STRATIFIED COASTAL OCEAN INTERACTIONS WITH HURRICANES

AND THE SEA BREEZE IN THE U.S. MID-ATLANTIC

by

GREGORY NICHOLAS SEROKA

A dissertation submitted to the

Graduate School-New Brunswick

Rutgers, The State University of New Jersey

In partial fulfillment of the requirements

For the degree of

Doctor of Philosophy

Graduate Program in Oceanography

Written under the direction of

Scott M. Glenn

And approved by

_____

_____

_____

_____

New Brunswick, New Jersey

October 2016

ABSTRACT OF THE DISSERTATION

STRATIFIED COASTAL OCEAN INTERACTIONS WITH HURRICANES

AND THE SEA BREEZE IN THE U.S. MID ATLANTIC

By GREGORY NICHOLAS SEROKA

Dissertation Director:

Scott M. Glenn

This dissertation uses the integration of modeling with observations and new analysis techniques to better understand and predict how the stratified coastal ocean interacts with important summer weather processes—tropical cyclones (TCs), which incur large coastal and inland damages, and the sea breeze circulation, which occurs nearly daily in the summer during high electricity demand periods. TC intensity prediction skill lags TC track prediction skill, and the shallow, coastal ocean remains a gap in TC research. The offshore component of the sea breeze is under-observed and poorly understood relative to its onshore component, and has important wind resource implications for the burgeoning U.S. offshore wind energy industry.

Using atmospheric modeling and coastal ocean observations with underwater gliders and buoys, it is shown in Hurricane Irene (2011) that stratified coastal ocean cooling—found to occur primarily ahead of the storm's eye center offshore the U.S. Mid-Atlantic—was the key missing contribution in modeling Irene's rapid decay just prior to NJ landfall. Irene's intensity was more sensitive to this cooling than any other model

parameter tested, and including this cooling in modeling mitigated the high bias in storm intensity predictions. Using ocean modeling, the spatiotemporal variability in the stratified coastal ocean cooling processes observed in Irene and Tropical Storm Barry (2007) was investigated. It was found that the dominant force balance across the entire Mid-Atlantic shelf ahead of storm eye passage for both storms was onshore wind stress balanced by offshore pressure gradient. This resulted in onshore surface currents opposing offshore bottom currents ahead-of-eye-center and enhancing surface to bottom current shear and surface cooling. Turbulent mixing cooled the surface layer while tides dominated the alternating warming/cooling advection signal. Finally, a new analysis technique, i.e. Lagrangian coherent structures, performed on atmospheric modeling was used to delineate the onshore surface convergent and offshore surface divergent sea breeze extents. It was found that atmospheric synoptic flow impacted the sea breeze onshore extent more than offshore extent, and that coastal upwelling did not impact sea breeze extent but rather caused an earlier onset and a shallower and more intense sea breeze both onshore and offshore.

Acknowledgements

This dissertation is the culmination of many years of work, and would not have been possible without the support of many, many people. Most importantly, I would like to thank my advisor Scott Glenn, who through many nights of staying late and ordering Chipotle/having leftover pizza, provided me with immeasurable guidance on the science of this thesis as well as all of his career advice.

I would also like to thank Rich Dunk, my external committee member, who through being a fellow meteorologist and through our countless phone conversations, always knew how to apply the scientific results to the real world and maximize the applied research aspects of the work to the offshore wind energy industry. I'm grateful for the valuable feedback from Josh Kohut, who, as thesis committee member, always had a unique and spot-on perspective when looking at my data plots, and who also knew how keep things light-hearted by cracking a joke at the right time. A thank you also goes to John Wilkin, who through both Graduate Program Director and thesis committee member, always kept the science on track, clear, and in context with past studies.

Thank you to Travis Miles, who joined Scott and me for many of those Chipotle/pizza nights of science arguing, bantering, and pioneering hurricane discovery, and, through the entirety of my Rutgers graduate career, was always there to bounce off ideas. Thanks to Oscar Schofield, who provided important feedback on the hurricane portions of my work. To Louis Bowers, how helped me to learn the ins and outs of WRF, and to Erick Fredj, who provided the invaluable expertise and code for the LCS simulations. I would like to thank past and present members of the Rutgers University Center for Ocean Observing Leadership, formerly the Coastal Ocean Observation Lab.

Without the help of many of you, I wouldn't have been able to press on in my thesis: Mike Crowley, Laura Palamara Nazzaro, Mike Smith, Hugh Roarty, John Kerfoot, Janice McDonnell, Carrie Ferraro, Patty Gillen, Steve Levenson, Yi Xu, and many others. Thank you to all the past and present fellow graduate students who have made my life better not only in work but also in my social life: Jack McSweeney, Alex Lopez, Aboozar Tabatabai, Mansha Pasricha, Filipa Carvalho, Nicole Waite, and many others. Thank you to all of my friends outside of the graduate program, who kept me sane throughout the ups and downs: Johnny Lin, Evan Buckland, Nick Pollock, Ryan Romanowski, Caroline Farkas, Megan Francis, and many others.

I would like to give a special thanks to my family: Mom, Dad, and Cheryl, for always being there for moral support when I needed it the most. And most importantly, thank you to my wife, Ilissa. I am forever grateful for all her guidance and thoughts on class projects, talks, papers, and overall science. Her creative ideas always made communicating my work that much more effective. I can't imagine life without her.

Table of Contents

List of Tables

List of Figures

Chapter 1

Introduction

Earth's northern mid-latitudes undergo large seasonal cycles, not only in the atmosphere but also in the ocean. Within the ocean, this seasonal cycle is especially pronounced over the western continental boundaries often characterized by broad continental shelves and proximity to coastal population centers [*Schofield et al.*, 2008]. The Mid-Atlantic Bight (MAB) of the eastern U.S. is located on one such broad continental shelf, with a large 20°C seasonal SST cycle. This seasonality in the surface ocean results in a well-mixed and cold coastal ocean in the winter and a highly-stratified warm surface and cold bottom coastal ocean in the summer [*Castelao et al.*, 2008], due to the presence of the summertime MAB Cold Pool at the bottom of the shelf water [*Houghton et al.*, 1982].

While the wintertime MAB circulation is characterized by a one-layer flow, during the summer the MAB acts as a two-layer system [*Lentz*, 2008 and references within]. Because the surface layer is isolated from the bottom during the summer two-layer regime, it is primarily wind-driven. Depending on the direction of the wind stress, upwelling or downwelling circulations can result. These circulations can have a large influence on the coastal sea surface temperature (SST) distribution and evolution, and resultant air-sea fluxes, impacting both hazardous (tropical cyclones, TCs) and persistent (sea breeze) summertime weather processes.

This dissertation investigates the interaction between the MAB stratified coastal ocean and both hurricanes and the sea breeze. Both topics are timely. TC track prediction has improved steadily over the past 20-25 years, but TC intensity prediction has lagged

[*Rogers et al.*, 2006; *Cangialosi and Franklin*, 2013]. This problem is even more important for landfalling storms, which must first cross the coastal ocean before making landfall. Daily sea breezes across the Mid-Atlantic occur during peak energy demand periods in the summer when household air conditioners are being used. Thus, it is critical to understand the interaction between the sea breeze and coastal upwelling circulation in the summer stratified two-layer system, especially for the burgeoning offshore wind energy industry. Further, understanding of the offshore component of the sea breeze lags that of the well-observed onshore component [*Steele et al.*, 2014]. This dissertation will describe one technique—Lagrangian coherent structures (LCSs)—that has yet to be used to clarify the offshore extent of the sea breeze.

In Chapter 2, the sensitivity of Hurricane Irene (2011) to the stratified coastal ocean cooling observed by [*Glenn et al.*, 2016] will be investigated in detail. The baroclinic coastal ocean cooling, the vast majority of which occurred ahead-of-eye-center, was not included in existing operational satellite SST products and coupled ocean-atmosphere hurricane models, and had the largest impact on the intensity of Irene over all other tested Weather Research and Forecasting (WRF) model parameters. While the size and structure of Irene was less sensitive to the cooling, including the cooling in atmospheric modeling mitigated the high storm intensity bias in predictions. It will be shown that this cooling—and not track, wind shear, or dry air intrusion—was the key missing contribution in modeling Irene's rapid decay prior to New Jersey (NJ) landfall. This chapter is published in Monthly Weather Review.

Chapter 3 builds off [*Glenn et al.*, 2016], which identified 11 hurricanes since 1985 that tracked northeastward over the MAB continental shelf during the highly

stratified summer months (June-August) and exhibited the ahead-of-eye-center cooling signal described in detail for Irene. While the ahead-of-eye-center cooling was observed at various MAB buoys during these storms, the details of the baroclinic coastal ocean processes that caused the cooling for each storm were not known. This chapter investigates the cross-shelf variability of the dominant forces and advective vs. mixing processes contributing to the cooling for Hurricane Irene (2011) and Tropical Storm Barry (2007). It will be shown that for Irene, the dominant force balance across the entire shelf before the eye passage was onshore wind stress balanced by offshore pressure gradient, resulting in vertical diffusion of cold bottom water across the thermocline and into the surface layer, and ahead-of-eye-center cooling. This force balance reversed after eye passage, with offshore wind stress balanced by onshore pressure gradient. For Barry, it will be shown that both the cross- and along-shelf momentum balances were important, but again dominated by onshore wind stress balanced by offshore pressure gradient ahead of eye passage, and offshore wind stress balanced by onshore pressure gradient after eye passage. Alternating warming/cooling due to tides dominated the advection terms in the temperature diagnostics, whereas vertical diffusion again was the main cause of the surface mixed layer cooling ahead-of-eye-center.

Chapter 4 describes the LCS technique used on WRF winds for delineating the onshore convergent and offshore divergent boundaries of the sea breeze. These boundaries will be used to test sensitivity of the sea breeze extent to synoptic flow and coastal upwelling. It will be shown that onshore sea breeze extent is very sensitive to synoptic flow, but the offshore extent is not, and that both the onshore and offshore extents are insensitive to coastal upwelling. However, coastal upwelling impacted sea

breeze intensity and onset time, with a shallower, sharper, and more intense onshore and offshore sea breeze, and earlier onset of the sea breeze, due to upwelling.

Chapter 2

Hurricane Irene (2011) Sensitivity to Stratified Coastal Ocean Cooling

2.1 Introduction

While tropical cyclone (TC) track prediction has steadily improved over the past two decades, TC intensity prediction has failed to progress in a similarly substantial way [*Cangialosi and Franklin*, 2013]. Many environmental factors control TC intensity, including the storm track itself, wind shear, intrusion of dry air, and upper-ocean thermal evolution [*Emanuel et al.*, 2004]. The last factor underlies all other processes because it directly impacts the fundamental transfer of energy from the ocean to the atmosphere within the TC heat engine [*Emanuel*, 1999; *Schade and Emanuel*, 1999].

Hurricane models often account for track and large-scale atmospheric processes that affect intensity—wind shear, dry air intrusion, and interaction with mid-latitude troughs [*Emanuel et al.*, 2004]. Some possible reasons include (i) greater attention to the atmosphere in modeling, and (ii) large-scale processes being resolved well, even with less advanced models. However, models do a comparatively less accurate job of representing oceanic processes that govern hurricane intensity because they are data limited [*Emanuel*, 1999, 2003; *Emanuel et al.*, 2004].

A specific upper-ocean thermal phenomenon that consistently emerges after a TC has passed is a cold pool of water left in the wake of its path, termed a "cold wake." This oceanic phenomenon has been observed behind TCs since at least the 1940s off the coast of Japan [*Suda*, 1943] and since at least the 1950s in the Atlantic, Caribbean, and Gulf of Mexico [*Fisher*, 1958]. Observational studies continued into the 1960s (e.g. Leipper 1967) with investigation of potential processes causing the cold wakes, such as upwelling

and turbulent entrainment of cold water into the warmer mixed layer. Studies in the late 1970s [*Chang and Anthes*, 1979; *Sutyrin and Agrenich*, 1979] began the use of idealized numerical simulations to investigate the effect of this oceanic cooling on TC intensity, but neglected TC movement. Then, numerical modeling studies in the 1980s [*Price*, 1981; *Sutyrin and Khain*, 1984] and 1990s [*Khain and Ginis*, 1991; *Bender et al.*, 1993; *Price et al.*, 1994] incorporated TC movement and three-dimensional coupled ocean-atmosphere models to further examine the negative SST feedback on storm intensity.

Prior to the 1980s and 1990s, observations of the upper ocean beneath a TC were uncommon due to the unpredictable and dangerous winds, waves, and currents in the storms [*D'Asaro*, 2003]. At that point, ocean observations in TCs, summarized by Price (1981), occurred primarily as a result of targeted studies using air-deployed profilers (e.g. Sanford et al. 1987; Shay et al. 1992), long-term observations that happened to be close to a TC's track (e.g. Forristall et al. 1977; Mayer and Mofjeld 1981; Dickey et al. 1998) or hydrographic surveys in a TC's wake (e.g. Brooks 1983). The severe conditions of TCs hampered progress in determining physical processes leading to the previously observed cold wake, as well as specific timing and location of the ocean cooling relative to the TC core. In the 2000s, studies began to provide observational and model evidence that significant portions of this surface ocean cooling can occur ahead of the hurricane eye center (e.g. D'Asaro 2003; Jacob and Shay 2003; Jaimes and Shay 2009), proposing that such cooling is especially important for hurricane intensity.

Even today, the bulk of research efforts have investigated deep ocean processes and their feedback onto TC intensity; indeed, a TC typically spends the vast majority of its lifetime over deep, open waters. However, rapid and significant changes in intensity

just before landfall and often in shallow water can have substantial implications on storm impacts, i.e., wind damage, storm surge, and inland flooding. For example, the statistical analysis by *Rappaport et al.* (2010) finds that category 3-5 hurricanes in the Gulf of Mexico weakened approaching landfall due to both vertical wind shear and hurricane-induced sea surface temperature reductions on the order of 1°C ahead of the storm center. Therefore, attention must be paid to coastal processes as well [*Marks et al.*, 1998], which inherently differ from deep water processes due to the influence of a shallow ocean bottom and coastal wall, and have been observed to produce SST cooling in TCs up to 11°C [*Glenn et al.*, 2016].

This chapter analyzes a recent landfalling storm, Hurricane Irene (2011), using a combination of unique datasets. Hurricane Irene is an ideal case study because in the days leading up to its landfall in New Jersey (NJ), its intensity was over-predicted by hurricane models (i.e. "guidance") and in resultant National Hurricane Center (NHC) forecasts [*Avila and Cangialosi*, 2012]. The NHC final report on the storm stated that there was a "consistent high bias [in the forecasts] during the U.S. watch/warning period." NHC attributes one factor in this weakening to an "incomplete eyewall replacement cycle" and a resulting broad and diffuse wind field that slowly decayed as the storm moved from the Bahamas to North Carolina (NC)—over a warm ocean and in relatively light wind shear. Irene made landfall in NC as a category 1 hurricane, two categories below expected strength.

One hypothesis as to why Irene unexpectedly weakened between the Bahamas and NC involves both aerosols and ocean cooling [*Lynn et al.*, 2015; *Khain et al.*, 2016]. Irene crossed a wide band of Sahara dust just north of the West Indies, initially causing

convection invigoration in the simulated eyewall and fostering the hurricane's development [*Lynn et al.*, 2015]. However, as Irene approached the U.S., continental aerosols intensified convection at the simulated storm's periphery. This intensification of convection at the TC periphery can lead to increases in TC central pressure and weakening of wind speed near the eyewall (Lynn et al. 2015 and references within).

This chapter's focus is on Irene's time after its NC landfall (Fig. 2.1) and after it had weakened in intensity due to continental aerosol interaction with convection at the hurricane's periphery and the slight SST cooling in the South Atlantic Bight (SAB). The SST cooling over the Mid Atlantic Bight (MAB) was at least 3-5 times greater than the SST cooling that occurred in the SAB (Figs. 2, 3).

While energetic ocean mesoscale features can distort the structure of the TC cold wake [*Walker et al.*, 2005; *Jaimes and Shay*, 2010; *Jaimes et al.*, 2011], during the direct forcing part of the storm, TC cooling in a deep ocean with no eddy features is frequently distributed symmetrically between the front and back half of the storm [*Price*, 1981]. This does not include the inertial response in the cold wake. As will be shown in this chapter, significant ahead-of-eye-center SST cooling (at least 6°C and up to 11°C, or 76-98% of total in-storm cooling) was observed over the MAB continental shelf during Hurricane Irene, indicating that coastal baroclinic processes enhanced the percentage of cooling that occurred ahead-of-eye-center [*Glenn et al.*, 2016].

This chapter will a) explore how Irene's predictions change using a semi-idealized treatment of the ahead-of-eye-center cooling, b) show that better treatment would have lowered the high bias in real-time predictions, and c) conclude that this ahead-of-eye-center cooling observed in Irene was the missing contribution—not wind

shear, track, or dry air intrusion—to the rapid decay of Irene's intensity just prior to NJ landfall.

2.2 Data and Methods

2.2.1 Gliders

Teledyne-Webb Research (TWR) Slocum gliders are autonomous underwater vehicles (AUVs) that have become useful platforms for monitoring the ocean's response to storms [*Glenn et al.*, 2008; *Ruiz et al.*, 2012; *Miles et al.*, 2013, 2015]. Gliders can profile the water column from the surface to depths of up to 1000 meters. They continuously sample every two seconds, providing a high temporal resolution time series from pre- to post-storm and complementing the spatial coverage that multiple concurrent Airborne eXpendable BathyThermograph (AXBT, Sessions et al. 1976; Sanabia et al. 2013) deployments can provide. Finally, gliders can be piloted, enabling more targeted profiling throughout the storm, in contrast to Argo [*Gould et al.*, 2004; *Roemmich et al.*, 2009] and ALAMO [*Sanabia and Jayne*, 2014; *Sanabia et al.*, 2016] floats, which passively move with ocean currents. Because of this, gliders can be directed to steer into a storm and station-keep, providing a fixed-point Eulerian observation time series. A more detailed description of general capabilities of these gliders can be found in Schofield et al. (2007). For storm-specific capabilities of the gliders, see Miles et al. (2013, 2015); Glenn et al. (2016).

Rutgers University Glider RU16 was used in this study. The glider was equipped with several science sensors, including a Seabird unpumped conductivity, temperature, and depth (CTD) sensor, which measured temperature, salinity, and water depth. The top

bin in the temperature profiles—0-1m depth—is used to provide a measure of near-surface temperature at the glider location (Fig. 2.1).

2.2.2 Buoys

2.2.2.1 Near-Surface Temperature

National Data Buoy Center (NDBC) buoys 41037 and 41036 in the SAB and buoys 44100, 44009, and 44065 in the MAB were used in this study (Fig. 2.1). Hourly water temperatures were used, which is measured at 0.6 m depth at all buoys except 0.46 m depth at 44100. These data provide near-surface water temperatures along and near the track of Hurricane Irene through the SAB and MAB.

2.2.2.2 Heat Fluxes

NDBC buoys 44009 and 44065 were used for latent and sensible heat flux calculations, which were estimated based on the "bulk formulae" [*Fairall et al.*, 1996]:

Sensible heat flux: $\quad H = -(\rho c_p)C_H U(\theta - \theta_{sfc})$ $\qquad$ (1)

Latent heat flux: $\quad E = -(\rho L_v)C_Q U(q - q_{sfc})$ $\qquad$ (2)

where ρ is density of air, c_p is specific heat capacity of air, C_H is sensible heat coefficient (see Eq. 5), U is 5m wind speed, θ is potential temperature of the air at 4m and θ_{sfc} is potential temperature at the water surface, L_v is enthalpy of vaporization, C_Q is latent heat coefficient (see Eq. 6), q is specific humidity of the air at 4m, and q_{sfc} is interfacial specific humidity at the water surface.

θ_{sfc} and q_{sfc} are both not directly computed from interfacial water temperature, but rather computed from buoy temperature measured at 0.6m depth. During high wind conditions, the difference between skin temperature and temperature at 0.6m depth is

likely small enough to have a negligible effect on the computed bulk fluxes [*Fairall et al.*, 1996].

2.2.3 Satellites

2.2.3.1 Sea Surface Temperature (SST)

The National Centers for Environmental Prediction (NCEP) Real-Time Global High-Resolution (RTG-HR) is a daily SST analysis used in this study. RTG-HR SST is operationally produced using in situ and AVHRR data on a 1/12° grid [*Reynolds and Chelton*, 2010]. The operational 13km Rapid Refresh (RAP) and the 12km North American Mesoscale model (NAM) and its inner nests, including the 4km NAM CONUS nest, use fixed RTG-HR SST. Therefore, RTG-HR is the most relevant SST product for comparison with the 2km SST composite described next.

Standard techniques to remove cloudy pixels in SST composites use a warmest pixel method because clouds are usually colder than the SST [*Cornillon et al.*, 1987]. This tends to reduce cloud contamination but results in a warm bias, which is unfavorable for capturing TC cooling. In this study, a three-day 'coldest dark pixel' composite method is used to map regions of cooling from Irene. This technique, described in Glenn et al. (2016), filters out bright cloudy pixels while retaining darker ocean pixels.

2.2.3.2 Water Vapor

Satellites are also used for a spatial estimate of the intrusion of dry air into Irene's circulation. Geostationary Operational Environmental Satellite (GOES) 13 Water Vapor Channel 3 brightness temperature imagery are used for these estimates.

2.2.4 Radiosondes

Radiosondes, typically borne aloft by a weather balloon released at the ground, directly measure temperature, humidity, and pressure, and derive wind speed and direction. To validate profiles of modeled wind shear and dry air intrusion, radiosonde observations of u and v winds are used from Albany, NY (KALB), Chatham, MA (KCHH), and Wallops Island, VA (KWAL), and RH is used from KALB and KWAL.

2.2.5 North American Regional Reanalysis (NARR)

The North American Regional Reanalysis (NARR) is a 32-km, 45 vertical layer atmospheric reanalysis produced by NCEP and provides a long-term (1979-present) set of consistent atmospheric data over North America [*Mesinger et al.*, 2006]. The data consist of reanalyses of the initial state of the atmosphere, which are produced by using a consistent data assimilation scheme to ingest a vast array of observational data into historical model hindcasts. NARR is used to evaluate modeled size and structure of Irene, modeled heat fluxes, and modeled wind shear, both horizontally and vertically.

2.2.6 Modeling and Experimental Design

2.2.6.1 Hurricane Weather Research and Forecasting (HWRF)

Output from two different versions of the Hurricane Weather Research and Forecast system [HWRF, Skamarock et al. (2008)] was used in this study: 1) the 2011 operational HWRF which was the Weather Research and Forecasting model (WRF) coupled to the feature-model-based Princeton Ocean Model [HWRF-POM, Blumberg and Mellor (1987)], and 2) the same HWRF atmospheric component but coupled to the Hybrid Coordinate Ocean Model [HWRF-HYCOM, Chassignet et al. (2007)].

For the operational 2011 hurricane season, POM for HWRF-POM was run at 1/6° resolution (~18km), with 23 terrain-following sigma coordinate vertical levels. The three-

dimensional POM output files contain data that are interpolated vertically onto the following vertical levels: 5, 15, 25, 35, 45, 55, 65, 77.5, 92.5, 110, 135, 175, 250, 375, 550, 775, 1100, 1550, 2100, 2800, 3700, 4850, and 5500m depth [*Tallapragada et al.*, 2011]. Near-surface temperatures are pulled from the top level of POM, which occurs at 5m.

The ocean model component of the 2011 HWRF-HYCOM system is the Real-Time Ocean Forecast System-HYCOM (RTOFS-HYCOM, Mehra and Rivin 2010), which varies smoothly in horizontal resolution from ~9km in the Gulf of Mexico to ~34km in the eastern North Atlantic [*Kim et al.*, 2014]. Initial conditions are estimated from RTOFS-Atlantic [*Mehra and Rivin*, 2010] 24-hour nowcasts [*Kim et al.*, 2014]. RTOFS-HYCOM uses the Goddard Institute for Space Studies (GISS) vertical mixing and diffusion scheme [*Canuto et al.*, 2001, 2002]. Near-surface temperatures are pulled from the top layer of HYCOM, which ranges from less than 1m in shallower regions (approximately 40m water column depth or less) to 3m in deeper regions (approximately 100m water column depth or greater).

2.2.6.2 Regional Ocean Modeling System (ROMS)

The Regional Ocean Modeling System (ROMS, http://www.roms.org, Haidvogel et al. 2008) is a free-surface, sigma coordinate, primitive equation ocean model that has been particularly used for coastal applications. Output is used from simulations run on the ESPreSSO (Experimental System for Predicting Shelf and Slope Optics) model [*Wilkin and Hunter*, 2013] grid, which covers the MAB from Cape Hatteras to Cape Cod, from the coast to past the shelf break, at 5km horizontal resolution and with 36 vertical levels.

2.2.6.3 WRF and Experimental Design

2.2.6.3.1 Control simulation

The Advanced Research dynamical core of WRF (WRF-ARW, http://www.wrf-model.org, [*Skamarock et al.*, 2008], Version 3.4 is a fully compressible, non-hydrostatic, terrain-following vertical coordinate, primitive equation atmospheric model. This WRF-ARW domain extends from South Florida to Nova Scotia, and from Michigan to Bermuda (Glenn et al. 2016).

In the experiments, the control simulation has a horizontal resolution of 6km with 35 vertical levels. The following physics options are used: longwave and shortwave radiation physics were both computed by the Rapid Radiative Transfer Model-Global (RRTMG) scheme; the Monin-Obukhov atmospheric layer model and the Noah Land Surface Model were used with the Yonsei University planetary boundary layer (PBL) scheme; and the WRF Double-Moment 6-class moisture microphysics scheme [*Lim and Hong*, 2010] was used for grid-scale precipitation processes. The control simulation did not include cumulus parameterization [*Kain*, 2004]; sensitivity to cumulus parameterization was tested in a subsequent simulation (see below and Table 2.1).

It was critical to ensure that the control simulation had a track very similar to the NHC best track, so as to not include any additional land effects on Irene's intensity as it tracked closely along the coast. Also, because TC translation speed has a large impact on SST response and subsequent negative feedback on TC intensity [*Mei et al.*, 2012], it was critical to closely simulate Irene's translation speed. Several different lateral boundary conditions and initialization times were experimented with before arriving at the best solution (after Zambon et al. 2014). The resulting initial and lateral boundary conditions

used are from the Global Forecast System (GFS) 0.5° operational cycle initialized at 06UTC 27 Aug 2011.

For the control simulation, RTG-HR SST from 00UTC 27 Aug 2011 is used for bottom boundary conditions over the ocean. This is six hours prior to model initialization, to mimic NAM and RAP operational conditions. All simulations are initialized at 06UTC 27 Aug 2011 when Irene was just south of NC (Fig. 2.1) and end at 18UTC 28 Aug 2011. By initializing so late, the focus is only on changes in Irene's intensity occurring in the MAB. Further, as will be shown below, model spin-up was a quick six hours, so the model is already in a state of statistical equilibrium [*Brown and Hakim*, 2013] under the applied dynamical forcing by the time Irene enters the MAB.

A two-part experiment, detailed below, is performed to investigate why model guidance did not fully capture the rapid decay of Irene just prior to NJ landfall. First, >140 simulations are conducted for sensitivities of Irene's intensity, size, and structure to various model parameters, physics schemes, and options, including horizontal and vertical resolution, microphysics [including a simulation with WRF spectral bin microphysics [*Khain et al.*, 2010] to test sensitivity to aerosols], PBL scheme, cumulus parameterization, longwave and shortwave radiation, land surface physics, air-sea flux parameterizations, coupling to a 1D ocean mixed layer (OML) model, coupling to a 3D ocean Price-Weller-Pinkel (PWP) model, and SST (Table 2.1). These simulations quantify and contextualize the sensitivities of Irene's modeled intensity, size, and structure to SST. Second, model assessment is performed, specifically evaluating the control run's treatment of track, wind shear, and dry air intrusion.

To conclude Data and Methods, details are provided on a few key sensitivities. These are: SST, air-sea flux parameterizations, 1D OML model, 3D PWP model, and latent heat flux <0 over water.

2.2.6.3.2 Sensitivity to SST

To quantify the maximum impact of the ahead-of-eye-center SST cooling on storm intensity, the control run using a static warm pre-storm SST (RTG-HR SST) is compared to a simulation using static observed cold post-storm SSTs. For this cold SST, the 29-31 Aug 2011 three-day coldest dark-pixel SST composite (described above) is used (Fig. 2.3E). According to underwater glider and NDBC buoy observations along Irene's entire MAB track (Fig. 2.1), almost all of the SST cooling in the MAB occurred ahead of Irene's eye center (Fig. 2.2C-F). The SAB also experienced ahead-of-eye-center SST cooling, but values are on the order of 1°C or less (Fig. 2.2A-B). Also, the model simulations include only six hours of storm presence over the SAB. Therefore, the SST simulations described above quantify the sensitivity of Irene to ahead-of-eye-center cooling that occurred only in the MAB.

2.2.6.3.3 Sensitivity to air-sea flux parameterizations

The bulk formulae for sensible and latent heat fluxes are listed above in the buoy heat flux description. The following is the equation for momentum flux:

Momentum flux: $\tau = -\rho C_D U^2$ (3)

where ρ is density of air, C_D is drag coefficient, and U is 10 m wind speed.

Three options exist in WRF-ARW Version 3.0 and later for air-sea flux parameterizations (WRF namelist option *isftcflx*=0, 1, and 2). These parameterization

options change the momentum (z_0), sensible heat (z_T), and latent heat (z_Q) roughness

lengths in the following equations for drag, sensible heat, and latent heat coefficients:

Drag coefficient: $\qquad\qquad C_D = \kappa^2/[\ln(z_{ref}/z_0)]^2 \qquad$ (4)

Sensible heat coefficient: $\qquad C_H = (C_D^{\frac{1}{2}})[\kappa/\ln(z_{ref}/z_T)] \qquad$ (5)

Latent heat coefficient: $\qquad C_Q = (C_D^{\frac{1}{2}})[\kappa/\ln(z_{ref}/z_Q)] \qquad$ (6)

where κ is the von Kármán constant and z_{ref} is a reference height (usually 10m).

The reader is encouraged to refer to Green and Zhang (2013) for a detailed look at

the impact of *isftcflx*=0, 1 and 2 on roughness lengths, exchange coefficients, and

exchange coefficient ratios C_H/C_D, C_Q/C_D, and C_K/C_D, where $C_K=C_H+C_Q$. Some key

points from their paper are that, at wind speeds of 33 m s^{-1} or greater, *isftcflx=1* has the

largest C_K/C_D ratio and shares with *isftcflx=2* the lowest C_D. As a result, they found that

for Hurricane Katrina (2005), using *isftcflx*=1 produced the most intense storm in terms

of minimum SLP and max winds.

Therefore, our SST sensitivity effectively changes the variables θ_{sfc} and q_{sfc} in

equations 1-3 above, while our air-sea flux parameterization sensitivities change the

equations for the momentum, sensible heat, and latent heat coefficients (equations 4-6)

going into the respective flux equations (1-3). Because *isftcflx*=1 and *isftcflx*=2 both

include a term for dissipative heating and *isftcflx*=0 does not in WRFv3.4 [*Green and*

Zhang, 2013], the air-sea flux parameterization sensitivity between *isftcflx*=0 and 1, and

between *isftcflx*=0 and 2 also test the effect of turning on and off dissipative heating in

the model. Although the dissipative heating term was removed as of WRFv3.7.1 due to

controversy within the wind-wave modeling community, dissipative heating is still

considered an important issue in high wind regimes, and it has been shown to be capable

of increasing TC intensity by 10-20% as measured by maximum sustained surface wind speeds [*Liu et al.*, 2011].

For the air-sea flux parameterization sensitivities, simulations are conducted with *isftcflx*=0, 1, and 2 using both the warm (control) and cold SST boundary conditions.

2.2.6.3.4 Sensitivities coupling WRF to 1D and 3D ocean models

Pollard et al.'s (1972; described in WRF context by Davis et al. 2008) 1D ocean mixed layer model was used to test the sensitivity of Irene to 1D ocean processes. Two different initializations of the 1D ocean model were initially performed: 1) *coastal stratification*: initializing the mixed layer depth (MLD) everywhere to 10m and the slope of the thermocline everywhere to 1.6°C/m according to glider RU16's observations [*Glenn et al.*, 2016], and 2) *HYCOM stratification:* initializing the MLD and top 200m mean ocean temperature spatially using HYCOM. However, there were major issues using both of these options to accurately determine sensitivity to 1D ocean processes. The issue with the first option is its requirement that the initialization is non-variant in space; the Gulf Stream, which is included in the model domain, is very warm and well mixed down to 100-200m [*Fuglister and Worthington*, 1951]. Initializing the Gulf Stream MLD to 10m would result in cold water only 10m deep being quickly mixed to the surface. The issue with the second option of using HYCOM is that due to its poor initialization, the HYCOM simulation used here did not resolve the abundant bottom cold water over the MAB Continental Shelf that was observed by glider RU16 prior to Irene [*Glenn et al.*, 2016] and that is typical of the summer MAB Cold Pool [*Houghton et al.*, 1982].

The 3D ocean PWP model [*Price et al.*, 1986, 1994] was used to test the sensitivity of Irene to 3D open ocean, deepwater processes, including Ekman

pumping/upwelling and mixing across the base of the mixed layer caused by shear

instability. While the 3D PWP model contains 3D dynamics and is fully coupled to WRF,

it does not have bathymetry or a coastline [*Lee and Chen*, 2014]; water depth is uniform

across the model grid. Therefore, any 3D PWP model run will not simulate the coastal

baroclinic processes that were observed in Irene over the MAB continental shelf due to

the presence of the coastline [*Glenn et al.*, 2016]. In addition, like in the 1D ocean model,

initialization must be non-variant in x-y space.

To ameliorate the issue with mixing the Gulf Stream and still conduct sensitivities

on non-static 1D and 3D ocean processes, an initialization time 12 hours later—18UTC

on 27 Aug instead of 06UTC on 27 Aug—was used for the WRF-1D OML and WRF-3D

PWP simulations, because Irene by then was already north of the Gulf Stream and thus

would not interact with it, and still south of the MAB (see Fig. 2.1). Four sensitivities

with this initialization time were tested with various configurations of the 1D OML and

3D PWP models. First, the 1D OML model was initialized using the pre-storm coldest

dark-pixel composite for SST and with a MLD of 200m, to simulate isothermal warm

ocean conditions and the effect of air-sea heat fluxes. Second, the 1D OML model was

initialized everywhere using RU16 observed stratification, as described above; this

simulated the effect of 1D deepwater mixing processes (the 1D OML model does not

have an ocean bottom). Third, the 3D PWP model was initialized everywhere using the

same RU16 observed stratification that was used for the 1D OML model simulation but

with 400m full water column depth, to simulate the effect of 3D deepwater processes.

Fourth, the 3D PWP model was initialized everywhere using HWRF-HYCOM

stratification at the RU16 glider location at 00UTC 26 Aug and again with 400m full

water column depth, to test the sensitivity to a poor ocean initialization. These simulations are summarized in Table 2.1.

2.2.6.3.5 Sensitivity to latent heat flux <0 over water

In the WRF surface layer scheme code, a switch exists that disallows any latent heat flux <0 W m^{-2}. (There is also a switch that disallows any sensible heat flux <-250 W m^{-2}). WRF convention for negative heat flux is downward, or from atmosphere to land or water surface. This sensitivity involves removing the switch disallowing negative latent heat flux. This switch removal only results in changes in latent heat flux over water, because the subsequent WRF land surface scheme modifies fluxes and already allows for latent heat flux to be negative over land.

2.3 Results

2.3.1 Sensitivity Tests

2.3.1.1 Motivation

Hurricane Irene developed into a tropical storm just east of the Lesser Antilles on August 20, 2011, strengthening into a Category 1 hurricane just after landfall in Puerto Rico two days later. Irene continued to move northwest over the Bahamas, intensifying into a Category 3 hurricane on August 23. Soon after, a partial eyewall replacement cycle occurred and Irene was never able to fully recover, eventually weakening into a Category 1 hurricane on August 27 as it neared NC. Irene remained at hurricane strength over the MAB until it made landfall in NJ as a tropical storm at 09:35UTC Aug 28. As stated above, the NHC final report on Irene [*Avila and Cangialosi*, 2012] conveyed a "consistent high bias [in the forecasts] during the U.S. watch/warning period", which

consisted of the time period when Irene was traversing the SAB and MAB [*Avila and Cangialosi*, 2012].

The coastal track of Irene (Fig. 2.1) over the relatively highly-instrumented Mid-Atlantic allowed for a comprehensive look into the details and timing of coastal ocean cooling. All in-water instruments employed here provide fixed point data within 70 km from Irene's eye, including station-keeping RU16, providing an Eulerian look at the ahead-of-eye-center cooling occurring near the storm's inner core. RU16 profiled the entire column of water over the MAB continental shelf, providing a view of the full evolution of the upper ocean response. The rapid two-layer shear-induced coastal mixing process that led to ahead-of-eye-center cooling is described in detail in Glenn et al. (2016).

The buoys in the SAB (41037 and 41036) documented ~1°C SST cooling in the storm's front half, with total SST cooling less than 2°C (Fig. 2.2). Eye passage at each buoy is indicated by a vertical dashed line and represents the minimum sea level pressure (SLP) observed. For RU16, minimum SLP taken from the nearby WeatherFlow Tuckerton coastal meteorological station was used to calculate eye passage time, and for 44100, linearly interpolated NHC best track data was used for eye passage time. In contrast to the SAB, the MAB buoys (44100, 44009, and 44065) as well as RU16 observed 4-6°C SST cooling ahead-of-eye-center, with only slight cooling after eye passage of less than 2°C (Fig. 2.2). Therefore, the buoys and glider provide detailed evidence that significant ahead-of-eye-center cooling—76-98% of the total observed in-storm cooling [*Glenn et al.*, 2016]—occurred in the MAB.

While the buoys provided information on the timing of SST cooling, the high-resolution coldest dark pixel SST composite showed the spatial variability of the cooling, revealing that the cooling was not captured by basic satellite products and some models used to forecast hurricane intensity. The improved three-day coldest dark pixel SST composite showed pre-storm (24-26 Aug 2011, Fig. 2.3A) and post-storm (29-31 Aug 2011, Fig. 2.3E) SST conditions along the U.S. East Coast. SST cooling to the right of storm track in the SAB approached 2°C, and in the MAB approached 11°C at the mouth of the Hudson Canyon (Fig. 2.3I). Under the TC inner core, within 25km of Irene's track, SST cooling in the SAB ranged from 0.5 to 1.5°C, while in the MAB cooling ranged from ~2 to ~4°C (Fig. 2.3M). It is important to note that the SST composite from three days after storm passage was used for post-storm conditions. There were, indeed, large cloud-free areas over the MAB one day after storm passage, but it took an additional two days to fill in the remaining areas over the MAB and attain a cloud-free composite for input into WRF. In the persistently clear areas during this three-day stretch, no additional SST cooling occurred during the post-storm inertial mixing period after the direct storm forcing.

RTG-HR SST pre- (26 Aug, Fig. 2.3B), post-storm (31 Aug, Fig. 2.3F), and difference (31 Aug minus 26 Aug, Fig. 2.3J) plots show spatially similar cooling patterns to the coldest dark pixel SST composite, but cooling magnitudes are lower, especially to the right of storm track in both the SAB and MAB (Fig. 2.3J). Similarly, there was no significant additional MAB cooling in RTG-HR SST from one day after (not shown) to three days after (Fig. 2.3F) storm passage.

HWRF-POM (Fig. 2.3C, G, K, O) and HWRF-HYCOM (Fig. 2.3D, H, L, P)

model results are also shown as examples of coupled ocean-atmosphere hurricane

models. Pre-storm (00UTC Aug 26) and post-storm (00UTC Aug 31) times for both

model results are coincident with the coldest dark pixel SST composite and RTG-HR

SST composite times, and both model simulations shown are initialized at 00UTC 26

Aug. Therefore, the post-storm SST conditions are 5-day forecasts in both models. Again,

there are no significant differences in MAB SST cooling between immediately after and

three days after Irene's passage in both HWRF-POM and HWRF-HYCOM. Like RTG-

HR post-storm SST (Fig. 2.3F), HWRF-POM (Fig. 2.3G) and HWRF-HYCOM (Fig.

2.3H) post-storm SSTs in the MAB are several degrees too warm—coldest SSTs are 20-

23°C, where they should be 17-20°C. Therefore, these coupled atmosphere-ocean models

designed to predict TCs did not fully capture the magnitude of SST cooling in the MAB

that resulted from Hurricane Irene.

2.3.1.2 Sensitivity Results

Over 140 WRF simulations were conducted to test the sensitivity of modeled

Irene intensity to the observed ahead-of-eye-center cooling and to other model

parameters. Only those simulations with tracks within 50km of NHC best track were

retained, leaving 30 simulations (Table 2.1).

To quantify cumulative model sensitivities, the sum of the absolute value of the

hourly difference between the control run minimum SLP (and maximum sustained 10m

winds) and experimental run minimum SLP (and max 10m winds) was taken, but only

from 23UTC 27 Aug to the end of the simulation. This confines the sensitivity to the time

period of Irene's presence over the MAB and thereafter. The equation is as follows:

$$\sum_{i=23UTC\ 27Aug}^{i=18UTC\ 28Aug} |\min SLP[control(@hour\ i)] - \min SLP[exp.(@hour\ i)]| \qquad (7)$$

Figure 2.4 shows the model sensitivities as measured by minimum SLP (left) and maximum 10m wind speeds (right). Over the 19 hours calculated, the three largest sensitivities when considering both intensity metrics were due to SST with the three WRF air-sea flux parameterization options (*isftcflx*=0, 1, 2). On average, for SST over the three options, pressure sensitivity was 66.6 hPa over the 19 hours (3.5 hPa hr^{-1}) and wind sensitivity was 52.0 m s^{-1} over the 19 hours (2.7 m s^{-1} hr^{-1}). Sensitivity to 3D open ocean, deepwater processes through the use of the 3D PWP model was comparatively large (Fig. 2.4). However, caution must be taken with this simulation because the 3D PWP model does not have a coastline and bathymetry, and ended up producing more in storm SST cooling than was observed by glider RU16 (not shown).

The Advanced Hurricane WRF sensitivities for the 12-hour later initialization (1D warm isothermal, 1D stratified, and 3D PWP) are presented in time series in Figs. 2.5A and 2.6A. The black line indicates NHC best track estimates of intensity, while the red solid line indicates the fixed pre-storm warm SST control run. Note that min SLP at initialization is about 973 mb whereas NHC best track indicates 950 hPa at that time; this difference is due to issues with WRF's vortex initialization [*Zambon et al.*, 2014a], and it only takes six hours for the model to adjust and drop 13 hPa to 959 hPa. The dotted red line indicates a sensitivity with digital filter initialization (DFI) turned on, which removes ambient noise at initialization. DFI resulted in initial min SLP (max winds) to be ~960 hPa (33 m s^{-1})—a reduction of 12 hPa (2 m s^{-1})—with downstream sensitivity negligible, demonstrating that the seemingly significant initialization issue likely has little significant effect on downstream intensity. The remaining sensitivities in Figs. 2.5A and 2.6A are

the 1D ocean with isothermal warm initial conditions (effect of air-sea fluxes) in cyan,

the 1D ocean with stratified initial conditions (effect of 1D mixing processes) in light

blue, and the 3D PWP deep ocean with stratified initial conditions (effect of 3D

deepwater processes) in dark blue. The air-sea fluxes have a negligible effect on

intensity, while the 1D ocean mixing and 3D deepwater processes have a gradually larger

negative effect on intensity.

The air-sea flux parameterization sensitivities with the standard initialization time

are shown in Fig. 2.5B and 2.6B. Again, the black line indicates NHC best track

estimates of intensity, and the simulations have issues with vortex initialization. The DFI

sensitivity for this set of runs (dotted red) again effectively resolves this issue. The red

lines indicate the three WRF air-sea flux parameterization options using the warm pre-

storm SST with the area between the *isftcflx*=0 and 1 options shaded in red, and the blue

lines and blue shading indicate the same but for the cold post-storm SST. Consistent with

the results found by Green and Zhang (2013), *isftcflx*=1 produced the most intense storm

using both minimum SLP and max winds intensity metrics, for both the warm pre-storm

SST and cold post-storm SST; again, *isftcflx*=1 has the largest C_K/C_D ratio and shares

with *isftcflx=2* the lowest C_D.

Figures 2.5C and 2.6C show the time evolution of three sensitivities: 1) SST,

warm vs. cold (black), 2) air-sea flux parameterization with warm SST, *isftcflx*=0 vs. 1

(red), and 3) air-sea flux parameterization with cold SST, *isftcflx*=0 vs. 1 (blue). For both

intensity metrics, sensitivity to SST gradually increases from about equal to flux

parameterization sensitivity upon entrance to the MAB (first gray vertical dashed line) to

almost triple it (~5 hPa vs. ~2 hPa, 6 m s^{-1} vs. ~0-2 m s^{-1}) upon exit out of the MAB

(second gray vertical dashed line). Finally, Figs. 2.5D-E and 2.6D-E show box and whisker plots of simulation error as compared to NHC best track, only during MAB presence (23UTC 27 Aug to 13UTC 28 Aug), with uncertainty in NHC best track data [*Torn and Snyder*, 2012; *Landsea and Franklin*, 2013] shown with gray shading. Correlation coefficient (R^2) values are shown at the bottom in gray, and ΔP and $\Delta WSPD$ are shown in black, with NHC ΔP and $\Delta WSPD$ values shown in the top right of panel E. These delta values, a measure of weakening rate, are calculated by taking the difference in pressure and wind speed between exit out of, and entrance into, the MAB.

Although the errors in min SLP for the simulations in Fig. 2.5D are low and the R^2 values are high, the errors in max winds are higher and the R^2 values are much lower in Fig. 2.6D. The four warm SST simulations (Figs. 2.5E and 2.6E) have a min SLP too low and max wind speed too high, while the three cold SST simulations have a min SLP closer to NHC best track and a max wind speed slightly lower than NHC best track. Because of the high uncertainty (4-5 m/s for non-major hurricanes) associated with NHC best track wind estimates [*Torn and Snyder*, 2012; *Landsea and Franklin*, 2013], errors from the pressure metric are used. Minimum SLP is also a more certain measure of intensity because it is always at the TC eye center. The highest R^2 values and the ΔP values closest to NHC best track ΔP were found with the three cold SST simulations. This indicates that a more accurate representation of the ahead-of-eye-center cooling via fixed cold post-storm SSTs lowers the high bias in our model's prediction of intensity. Further, the low ΔP/weakening rate attained using the 3D deepwater PWP simulation (ΔP: 6.8 hPa; rate: 0.5 hPa hr^{-1})—which again did not have a coastline or appropriately shallow ocean bottom—suggests that coastal baroclinic processes were responsible for

the cooling that contributed to Irene's observed larger ΔP/weakening rate (ΔP: 14 hPa; rate: 1 hPa hr^{-1}). These coastal baroclinic processes, which are investigated in detail in Glenn et al. (2016), can be summarized as follows:

(a) front half of Irene's winds were onshore towards the Mid Atlantic coastline

(b) ocean currents in the surface layer above the sharp, shallow thermocline were aligned with the winds and also directed onshore over the MAB Continental Shelf

(c) water piled up along the Mid Atlantic coast, setting up a pressure gradient force directed offshore

(d) responding to the coastal piling of water, currents in the bottom layer below the sharp, shallow thermocline were directed offshore

(e) opposing onshore surface layer and offshore bottom layer currents led to large shear across the thermocline and turbulent entrainment of abundant bottom cold water to the surface; this enhancement of shear and SST cooling occurred in the front half of Irene as long as the winds were directed onshore (hence the term "ahead-of-eye-center cooling").

Therefore, without the coastline in simulations, 1) the coastal piling of water, 2) the offshore bottom counterflow, 3) the enhanced shear at the thermocline, and 4) the rapid surface cooling would not be simulated.

Finally, the deep ocean simulations using the 1D ocean and the 3D ocean PWP model initialized with stratified conditions produced 32% and 56% of the in-storm cooling ahead-of-eye-center at the RU16 glider location, respectively (not shown). Meanwhile, 76% of the observed in-storm cooling at the RU16 glider location—and

82%, 90%, and 98% at 44009, 44065, and 44100, respectively—occurred ahead-of-eye-center (Fig. 2.2), further indicating that the non-simulated coastal baroclinic processes enhanced the percentage of ahead-of-eye-center cooling in Irene.

How sensitive are Irene's size and structure to SST? To spatially evaluate WRF results, NARR SLP and winds are used (Fig. 2.7). Spatial plots of SLP are shown from NARR (Fig. 2.7A), WRF warm SST (Fig. 2.7B), and WRF cold SST (Fig. 2.7C) runs, at just before NJ landfall. Only slight differences exist between WRF simulations, mainly in Irene's central pressure (warm SST: 955.4 hPa, cold SST: 959.1 hPa); overall size and structure of the storm is very similar between runs. The WRF simulations also compare well in size and shape to NARR SLP, but do not in central pressure (NARR: 975.9 hPa). This is likely due to lower NARR resolution, as the NHC best track estimate of central pressure at landfall, only 35 min after, is 959 hPa. NARR, at 32-km resolution, is far too coarse to resolve inner-eyewall processes [*Gentry and Lackmann*, 2009; *Hill and Lackmann*, 2009].

Similar results are shown in spatial plots of 10m winds (Fig. 2.8). General size and structure, especially over land, agree well among NARR, warm SST, and cold SST runs, but major differences exist over the MAB waters. NARR shows a maximum wind speed of 22.7 m s^{-1}, whereas the WRF warm SST (33.0 m s^{-1}) and cold SST (31.0 m s^{-1}) simulations are much closer to NHC best track's estimate of 30.9 m s^{-1}. Besides a general overall reduction in wind speed in the cold SST simulation, little difference is noted in size of Irene between warm and cold SST. This is verified by a radius of maximum wind (RMW) comparison between the warm and cold SST simulations and b-deck data from the Automated Tropical Cyclone Forecast (ATCF, Sampson and Schrader 2000) system

database (Table 2.2). The data files within ATCF are within three decks known as a-, b-, and f-decks. The b-deck data for Irene, available every six hours, shows good agreement with both warm and cold SST simulations, with 13 km or less difference in RMW between warm and cold SST for the first 24 hours of simulation, and 21 km or less difference in RMW between model and "observed" b-deck radii for the first 18 hours of simulation. At 12UTC 28 Aug, the cold SST simulation shows a much larger RMW, likely due to the strongest winds occurring in an outer band thunderstorm and indicating more rapid enlargement of storm size.

Vertical east-west (Fig. 2.9A-C) and north-south (Fig. 2.9D-F) cross sections of wind speeds through the eye of Irene at 09UTC 28 Aug, just before landfall, tell the same story—that NARR has issues reproducing the higher wind speeds not only at 10m but through the entire atmosphere, and that there are only slight differences in wind speed structure between the warm and cold SST simulations. Both simulations show an asymmetric storm west to east with the core of the strongest winds over water, on the right side of the eye, extending all the way up to the tropopause at about 200 hPa (Fig. 2.9B and C), with the warm SST run showing much higher wind speeds from ~950 hPa to 700 hPa. On the left side of the eye, the strongest winds extend only up to 700-800 hPa and the core is much narrower from west to east. The north-south cross sections show a more symmetric storm, as well as the outer edges of the Jet Stream at about 200 hPa and 45°N.

Because air-sea heat fluxes drive convection, TC circulation, and thus resulting TC intensity, a closer look at the sensible and latent heat fluxes, specifically to determine just how sensitive they are to a change in SST, is warranted. The fluxes are plotted

spatially at 00UTC 28 Aug in Fig. 2.10, and temporally at two MAB buoys in Fig. 2.11.

The largest modeled latent and sensible heat fluxes correlate well spatially with the

strongest winds in NARR, warm SST, and cold SST runs (Fig. 2.10). However, there are

large differences in both latent and sensible heat fluxes between the warm and cold SST

runs, most notably over the MAB where a reverse in the sign of both latent and sensible

heat flux occurs. In some locations over the MAB, the warm SST run shows a few

hundred W m^{-2} in latent heat flux directed from the ocean to the atmosphere (Fig. 2.10E),

whereas the cold SST run shows several hundred W m^{-2} in the opposite direction (Fig.

2.10F). NARR also shows slightly negative latent heat flux over the MAB (NARR fluxes

are 3-hr averages). Similar patterns are evident in sensible heat flux, but at a much

smaller magnitude. It is again important to note that a negative latent heat flux over

water—directed from the atmosphere to the ocean—is disallowed in WRF (similarly,

sensible heat fluxes <-250 W m^{-2} are also disallowed over water). What is shown for the

cold SST (warm SST) run in Fig. 2.10 is the cold SST (warm SST) simulation from

sensitivity number 19 (18) (Table 2.1), with latent heat flux <0 allowed over water. When

negative latent heat flux is not allowed, all negative latent heat fluxes (e.g. the blue areas

in Fig. 2.10F) become zero (not shown).

 The negative latent heat fluxes were also "observed" at both buoys at which they

were calculated—44009 and 44065. At both buoys, for almost the entire times shown, air

temperature was greater than SST—in some cases over 4.5°C warmer—and air specific

humidity was greater than specific humidity at water surface (Fig. 2.11A, B). The largest

temperature and specific humidity differences occurred either during or right at the end of

the SST cooling at each buoy, and coincided with the largest calculated "observed"

negative sensible heat fluxes (-50 W m^{-2} to -100 W m^{-2}) and negative latent heat fluxes (-200 W m^{-2} to -250 W m^{-2}) at both buoys (Fig. 2.11C, D). These negative values are in stark contrast to the positive enthalpy fluxes (latent + sensible heat fluxes) of O(1000) W m^{-2} found under normal and rapid TC intensification scenarios [*Lin et al.*, 2009; *Jaimes and Shay*, 2015]. At this time, NARR latent heat fluxes approached -120 W m^{-2} at 44009 and -40 W m^{-2} at 44065. The cold SST simulation shows latent heat fluxes zeroed out this whole time period (Fig. 2.11C, D), and approached -180 W m^{-2} at 44009 and -130 W m^{-2} at 44065 when negative latent heat fluxes are allowed (Fig. 2.11E, F). Meanwhile, the warm SST simulation shows latent heat fluxes with opposite sign, approaching 470 W m^{-2} toward the end of the simulation at 44009 and 530 W m^{-2} at 44065. Further, heat flux sensitivity to air-sea flux parameterizations was low, especially when compared to its sensitivity to warm vs. cold SST. This evaluation of air-sea heat fluxes confirms that the cold SST simulation not only begins to resolve the negative latent heat fluxes that have been indicated by observations, but also approaches negative values that significantly affect storm intensity.

2.3.1.3 Validation of Track, Wind Shear, and Dry Air Intrusion

To test our hypothesis that upper ocean thermal structure and evolution in the MAB was the missing contribution to Irene's decay just before NJ landfall, the control run's treatment of track, wind shear, and dry air intrusion was evaluated.

Track was handled very well by the simulations, remaining within 30 km for the entire time series for the control run and until landfall for the cold SST sensitivity (Fig. 2.1, Table 2.3). As Irene tracked so close to shore, this was critical for teasing out any potential impact from land interactions. In addition, control run translation speed over the

MAB (~10 m s^{-1}) and cold SST sensitivity translation speed over the MAB (~10 m s^{-1}) were consistent with NHC best track translation speed for Irene over the MAB (~10 m s^{-1}). For context, typical TC translation speed at 36-40°N (approximate MAB latitude range) is 8-10 m s^{-1} [*Mei et al.*, 2012].

Wind shear values within and ahead of Irene during its MAB presence were similarly handled well by the simulations. At the time of entrance into the MAB, 200-850 hPa wind shear values in NARR, WRF warm SST, and WRF cold SST runs approached 60 m s^{-1} in the near vicinity ahead of Irene's eye (Fig. 2.12A, C, E). Radiosonde launches from KALB, KCHH, and KWAL at the same time showed 200-850 hPa wind shear values of about 38 m s^{-1}, 34 m s^{-1}, and 15 m s^{-1}, respectively, which matched well with NARR (44 m s^{-1}, 29 m s^{-1}, 22 m s^{-1}) and both WRF simulations (41 m s^{-1}, 33 m s^{-1}, 17 m s^{-1} for warm SST; 39 m s^{-1}, 32 m s^{-1}, 19 m s^{-1} for cold SST); furthermore, simulated u and v wind profiles across the entire atmospheric column correlated well with observed profiles (Fig. 2.12G, I, K). Twelve hours later, wind shear values ahead of Irene in NARR and both WRF simulations again approached 60 m s^{-1}, and observed wind shear at all three radiosonde sites correlated well with NARR and WRF (Fig. 2.12H, J, L). Finally, time series of 200-850 hPa and 500-850 hPa wind shear values for NARR and WRF simulations were calculated by averaging wind shear values within an annulus 200 to 800 km from Irene's center [*Rhome et al.*, 2006; *Zambon et al.*, 2014b]. 200-850 hPa wind shear values increase from approximately 20 m s^{-1} at 12UTC 27 Aug to 25-30 m s-1 by the end of the simulation. These wind shear values were likely extremely detrimental to Irene's intensity. Our WRF simulations accurately reproduced these very high values and thus our model captured this important contribution to Irene's decay.

Finally, a snapshot of RH at 200 hPa and 700 hPa from WRF at 12UTC 28 Aug

shows an intrusion of dryer air into the southeast quadrant of Irene, agreeing well with a

GOES water vapor image 12 minutes later (Fig. 2.13A-E). This GOES image indicates

dry upper levels (~200 hPa) and moist lower levels (~700 hPa) in the southern half of the

storm. In the northern half of the storm there are moist upper and lower levels. Our WRF

simulations match well in both halves. WRF simulations are also consistent with

observations from a KALB radiosonde (Fig. 2.13F, dashed lines), which was in the

storm's northern half at this time and showed moist lower levels and relatively moist

upper levels. Comparisons with a KWAL radiosonde (Fig. 2.13F, solid lines), which was

in the storm's southern half at this time, showed WRF actually drying out the atmosphere

more than observed between approximately 700 and 300 hPa. Overdrying the mid-levels

would result in additional decreases in storm intensity, so it is clear that dry air intrusion

was also not a neglected contribution to Irene's decay.

2.4 Discussion

In summary, significant ahead-of-eye-center SST cooling (at least 6°C and up to

11°C, or 76-98% of in-storm cooling) was observed over the MAB continental shelf

during Hurricane Irene. Standard coupled ocean-atmosphere hurricane models did not

resolve this cooling in their predictions, and operational satellite SST products did not

capture the result of the cooling. In this chapter, the sensitivity of Irene's intensity, size,

and structure to the ahead-of-eye-center SST cooling was quantified. The intensity

sensitivity to the ahead-of-eye-center cooling turned out to be the largest among tested

model parameters, surpassing sensitivity to the parameterization of air-sea fluxes

themselves. Storm size and structure sensitivity to the ahead-of-eye cooling was comparatively low.

Furthermore, accounting for the ahead-of-eye-center SST cooling in our modeling through the use of a fixed cold post-storm SST that captured the cooling mitigated the high bias in model predictions. Validation of modeled heat fluxes indicated that the cold SST simulation accurately reversed the sign of latent heat flux over the MAB as observed by two NDBC buoys. This would confirm the use of post-storm SST fixed through simulation so that Irene would propagate over the colder "pre-mixed" waters, even though some slight cooling did indeed occur after eye passage. Finally, the simulations handled track, wind shear, and dry air intrusion well, indicating that upper ocean thermal evolution was the key missing contribution to Irene's decay just prior to NJ landfall.

Simplistic 1D ocean models are incapable of resolving the 3D coastal baroclinic processes responsible for the ahead-of-eye-center cooling observed in Irene, consistent with Zambon et al. (2014) in their study of Hurricane Ivan (2004). Rather, a 3D high resolution coastal ocean model, such as ROMS, nested within a synoptic or global-scale ocean model like HYCOM and initialized with realistic coastal ocean stratification, could begin to spatially and temporally resolve this evidently important coastal baroclinic process (as described above in the Results section), adding significant value to TC prediction in the coastal ocean—the last hours before landfall where impacts (storm surge, wind damage, and inland flooding) are greatest and are most closely linked with changes in storm intensity.

A ROMS simulation at 5km horizontal resolution over the MAB not specifically designed for TCs can begin to resolve this ahead-of-eye-center cooling spatially (Fig.

2.14). This moderately accurate treatment of TC cooling, however, was arrived at through the combination of weak wind forcing from NAM (max winds ~10 m s^{-1} too low) and a broad initial thermocline, thus providing a right answer for the wrong reasons. Some issues with SST cooling from ROMS remain, including insufficient cooling in the southern MAB and surface waters warming too quickly post-storm. Further improvements may be realized with:

1) Better initialization to resolve and maintain the sharp initial thermocline and abundant bottom cold water.

2) Better mixing physics/turbulence closure schemes to accurately widen and deepen the thermocline upon storm forcing.

3) More accurate wind forcing and air-sea flux coefficients.

These suggestions are consistent with the recommendations of Halliwell et al. (2011), who studied Hurricane Ivan (2004) in detail as it moved over the relatively deeper and less stratified waters of the Gulf of Mexico. Future research will be conducted to test these ocean model improvements.

Other future work is three-fold. First, better ocean data, e.g. more coastal ocean profile time series from flexible platforms like underwater gliders, will be needed to better spatially validate ocean models and identify critical coastal baroclinic processes. Second, Glenn et al. (2016) identified ten additional MAB hurricanes since 1985, as well as Super Typhoon Muifa (2011) over the Yellow Sea, that exhibited ahead-of-eye-center cooling in stratified coastal seas. In-depth investigation of these storms, the response of the coastal baroclinic ocean, and the feedbacks to storm intensities will be crucial.

Finally, movement towards a fully coupled modeling system is critical. Studies like this

help isolate specific processes that components of coupled models should simulate.

Table 2.1 List of model sensitivities, grouped by type. Name of sensitivity is on left, details of sensitivity with WRF namelist option on right. Control run listed last.

Sensitivity	WRF Namelist Option
A. Model Configuration	
1. Horizontal resolution (*dx*)	3 km vs. 6 km
2. Vertical resolution (*e_vert, eta_levels*)	51 vs. 35 vertical levels
3. Adaptive time step (*use_adaptive_time_step*)	on vs. off
4. Boundary conditions (update frequency, *interval_seconds*)	3 vs. 6 hours
5. Digital Filter Initialization (DFI, *dfi_opt*)	on (dfi_nfilter=7) vs. off
B. Atmospheric/Model Physics	
6-7. Microphysics (*mp_physics*)	6 (WRF Single-Moment 6-class) vs. 16 (WRF Double-Moment 6-class) vs. 30 (HUJI spectral bin microphysics, 'fast')
8-9. Planetary boundary layer scheme (*bl_pbl_physics*)	5 (Mellor-Yamada Nakanishi and Niino Level 2.5) vs. 7 (ACM2) vs. 1 (Yonsei University)
10. Cumulus parameterization (*cu_physics*)	1 (Kain-Fritsch, *cudt*=0, *cugd_avedx*=1) vs. 0 (off)
11. SST skin (*sst_skin*)	on vs. off
12-14. Longwave radiation (*ra_lw_physics*)	1 (RRTM) vs. 5 (New Goddard) vs. 99 (GFDL) vs. 4 (RRTMG)
15-17. Shortwave radiation (*ra_sw_physics*)	1 (Dudhia) vs. 5 (New Goddard) vs. 99 (GFDL) vs. 4 (RRTMG)
18-19. Latent heat flux <0 over water (in module_sf_sfclay)	on vs. off (warm SST)
	on vs. off (cold SST)
20. Land surface physics (*sf_surface_physics*)	1 (5-layer thermal diffusion) vs. 2 (Noah)
C. Advanced Hurricane WRF (AHW) Options	
21-22. Air-sea flux parameterizations (*isftcflx*)	1 vs. 0 (warm SST) (control run: *isftcflx*=2)
	1 vs. 0 (cold SST) (control run: *isftcflx*=2)
D. Sea Surface Temperature	
23-25. SST	cold vs. warm (*isftcflx*=2)
	cold vs. warm (*isftcflx*=1)
	cold vs. warm (*isftcflx*=0)
E. Advanced Hurricane WRF (AHW) Options (12-hour later initialization)	
26. Digital Filter Initialization (DFI, *dfi_opt*)	on (dfi_nfilter=7) vs. off
27-28. 1D Ocean Mixed Layer Model (*sf_ocean_physics=1*)	on (isothermal warm initial conditions) vs. on (glider stratified initial conditions) vs. off
29-30. 3D Ocean Price-Weller-Pinkel Model (*sf_ocean_physics=2*)	on (HWRF-HYCOM initial conditions) vs. on (glider stratified initial conditions) vs. off

Table 2.2 Radius of maximum 10m winds in kilometers. Warm SST and cold SST simulations compared to b-deck data from the ATCF system database.

Radius of Maximum Wind (km)			
Time	b-deck	Warm SST	Cold SST
06UTC 27 Aug	111	107	107
12UTC 27 Aug	83	80	80
18UTC 27 Aug	83	102	104
00UTC 28 Aug	83	72	85
06UTC 28 Aug	185	74	74
12UTC 28 Aug	185	213	280

Table 2.3 Track error in kilometers as compared to NHC best track data, for the warm and cold SST simulations.

Track error (km)		
Time	Warm SST	Cold SST
06UTC 27 Aug	12	12
12UTC 27 Aug	23	23
18UTC 27 Aug	13	11
00UTC 28 Aug	16	10
06UTC 28 Aug	5	14
09:35UTC 28 Aug*	8	28
12UTC 28 Aug	25	44
13UTC 28 Aug	26	48

*landfall in NJ
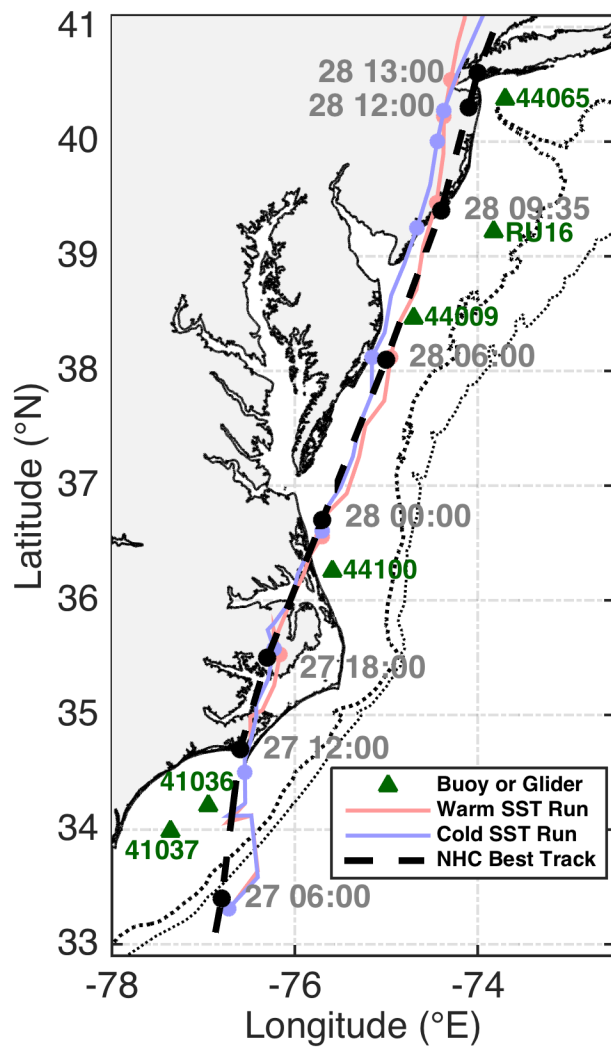
Figure 2.1 NHC best track data for Hurricane Irene in dashed black, with timing (2011 Aug DD HH:MM) labeled in gray. Tracks for warm (red) and cold (blue) SST simulations are also plotted. NDBC buoy and glider RU16 locations are shown with green triangles. 50 and 200m isobaths plotted in dotted black lines.
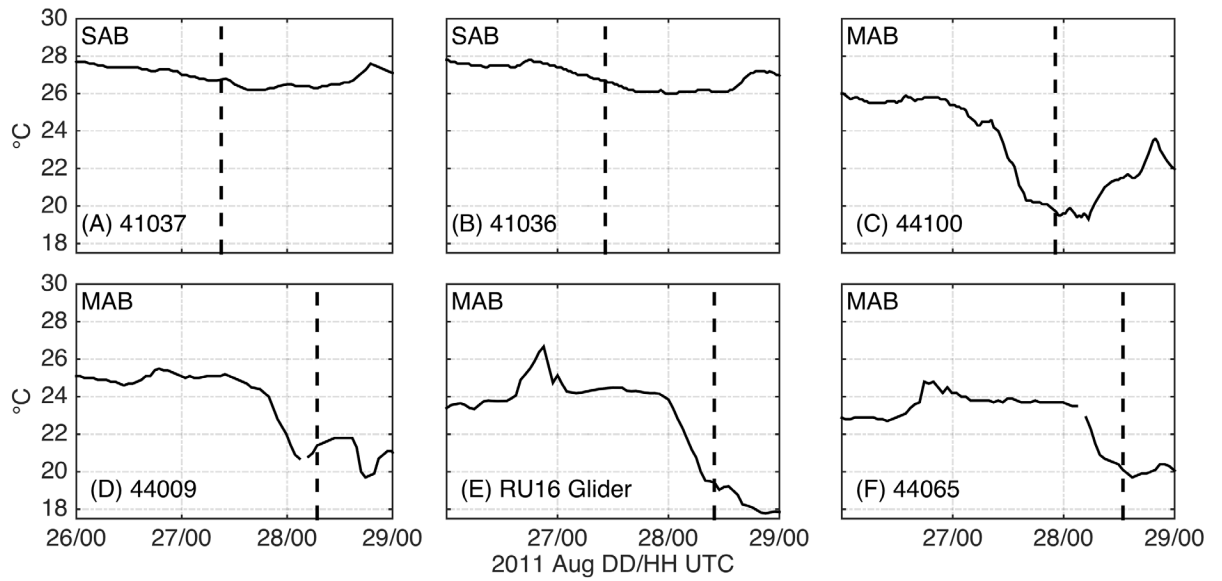
Figure 2.2 NDBC buoy and glider near surface water temperature (°C) time series. South Atlantic Bight buoys (denoted by "SAB") from south to north are 41037 and 41036, and Mid Atlantic Bight buoys and glider RU16 (denoted by "MAB") from south to north are 44100, 44009, glider RU16, and 44065. Timing of Irene's eye passage by the buoy or glider denoted with vertical dashed line.
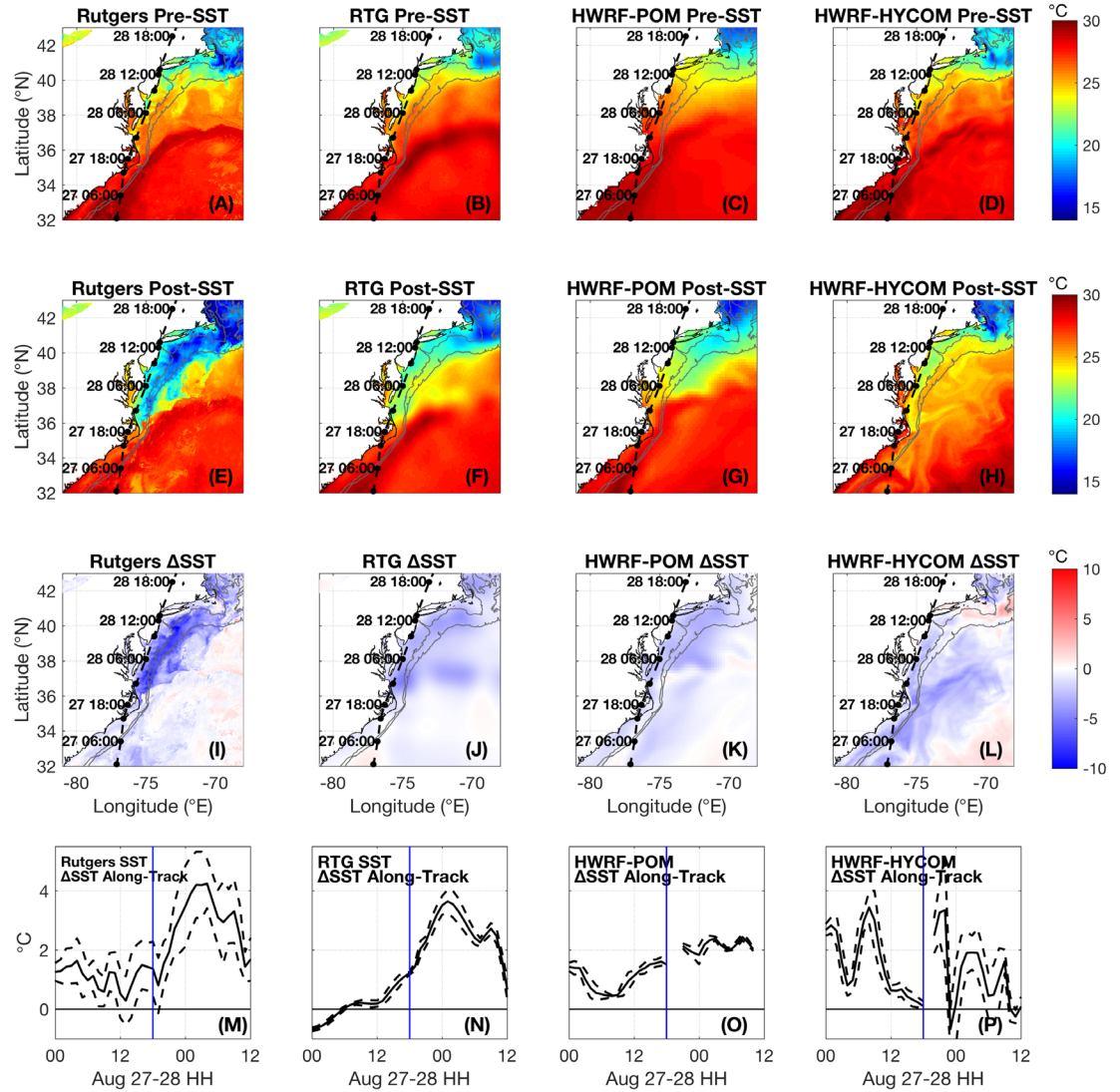
Figure 2.3 SST plots before Irene (A-D), after Irene (E-H), difference between before and after (I-L), and along-track SST change (mean within 25km of NHC best track in solid black, +/- one standard deviation in dashed black) time series (M-P) with vertical blue line dividing the first part of the time series when Irene was over the SAB, and the second part of the time series when Irene was over the MAB. First column is the new Rutgers SST composite, as described in the satellite SST section in Data and Methods above; before Irene is coldest dark pixel composite from 24-26 Aug 2011, after Irene is from 29-31 Aug 2011. Second column is the Real-Time Global High Resolution (RTG HR) SST product from NOAA; before Irene is from 26 Aug, after Irene is from 31 Aug. Third column is the operational HWRF-POM from 2011, simulation initialized at 00UTC 26 Aug 2011; before Irene is from 00UTC 26 Aug, after Irene is from 00UTC 31 Aug. Fourth column is the experimental HWRF-HYCOM from 2011, simulation initialized at

00UTC 26 Aug 2011; before Irene is from 00UTC 26 Aug, after Irene is from 00UTC 31 Aug.

Pressure and Wind Sensitivities: 8/27 2300- 8/28 1800 UTC

Group	Name	Options
Model Setup	Horizontal resolution	3km vs. 6km
	Vertical resolution	51 vs. 35 levels
	Adaptive time step	on vs. off
	B.C. (Frequency)	3 hrs vs. 6 hrs
	Digital Filter Initialization (DFI)	on vs. off
Atmospheric/ Model Physics	Microphysics	6 vs. 16
		30 vs. 16
	PBL scheme	5 vs. 1
		7 vs. 1
	Cumulus parameterization	1 vs. 0
	SST skin	on vs. off
	Longwave radiation physics	1 vs. 4
		5 vs. 4
		99 vs. 4
	Shortwave radiation physics	1 vs. 4
		5 vs. 4
		99 vs. 4
	Latent heat flux <0 over water	on vs. off (warm SST)
		on vs. off (cold SST)
	Land surface physics	1 vs. 2
Advanced Hurricane WRF	Air-sea flux parameterizations	1 vs. 0 (warm SST)
		1 vs. 0 (cold SST)
Sea Surface Temperature	SST	Warm vs. Cold (isftcflx=2)
		Warm vs. Cold (isftcflx=1)
		Warm vs. Cold (isftcflx=0)
Advanced Hurricane WRF (12-h later init.)	Digital Filter Initialization (DFI)	on vs. off
	1D Ocean Mixed Layer Model	on (isothermal warm) vs. off
		on (stratified) vs. off
	3D Ocean Price-Weller-Pinkel Model	on (HWRF-HYCOM) vs. off
		on (stratified) vs. off

Figure 2.4 Cumulative model sensitivity results, from 23UTC 27 Aug 2011 (entrance of Irene's eye center over MAB) to 18UTC 28 Aug 2011 (end of simulation). Group, name, and WRF namelist options on left with control run namelist option listed last for each sensitivity. Minimum sea level pressure (hPa) sensitivity on left and maximum sustained 10m wind (m s^{-1}) sensitivity on right.
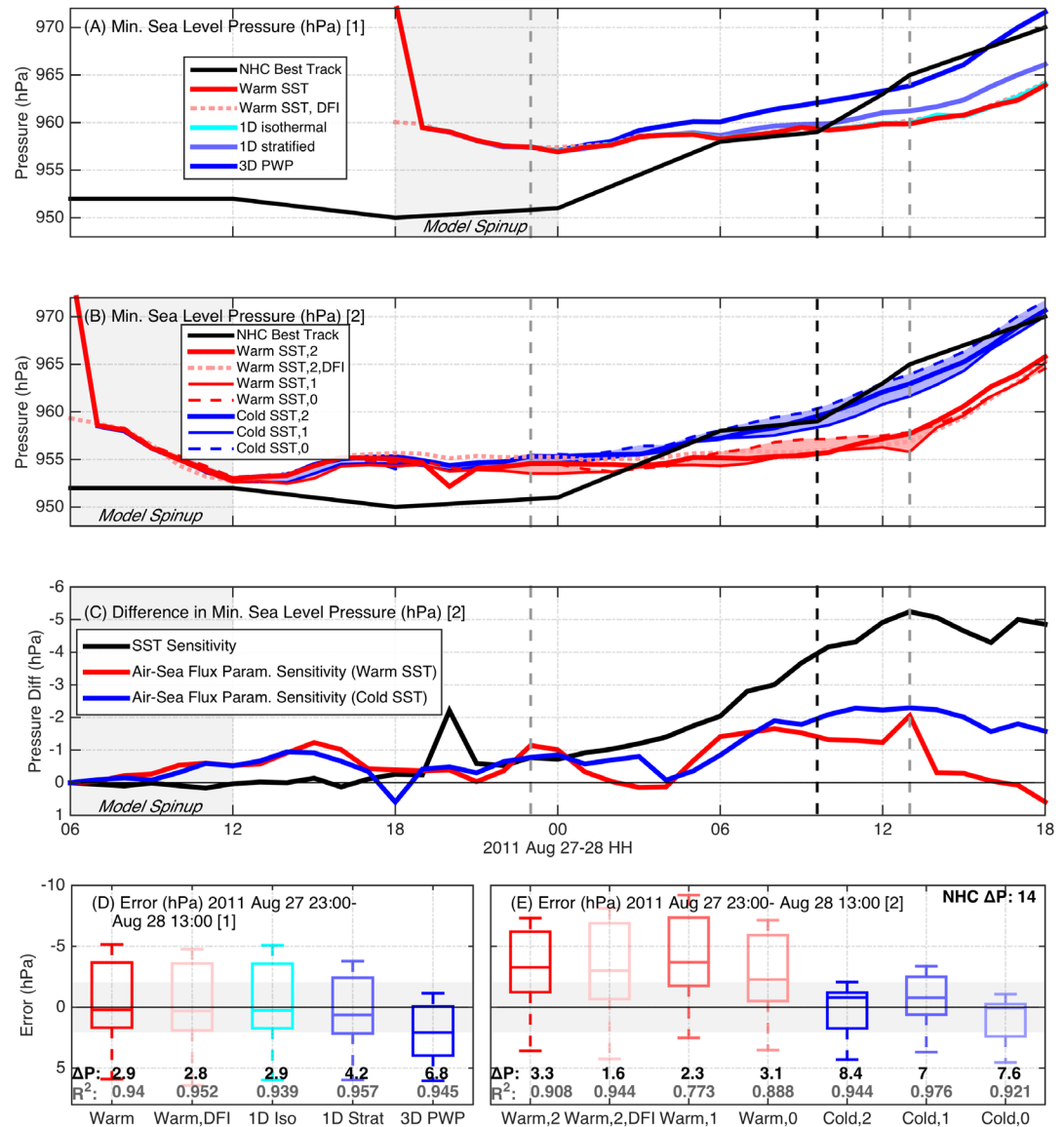
Figure 2.5 Minimum SLP (hPa) time series for WRF non-static ocean runs (A), with NHC best track in black, warm SST in red, warm SST with DFI in dotted red, 1D ocean with isothermal warm initialization in cyan, 1D ocean with stratified initialization in light blue, and 3D PWP ocean in dark blue. (B) same as (A) but for WRF static ocean runs, with warm SST with *isftcflx*=2 in red, warm SST with DFI in dotted red, warm SST with *isftcflx*=1 in thin red, warm SST with *isftcflx*=0 in dashed red, the three cold SST runs the same as warm SST but in blue lines. Vertical dashed gray lines depict start and end of Irene's presence over the MAB (23UTC 27 Aug to 13UTC 28 Aug), with vertical dashed black line depicting Irene's landfall in NJ. Model spin-up indicated as first 6 simulation hours with gray box. Difference in central pressure (C) between WRF static ocean warm and cold SST runs with *isftcflx*=2 in black, between *isftcflx*=0 and 1 for warm SST in red, and between *isftcflx*=0 and 1 for cold SST in blue. Finally, box and whisker plots of errors vs. NHC best track data for WRF static ocean runs (D) and non-static ocean (E)

during Irene's MAB presence, with r-squared values in gray and ΔP between 23UTC 27 Aug and 13UTC 28 Aug in black. NHC best track ΔP in top right of (E), and uncertainty in pressure from NHC best track data indicated by gray ribbon +/- 0 in (D) and (E).
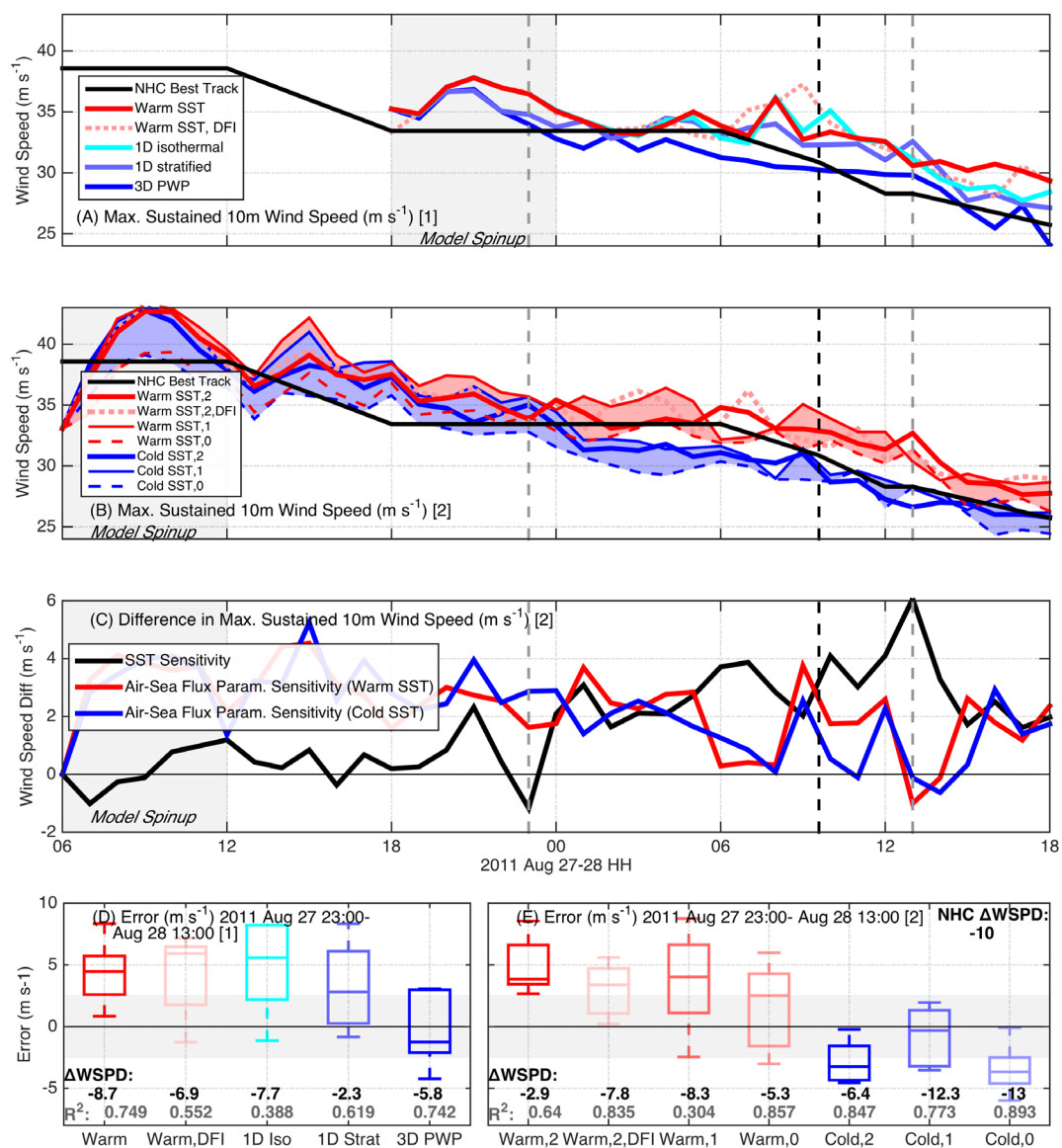
Figure 2.6 Same as Figure 2.5, but for maximum sustained 10m winds (m s^{-1}).
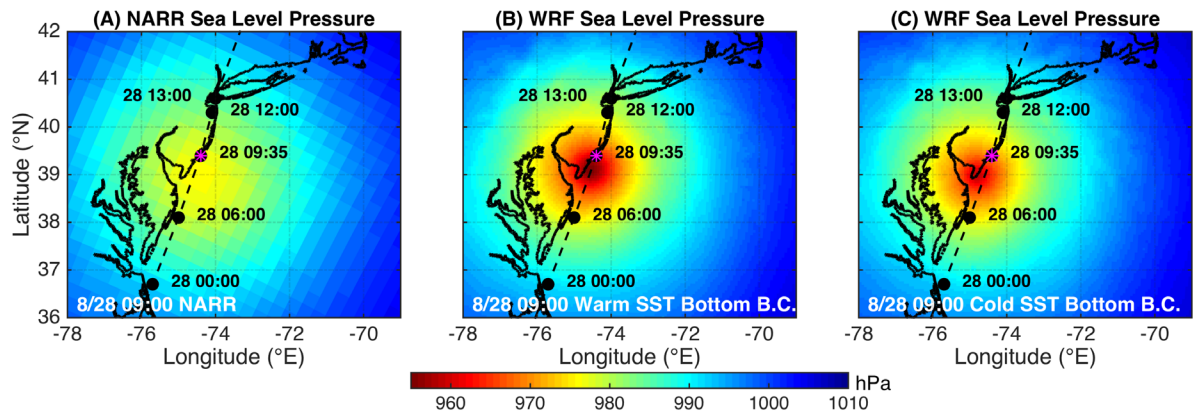
Figure 2.7 Spatial plot of SLP (hPa) at 09UTC 28 Aug just prior to NJ landfall, with Irene's NHC best track in dashed black, NARR (A), WRF with warm SST bottom boundary conditions (B), and WRF with cold SST bottom boundary conditions (C).
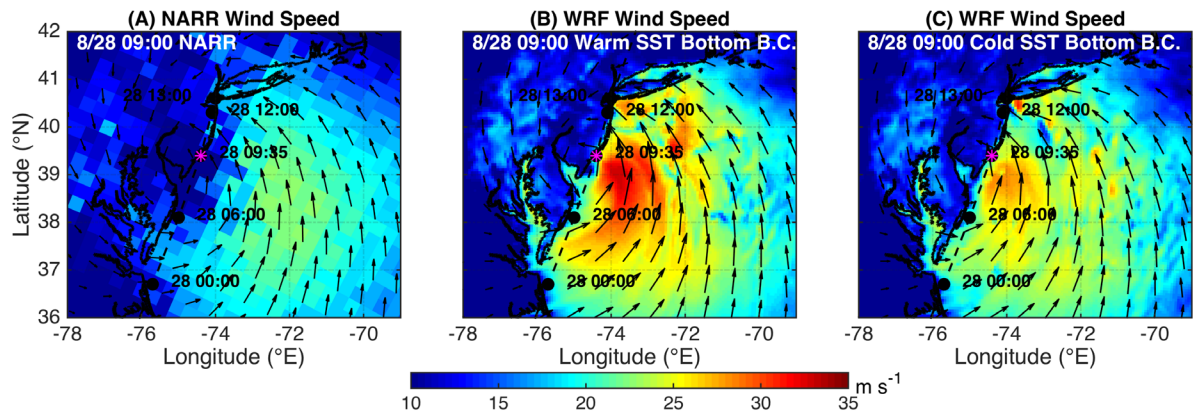
Figure 2.8 Same as Figure 2.7 but for 10m winds (m s^{-1}).
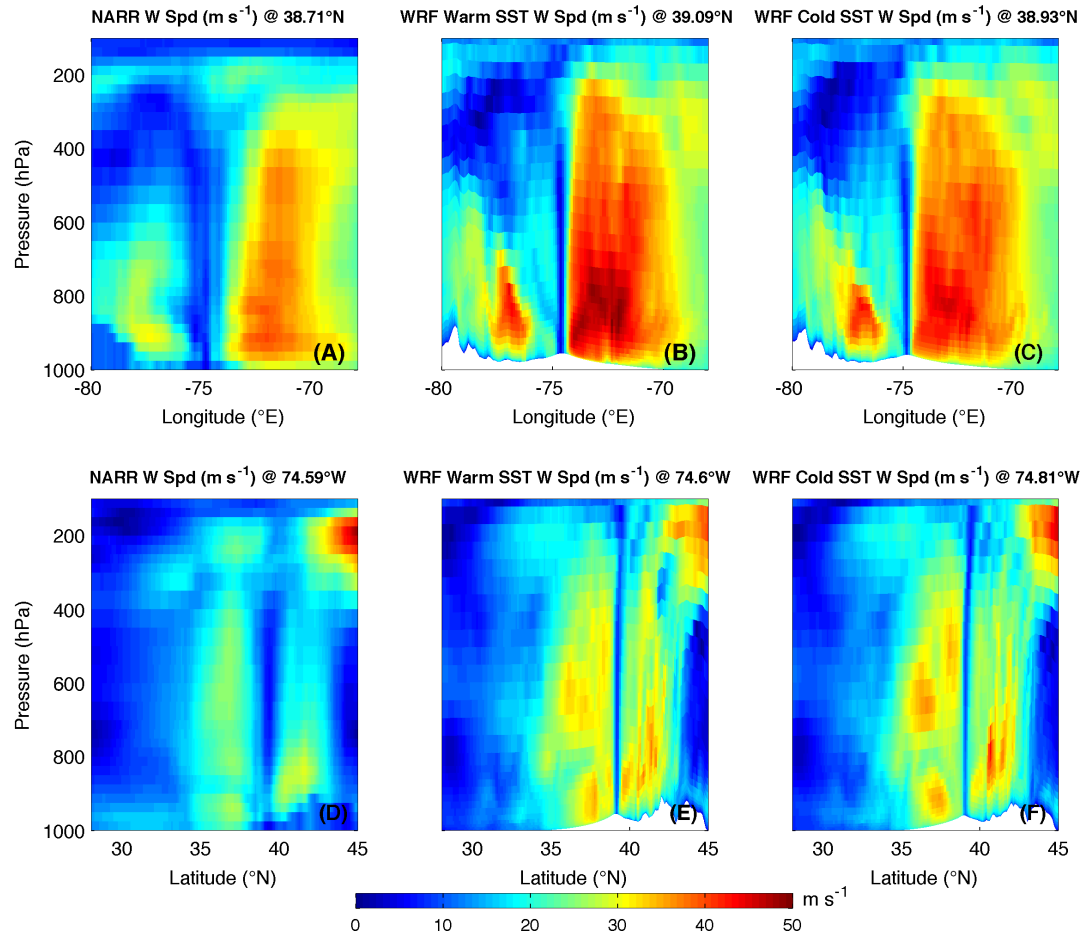
Figure 2.9 Vertical cross sections of wind speed through Irene's eye at 09UTC 28 Aug, just prior to NJ landfall. Top row (A-C) are west-to-east cross sections, while bottom row (D-F) are south-to-north cross sections. For each, latitude and longitude of eye is determined by locating the minimum SLP for NARR (A, D), WRF with warm SST bottom boundary conditions (B, E) and WRF with cold SST bottom boundary conditions (C, F).
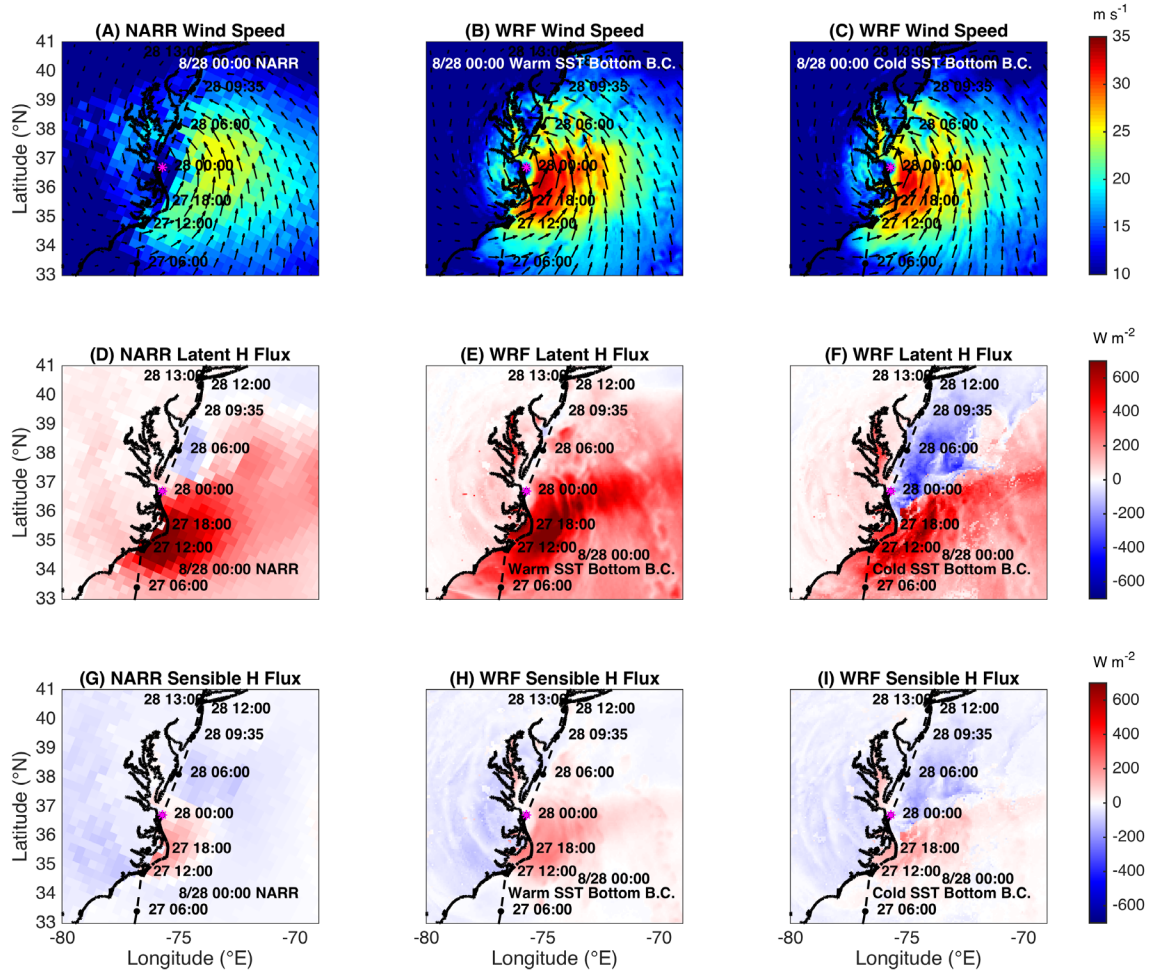
Figure 2.10 Spatial plots of 10m winds (m/s, A-C), latent heat flux at the surface (W m^{-2}, D-F), and sensible heat flux at the surface (W m^{-2}, G-I), at 00UTC 28 Aug. Fluxes are positive directed from water or land to atmosphere. NARR is first column (A, D, G) with fluxes shown as 3-hr averages ending at 00UTC 28 Aug, WRF with warm SST bottom boundary conditions is second column (B, E, H) with fluxes shown as instantaneous, and WRF with cold SST bottom boundary conditions (with negative latent heat flux allowed) is third column (C, F, I) with fluxes also shown as instantaneous.
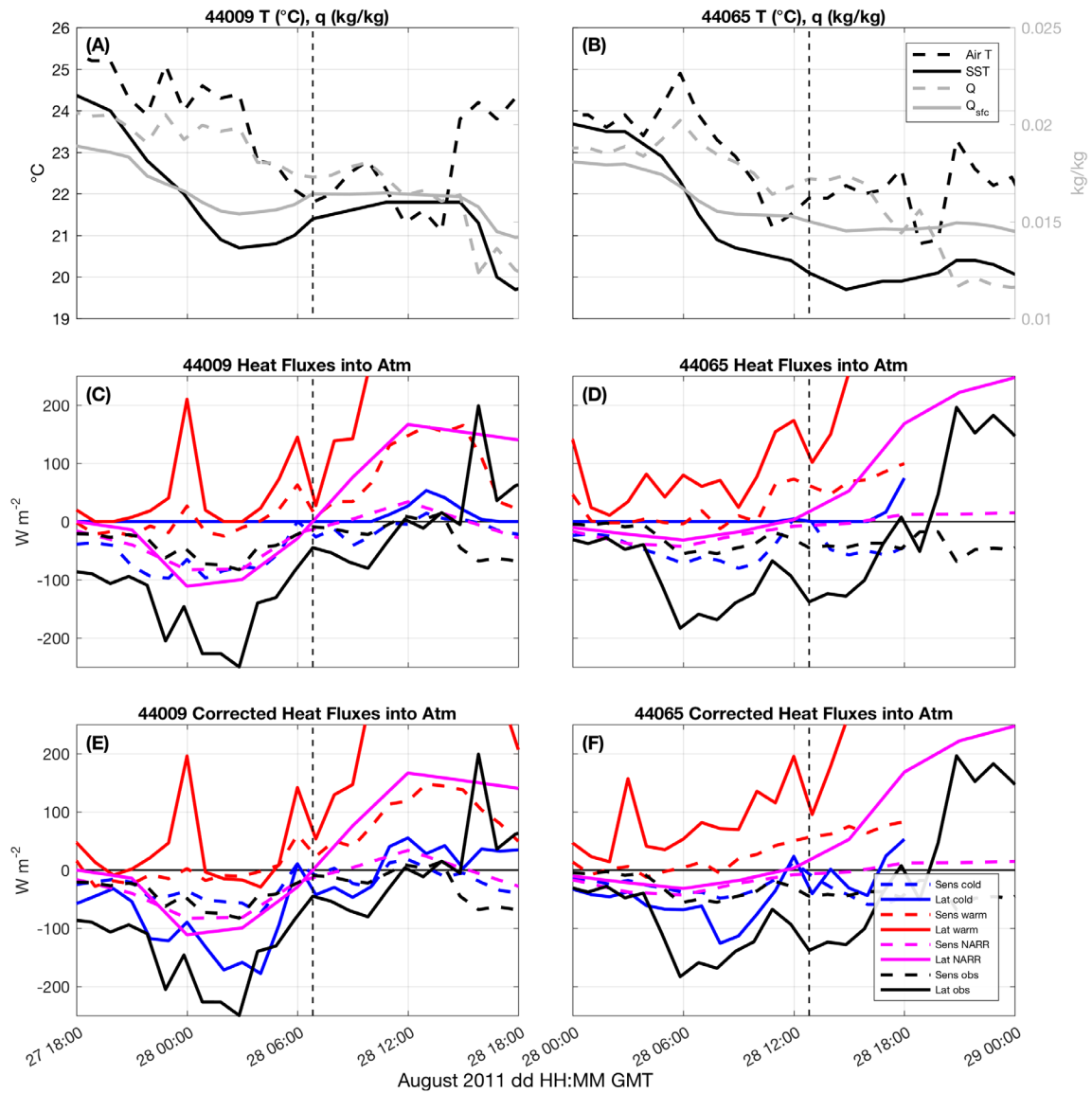
Figure 2.11 Time series of air temperature (°C, black dashed), near surface water temperature (°C, black solid), air specific humidity (kg/kg, gray dashed), and specific humidity at water surface (kg/kg, gray solid) at buoy 44009 (A) and 44065 (B), with vertical dashed line indicating timing of eye passage by that buoy (note the time axes are different for each buoy). Sensible (dashed) and latent (solid) heat fluxes (W m^{-2}) shown in (C) and (D) for observed (black), NARR (magenta, 3-hr flux averages), warm SST (red), and cold SST (blue). Fluxes are positive from ocean to atmosphere. Finally, the last row (E and F) show the same fluxes for observed and NARR as in (C) and (D) but WRF fluxes are corrected to allow for negative latent heat flux over water.
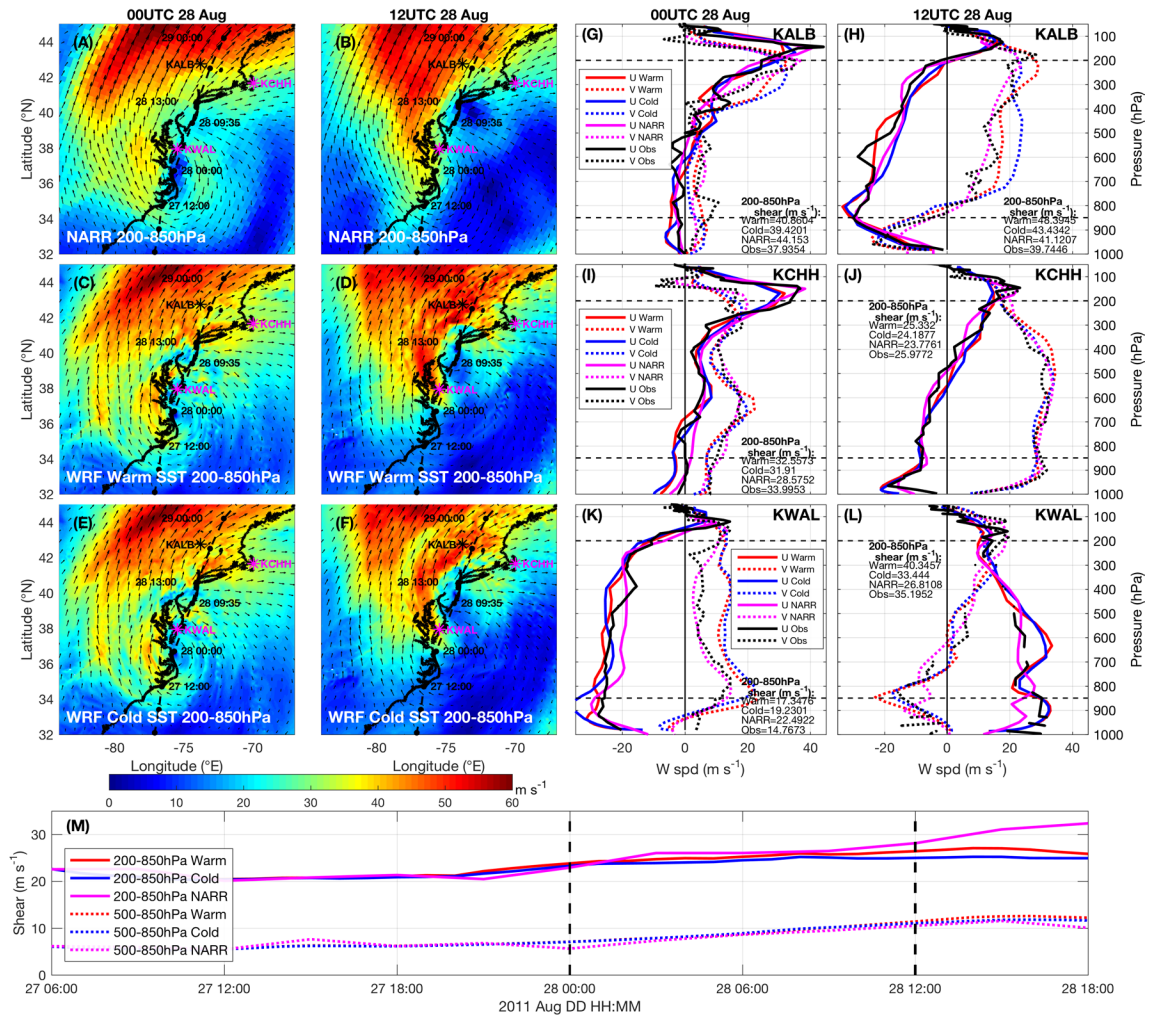
Figure 2.12 Wind shear validation, with first and third columns (A, C, E; G, I, K) at 00UTC 28 Aug and second and fourth columns (B, D, F; G, I, K) at 12UTC 28 Aug. Spatial plots are 200-850 hPa wind shear (m/s), with NARR in first row (A, B), WRF warm SST in second row (C, D) and WRF cold SST in third row (E, F). KALB, KCHH, KWAL indicated by labeled stars on maps and upper air radiosonde data at KALB (G, H), KCHH (I, J), and KWAL (K, L) plotted in third and fourth columns, with solid lines for u-winds (positive from W) and dashed lines for v-winds (positive from S), and observed in black, NARR in magenta, WRF cold SST in blue, and WRF warm SST in red. 200-850 hPa wind shear values (m s^{-1}) are labeled on graphs for observed, NARR, and WRF simulations. Time series (M) of 200-850hPa (solid) and 500-850hPa (dotted) vertical shear (m s^{-1}) for WRF warm SST (red), WRF cold SST (blue), and NARR (magenta), with vertical dashed lines indicating times of panels A-L.
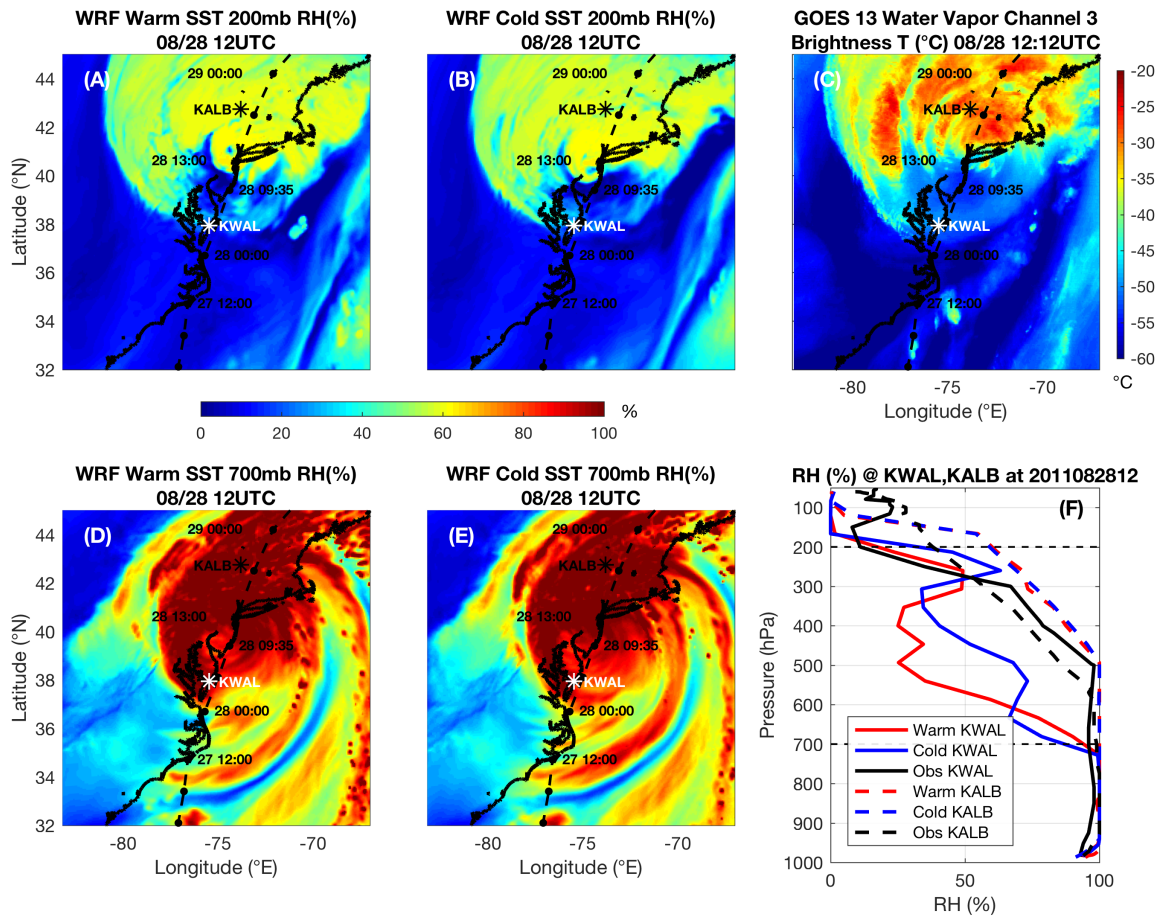
Figure 2.13 Dry air intrusion validation (relative humidity, RH, %) at 12UTC 28 Aug, with WRF warm SST in first column (A, D); cold SST in second column (B, E); and observations in third column (C, F). GOES 13 water vapor channel 3 brightness temperature (°C) at 12:12UTC 28 Aug (C) and upper air radiosonde relative humidity (%) at KWAL with observed in black, WRF warm SST in red, and WRF cold SST in blue (F). Top row (A, B) are WRF RH (%) at 200 mb for upper atmosphere, and bottom row (D, E) are WRF RH (%) at 700 mb for mid- to lower-atmosphere. KWAL location in white, and NHC best track in black in spatial plots.
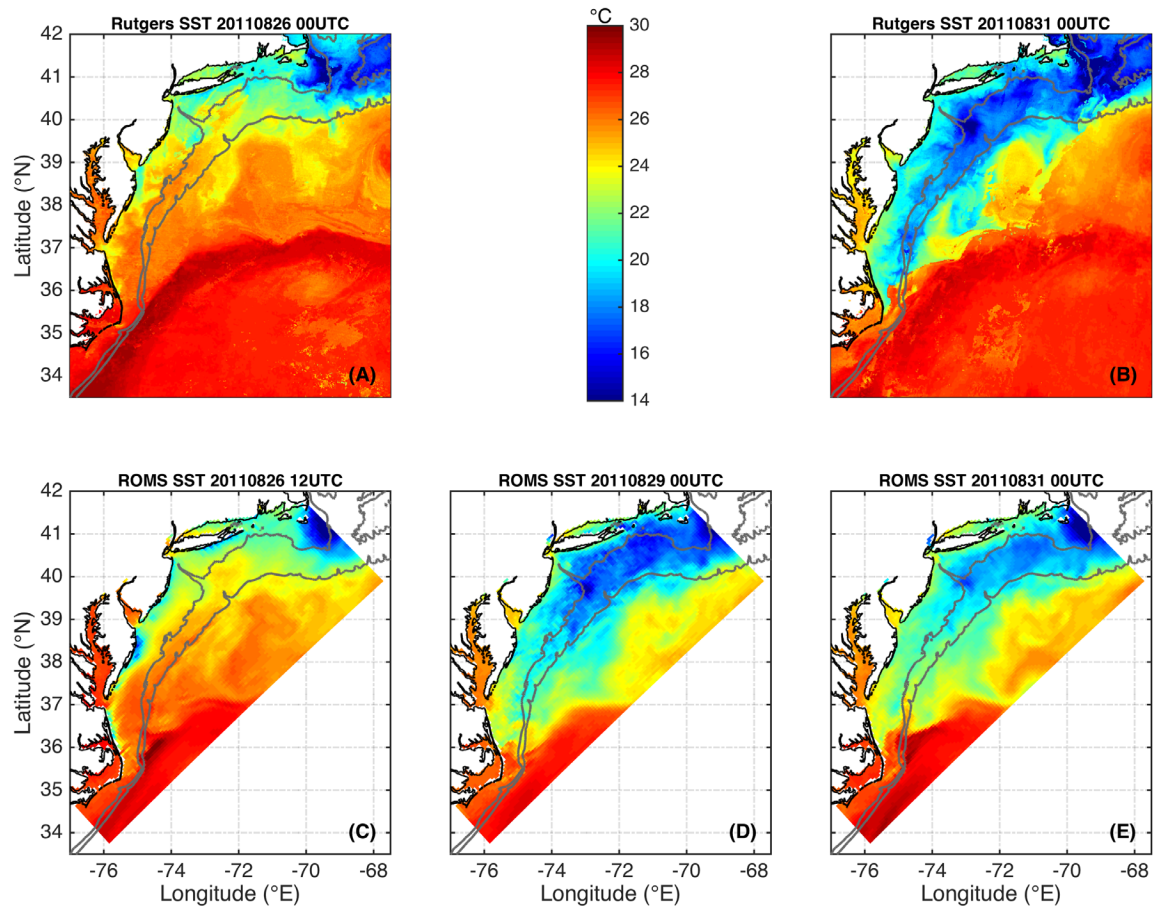
Figure 2.14 SST from the new Rutgers SST composite in top row from before Irene at 00UTC 26 Aug (A) to after Irene at 00UTC 31 Aug (B). Bottom row is water temperature of top layer from a simulation using the ROMS ESPreSSO grid, with before Irene at 12UTC 26 Aug (simulation initialization) on left (C), just after Irene at 00UTC 29 Aug in middle (D), and well after Irene at 00UTC 31 Aug on right (E).

Chapter 3

Spatiotemporal variability of stratified coastal ocean cooling processes in Hurricane Irene (2011) and Tropical Storm Barry (2007)

3.1 Introduction

Baroclinic coastal ocean mixing and cooling processes have been identified in Hurricane Irene (2011), described in detail in [*Glenn et al.*, 2016]. The ahead-of-eye-center cooling signal that resulted from the baroclinic coastal ocean mixing processes was found to be present in 11 Mid-Atlantic Bight (MAB) storms since 1985, and also in Super Typhoon Muifa (2011) in the Yellow Sea between eastern China and Korea. Further, this ahead-of-eye-center cooling was found to have a large impact on Hurricane Irene's intensity, larger than any other WRF parameter tested [Chapter 2, *Seroka et al.*, 2016].

Many questions in this study remain. First, it is not known whether the ahead-of-eye-center cooling had an impact on the intensities of the other 10 MAB storms and Typhoon Muifa. To what degree was this impact? Extensive sensitivity studies like the one performed in Chapter 2 here, and published in [*Seroka et al.*, 2016], would need to be performed to investigate these intensity impacts. These impact studies will be left for future work.

Second, it is not known if the same or different cooling processes occurred in the other 10 MAB storms and in Typhoon Muifa. What were the dominant momentum balances that occurred in these storms? Was the cross-shelf balance onshore wind stress balanced by offshore pressure gradient force, resulting in the offshore bottom currents opposing the onshore surface currents and enhancing shear-induced mixing? Did mixing dominate advection in these storms? Did these processes lead to the ahead-of-eye-center cooling signal identified? What was the spatial variability of the cooling processes, both

cross-shelf and along-shelf, for all storms including Irene? How did the processes over the shallow water on the shelf compare to those over the deep water? These questions will guide this chapter's work described below.

Standard operational model annual performance metrics are based on the mean across all storms simulated during one or several hurricane seasons (e.g. [*Kim et al.*, 2014; *Tallapragada et al.*, 2014; *Cangialosi and Franklin*, 2016]). While this method is effective in testing overall performance of a model, it tends to wash out any storm "personalities"—that is, unique characteristics—in both the atmosphere and the ocean. The full range of storm personalities represent the full range of storm air-sea feedbacks that models should capture and resolve. Therefore, it is critical to not only improve models incrementally based on the mean in an operational environment (e.g. [*Kim et al.*, 2014; *Tallapragada et al.*, 2014; *Cangialosi and Franklin*, 2016]), but also to investigate individual case studies and processes that models may or may not be correctly resolving (e.g. [*Glenn et al.*, 2008, 2016; *Lin et al.*, 2009; *Sanabia and Jayne*, 2014; *Jaimes and Shay*, 2015; *Seroka et al.*, 2016]).

In order to better understand the baroclinic ocean response for different storms, further investigation was performed on Hurricane Irene and Tropical Storm Barry (2007), one of the other 10 MAB storms. For both of these storms, Rutgers University underwater gliders were deployed on the MAB continental shelf. Irene had a more inshore track northward through the MAB and Barry tracked farther offshore along the shelf break (Fig. 3.1). Further, Irene occurred in late August toward the end of the MAB summer stratified season, while Barry occurred in early June, during the beginning of the summer stratified season. However, the intent is not to perform direct comparisons

between the two storms, as this would introduce several uncontrollable variables and not be a fully controlled experiment. Rather, the objective is to better understand the conditions in both the atmosphere and ocean that lead to the baroclinic coastal ocean cooling processes, ahead-of-eye-center cooling, and impact on storm intensities that have been identified in Irene. This chapter will investigate the details of and variability in the dominant processes—in both the cross- and along-shelf directions—for both Irene and Barry.

By studying the spatiotemporal variability in these baroclinic coastal ocean cooling tropical cyclone (TC) processes, the aim will be to 1) inform sampling strategies for future coastal ocean observatories for TCs, and 2) improve the modeling of the full range of stratified coastal ocean TC responses. These two implications will be more fully addressed in Section 3.4, Summary and Discussion below.

3.2 Data and Methods

3.2.1 High Frequency (HF) Radar

Hourly surface ocean current data, 1-hr center-averaged, from a network of CODAR Ocean Sensors SeaSonde HF Radar stations [*Barrick et al.*, 1977] along the MAB coast were used in this chapter. Surface current map data have a nominal 6km spatial resolution (Fig 3.1).

3.2.2 Gliders

Teledyne-Webb Research (TWR) Slocum gliders, autonomous underwater vehicles (AUVs), were used in this chapter [*Schofield et al.*, 2007; *Glenn et al.*, 2008, 2016; *Ruiz et al.*, 2012; *Miles et al.*, 2013, 2015]. Rutgers University Gliders RU16 (Irene) and RU17 (Barry) data were analyzed. Both gliders were equipped with a Seabird

unpumped conductivity, temperature, and depth (CTD) sensor, measuring temperature, salinity, and water depth.

Depth- and time-averaged velocity calculations were performed using a dead-reckoning technique, a method typically used for underwater gliders (e.g. [*Glenn et al.*, 2016] and references within). To estimate bottom layer currents at the glider location, a combination of dead-reckoned depth-averaged glider currents and HF radar surface currents are used (Fig. 3.1). This method assumes that the HF radar surface currents are representative of the currents in the surface mixed layer above the thermocline. See [*Glenn et al.*, 2016] for detailed methods and equations used to calculate bottom layer currents.

3.2.3 Bathymetry

U.S. Coastal Relief Model data from the NOAA National Centers for Environmental Information were used for water depth and coastlines throughout this chapter [*NOAA National Centers for Environmental Prediction*, 2016].

3.2.4 Satellite SST

Advanced Very High Resolution Radiometer (AVHRR) data were used for ocean model SST verification. Techniques empirically-derived for the MAB to remove bright cloud covered pixels and retain darker ocean pixels were used to decloud AVHRR data.

3.2.5 Regional Ocean Modeling System (ROMS): ESPreSSO

Ocean model simulations were conducted using ROMS [*Haidvogel et al.*, 2008], a free-surface, sigma coordinate, primitive equation ocean model (code available at http://www.myroms.org). ROMS has been used for a wide variety of coastal applications. Specifically, ESPreSSO (Experimental System for Predicting Shelf and Slope Optics)

model [*Wilkin and Hunter*, 2013], covering the MAB from Cape Cod to south of Cape Hatteras, and from the inland bays to beyond the shelf break, was used for simulations. The ESPreSSO grid has a horizontal resolution of 5km and 36 vertical levels in a terrain-following s-coordinate system. The following were used in the ESPreSSO simulations: initial conditions developed from an ESPreSSO grid ROMS run with strong constrained four-dimensional variational (4D-Var) data assimilation; atmospheric forcing from North American Mesoscale (NAM) 12km 3-hourly forecast data, using the COARE bulk formulae [*Fairall et al.*, 2003] to calculate surface momentum and buoyancy fluxes; boundary conditions are daily two-dimensional surface elevation and three-dimensional velocity, temperature, and salinity fields from the Hybrid Coordinate Ocean Model (HYCOM) Navy Coupled Ocean Data Assimilation (NCODA) forecast system; river inflows from the seven largest rivers, using daily average U.S.G.S. discharge data; tidal boundary conditions from the ADvanced CIRCulation (ADCIRC) tidal model; and vertical turbulence diffusivity using the general length scale method k-kl type vertical mixing scheme [*Umlauf and Burchard*, 2003; *Warner et al.*, 2005].

For Barry, the ROMS ESPreSSO simulation was initialized at 1200 UTC on May 29, 2007 and ended at 1200 UTC on June 8, 2007, with storm eye passage by glider RU17 at 1700 UTC on June 4, 2007, just over five days into the simulation. For Irene, the ROMS ESPreSSO simulation was initialized at 1200 UTC on August 24, 2011 and ended at 0000 UTC on September 3, 2011, with storm eye passage by glider RU16 at 1200 UTC on August 28, 2011, exactly four days into the simulation.

The depth-averaged momentum balance terms were direct output from the ROMS simulations, and the equation is as follows:

$$\underbrace{\frac{\partial u}{\partial t}}_{\text{Acceleration}} = \underbrace{-\frac{\partial(uu)}{\partial x} - \frac{\partial(vu)}{\partial y}}_{\text{Horizonal advection}} - \underbrace{\frac{1}{\rho_0}\frac{\partial P}{\partial x}}_{\text{Pressure gradient}} + \underbrace{\left(\underbrace{\frac{\tau_s^x}{h\rho_0}}_{\text{Surface}} - \underbrace{\frac{\tau_b^x}{h\rho_0}}_{\text{Bottom}}\right)}_{\text{Stress}} + \underbrace{fv}_{\text{Coriolis}} \qquad (1)$$

where u and v are the along-shelf and cross-shelf components of velocity respectively, t is time, P is pressure, ρ_o is a reference density, τ_s and τ_b are surface (wind) and bottom stresses, h is water column depth, and f is the latitude-dependent Coriolis frequency. Horizontal diffusion was small and neglected here, as in [*Glenn et al.*, 2016].

The temperature rate equation terms to diagnose advection vs. mixing were also direct output from ROMS. The equation is as follows:

$$\frac{\partial T}{\partial t} = -\frac{\partial(uT)}{\partial x} - \frac{\partial(vT)}{\partial y} - \frac{\partial(wT)}{\partial z} + \frac{\partial A_{kt}\frac{\partial T}{\partial z}}{\partial z} + \mathcal{D}_T + \mathcal{F}_T \qquad (2)$$

with the following surface and bottom boundary conditions:

$$\left(A_{kt}\frac{\partial T}{\partial z}\right)_{z=0} = \frac{Q_{\text{net}}}{\rho_0 C_p} \qquad (3)$$

$$\left(A_{kt}\frac{\partial T}{\partial z}\right)_{z=-h} = 0 \qquad (4)$$

Here, T is the temperature, t is time, u, v, and w are the along-shelf, cross-shelf and vertical components of velocity. A_{kt} is the vertical diffusivity coefficient, $\mathcal{D}_T$ is the horizontal diffusion term and $\mathcal{F}_T$ is friction. Q_{net} is the surface net heat flux, ρ_0=1025, kg m^{-3} is a reference density, C_p=3985 J (kg °C)$^{-1}$ is the specific heat capacity of seawater and h is the water depth. Horizontal diffusion again was small and neglected here, again as in [*Glenn et al.*, 2016].

3.3 Results

3.3.1 Observations

Glenn et al., 2016 used HF radar and glider RU16 data to determine surface, depth-averaged, and bottom currents at the glider location during Irene. Part of the time series is repeated here in Fig. 3.1 for ease of comparison to similar analysis for Barry. At 0600 UTC on August 28, 2011, less than four hours before Irene's NJ landfall and eye passage by glider RU16, surface ocean currents were directed onshore and upshelf, aligning close to the onshore winds ahead of Irene's eye (Fig. 3.1 top left). Current magnitudes at this time approached 1 m s^{-1}. At 0200 UTC on June 4, 2007, a full 15 hours before Barry's eye passage by glider RU17, surface ocean currents were in a very similar direction, onshore and upshelf.

Time series of temperature profiles at the glider locations below the surface current maps indicate initially very strong stratification and an eventual breakdown in stratification upon storm forcing. For Irene in late August, surface mixed layer temperatures approached 25°C to ~10-15m depth, and bottom MAB Cold Pool temperatures were less than 10°C. For Barry in early June, surface mixed layer temperatures down to ~10-15m depth were approaching 16°C with bottom MAB Cold Pool temperatures again less than 10°C. For Irene, the thermocline (black contour) deepened to ~30m depth and surface mixed layer temperatures cooled to ~17°C, with much (~5°C, or ~75%) of the cooling occurring ahead-of-eye-center. For Barry, the thermocline (black contour) deepened briefly to 25m depth and surface mixed layer temperatures cooled to nearly 14°C, with 100% of the cooling at RU17 occurring ahead-of-eye-center.

Cross-shelf and along-shelf surface (red), depth-averaged (green), and bottom (blue) current time series are depicted in the two panels below the temperature time series

in Fig. 3.1. For Irene observation results, currents in Earth coordinates are rotated 31°
clockwise from north to attain cross- and along-shelf components. For Barry observation
results, currents in Earth coordinates are rotated 50° clockwise from north to attain cross-
and along-shelf components. For both Irene and Barry, red surface currents peaked
onshore ahead-of-eye-center, and blue bottom currents peaked offshore at the same time
yet with a bit of a lag in set up. For Irene, along-shelf currents were very small ahead-of-
eye-center, but for Barry, along-shelf surface currents to the northeast peaked ahead-of-
eye-center and bottom currents peaked just before. The bottom right panel in Fig. 3.1
shows a calculation of surface to bottom shear, combining both the along- and cross-shelf
components. Maximum shear occurred at the same time as maximum surface cooling and
thermocline deepening, and well before eye passage. For both storms, observations
indicate a two-layer circulation, with surface currents onshore and bottom currents
offshore, enhancing the shear and resultant mixing and cooling. For Barry, a similar
surface to bottom shear profile occurred in the along-shelf direction.

3.3.2 Modeling

In order to investigate in more detail the details of the baroclinic processes and
mixing that occurred in Irene and Barry, including momentum balance analysis and the
temperature diagnostic equation for mixing vs. advection comparisons, ROMS
ESPreSSO simulations were performed. Pre-storm SST maps and stratification in
existing ROMS ESPreSSO real-time runs were evaluated to determine sufficient model
initialization (not shown). Once this evaluation was performed and results were found to
be satisfactory for model initialization, the ROMS simulations were executed, as
described in Section 3.2.5 above.

3.3.2.1 Model vs. Observations: Irene

A pre-storm map of SST over the MAB from AVHRR at 0742 UTC on August 24, 2011 (Fig. 3.2 left) shows coastal upwelling along the NJ, DE, and MD coastlines, with a warm tongue of SST through the southern MAB and extending offshore of the 50m isobath and into the northern MAB north of the Hudson Canyon. The ROMS ESPreSSO re-run SST ~four hours later (Fig. 3.2 right) shows very good agreement with AVHRR, capturing the coastal upwelling, warm tongue, Gulf Stream, and colder waters south of Rhode Island and Nantucket.

A post-storm map of SST over the MAB from AVHRR at 0828 UTC on August 29, 2011 (Fig. 3.3 left) shows a much different story, with cold <18°C SST from the mouth of the Hudson Canyon and northward, and a corridor of colder water at the 50m isobath and offshore in the southern MAB. The ROMS ESPreSSO re-run SST (Fig. 3.3 right) again shows very good agreement with AVHRR, with perhaps the only issue being not as cold water at the mouth of the Delaware Bay and in the southern MAB.

A difference map of post-storm minus pre-storm AVHRR SST (Fig. 3.4 left) shows maximum cooling (approaching 11°C) at the mouth of the Hudson Canyon and across the MAB, with less cooling in the shallow regions of the shelf and offshore in the deep water. Again, ROMS (Fig. 3.4 right) agrees very well with the AVHRR cooling map, capturing the maximum in cooling at the Hudson Canyon mouth.

Finally, RU16 glider temperature profile time series (Fig. 3.5 left) shows the same deepening of the thermocline and cooling of the surface layer as shown in Fig. 3.1. ROMS (Fig. 3.5 right) taken at the closest grid cell to the average position of RU16 during the storm period shows an initial thermocline ~10-15m too deep but with correct

surface mixed layer and bottom layer temperatures. The ROMS thermocline deepens to the correct depth during the storm, but the surface does not cool sufficiently likely due to the inadequate supply of cold bottom water at the start. Despite these deficiencies, the ROMS re-run seems to compare well with observations and should provide valuable details on the storm response processes.

3.3.2.2 Model vs. Observations: Barry

A pre-storm map of SST over the MAB from AVHRR at 0559 UTC on June 2, 2007 (Fig. 3.6 left) is partially blocked by clouds but shows a warm Gulf Stream offshore, a couple Gulf Stream rings to the northwest on the shelf slope, a ribbon of colder water along the shelf break at 200m, a ribbon of warmer water inshore of the 50m isobath, and coastal upwelling east of Cape May, NJ, at the mouth of Delaware Bay, and along the Delmarva peninsula. ROMS (Fig. 3.6 right) shows good agreement with AVHRR, with a warm Gulf Stream, cold water to the north, NJ and Delaware Bay coastal upwelling, warmer mid-shelf MAB waters, and a hint of the warm Gulf Stream filament approaching the 200m isobath.

A post-storm map of SST over the MAB from AVHRR at 0207 UTC on June 5, 2007 (Fig. 3.7 left) with the same color bar as Fig. 3.6 shows cooler water over the northern MAB, and ROMS at the same time (Fig. 3.7 right) provides a similar picture. The difference maps of post-storm minus pre-storm AVHRR SST (Fig. 3.8 left), ROMS re-run at the same time (Fig. 3.8 middle), and ROMS re-run to maximize cooling (Fig. 3.8 right) highlight the cooling and warming patterns across the MAB. Although clouds block parts of the map, AVHRR shows a pattern of warming in the southern MAB and offshore, and cooling in the northern MAB and offshore. Both ROMS re-run difference

maps show more widespread cooling, with slight warming offshore NJ and off the Delmarva peninsula, and where the Gulf Stream meanders moved through time.

Finally, the profile time series of temperature at the RU17 glider location (Fig. 3.9 left) again shows surface mixed layer cooling and deepening during the storm period, as in Fig. 3.1. ROMS ESPreSSO re-run (Fig. 3.9 right) shows a thermocline initially 15-20m too deep, but surface and bottom temperatures overall correct. The resulting cooling of the surface layer occurs at about the correct time, but the warming post-storm does not occur likely due to the surface mixed layer deeper than observed.

3.3.2.3 Hövmollers: Irene

At the cross section location near RU16 noted by the northwest to southeast black dots in Figs. 3.2-3.4, Hövmollers of time (increasing up) vs. distance offshore were produced. Surface temperature (Fig. 3.10 left) shows initially warm surface water stretching from the edge of the coastal upwelling to >200km offshore. Then, SST rapidly cools across the shelf and in deep water, so that any cooling after eye passage (from NAM—two hours later than observed) is minimal. No SST cooling occurred within the coastal upwelling. Bottom temperature (Fig. 3.10 right) shows a warm downwelling bulge, starting at the coastline and extending to close to 50km offshore. The core of the MAB Cold Pool can be seen around 100km offshore. Four sample locations are noted with the vertical solid lines labeled 1) in the upwelling, 2) near RU16, 3) in the core of the Cold Pool, and 4) in deep water. These four locations will be used in the temperature diagnostic analysis, Section 3.3.4.1.

A Hövmoller of cross-shelf surface currents (Fig. 3.11 left) show onshore currents increasing at about 0000 UTC on August 28, from about 50km offshore across the shelf

and into some of the deeper water. For Irene model results, currents in Earth coordinates are again rotated 31° clockwise from north to attain cross- and along-shelf components. The onshore surface currents peak at around 0300 UTC, and then decrease a few hours before eye passage. Bottom currents (Fig. 3.12 left) are opposing offshore across the shelf and weaker than the onshore surface currents. The bottom onshore currents begin again at about 0000 UTC on August 28, and last until eye passage. After eye passage, surface currents switch to offshore, with the switch nearshore occurring a few hours after eye passage likely due to tidal influence (not shown). Bottom currents switch to onshore after eye passage almost immediately. Maximum shear from this plot occurred roughly from 0000 to 1200 UTC on August 28, and reversed from 1500 UTC on August 28 to 0000 UTC on August 29.

The along-shelf surface current Hövmoller (Fig. 3.12 left) shows northeastward currents ahead of and after eye passage, with southwestward surface currents after eye passage in deeper water. Bottom currents (Fig. 3.12 right) are southwestward ahead of eye passage and immediately after, then northeastward later at 0000 UTC on August 29. Maximum shear from this plot occurred roughly from 0600 to 1500 UTC on August 28.

Cross-shelf (Fig. 3.13 left) and along-shelf (Fig. 3.13 right) surface to bottom shear Hövmollers are the components that comprise the bulk surface to bottom shear Hövmoller (Fig. 3.14 left). This bulk shear Hövmoller shows a symmetric ~50% ahead and 50% behind eye shear pattern in deep water, consistent with [*Price*, 1981]. In the shallow water over the continental shelf, shear is skewed ahead-of-eye-center. Because in deep water the bottom layer is quiescent and in shallow water the bottom layer is moving, only qualitative comparisons between deep and shallow water can be made. Additionally,

bottom currents in shallow water are affected by opposing bottom stress, restricting any quantitative comparisons between deep and shallow water. By changing bottom currents to 0, a more evenly distributed shear pattern between ahead of and behind eye passage results (Fig. 3.14 right), showing that the opposing bottom currents in the two-layer circulation has an influence on the shear pattern.

Further, the ahead-of-eye-center cooling due to this shear is greater than behind-eye cooling (Fig. 3.10) likely because behind the eye, 1) the water column is already mixed, and stratification is weaker, and 2) shear decreases but to a greater extent than the decrease in stratification, because winds are offshore and weaker due to frictional land effects. As will be shown in the following momentum balance Hövmollers, the dominant cross-shelf momentum terms are onshore wind stress balanced by offshore pressure gradient force ahead-of-eye-center, and offshore wind stress balanced by onshore pressure gradient force behind-eye-center. This balance is likely due to the presence of the coastline and shallow bottom, in which onshore surface winds ahead-of-eye-center pile water at the coast and result in the offshore bottom current, and offshore surface winds behind-eye-center push water away from the coast and result in the onshore bottom current. In both cases—ahead-of-eye-center and behind-eye-center—a two-layer circulation occurs due to the presence of the coastline, shallow bottom, and stratified water column.

The depth-averaged cross-shelf momentum balance time series (Fig. 3.15) depicts all terms except for horizontal viscosity, which was very small. Acceleration shows a strongly tidal signal, with less onshore acceleration just before eye passage. Wind stress is strongly onshore ahead-of-eye passage, and switches to offshore after. Pressure

gradient force is offshore ahead-of-eye all the way to the shelf break, and then switches to offshore mid-shelf first and then nearshore and near the shelf break second; this pressure gradient pattern is due to coastal set up ahead-of-eye and coastal set down behind-eye. Coriolis is offshore, increasing after the eye. Bottom stress is onshore opposing the offshore bottom currents ahead-of-eye, and then switches sign after eye. Finally, advection is small and noisy, with a potential inertial response signal especially near the shelf break. The dominant cross-shelf force balance progresses from –wind stress balanced by +pressure gradient ahead-of-eye-center, to +wind stress +coriolis balanced by –pressure gradient after eye passage until 0000 UTC on August 29, and finally to a geostrophic balance of +coriolis balanced by –pressure gradient.

In the along-shelf direction, depth-averaged momentum balance terms (Fig. 3.16) are generally smaller than the cross-shelf terms. Again, acceleration has a tidal signal, but so does Coriolis. The dominant along-shelf force balance progresses from –wind stress balanced by +pressure gradient and +coriolis, to +wind stress balanced by –pressure gradient and –coriolis, and finally to +pressure gradient balanced by +/- coriolis (tidal periodicity).

3.3.2.3 Hövmollers: Barry

The time series of SST for Barry (Fig. 3.17 left) was taken at the northern WNW to ESE cross section location just north of the Hudson Canyon as indicated by the black dots in Figs. 3.6-3.8. This northern location was chosen to target the greatest SST cooling in Barry. A similar cooling signal is apparent across the shelf and even in deep water. At National Data Buoy Center (NDBC) station ALSN6, the Barry station used by [*Glenn et al.*, 2016] for the ahead-of-eye-center cooling signal, cooling (~3.5°C) was greatest. At

the warm strip of water indicated by the vertical line labeled "2", and in the deep water, total cooling was less than 1°C. The bottom temperature spatial time series (Fig. 3.17 right) shows a similar but more subtle downwelling bulge from the coast as was evident in Irene. Five sample locations are noted with the vertical solid lines labeled 1) in the nearshore maximum cooling and near ALSN6, 2) in the warm strip of water, 3) in the core of the Cold Pool, 4) near RU17, and 5) in deep water. These five locations will be used in the temperature diagnostic analysis, Section 3.3.4.2.

The cross-shore surface current time series (Fig. 3.18 left) shows onshore surface currents peaking 12-18 hours prior to eye passage, but remaining weakly onshore until eye passage. For Barry model results, currents in Earth coordinates are also rotated 31° clockwise from north to attain cross- and along-shelf components. Bottom currents (Fig. 3.18 right) show a primarily tidal signal, with alternative offshore and onshore bottom currents. Maximum shear was roughly 0600 to 1200 UTC on June 4. This maximum shear occurs when the bottom offshore currents (mainly tidal) oppose the onshore surface currents. Because the storm forcing is weaker than in Irene, the tidal signal dominates the bottom current forcing. This is consistent with the findings of [*Keen and Glenn*, 1995], who found that during a storm crossing the MAB in October 1990, the tidal signal dominated the bottom current forcing, and storm sedimentation was directly related to the tidal flow.

In the along-shelf direction, surface currents were northeastward before eye passage and southwestward after (Fig. 3.19 left). Bottom currents were southwestward the entire storm period, both before and after eye passage. One open question that remains is why? Could the Hudson Canyon be acting like a barrier, blocking bottom

currents from crossing it? A similar analysis just south of the Hudson Canyon may help answer this question.

Cross-shelf (Fig. 3.20 left) and along-shelf (Fig. 3.20 right) surface to bottom shear Hövmollers are the components that again comprise the bulk surface to bottom shear Hövmoller (Fig. 3.21 left). This bulk shear Hövmoller again shows a roughly symmetric ~50% ahead and 50% behind eye shear pattern in deep water if the time period of 0000 UTC on June 4 to 0600 UTC on June 5 is used. Again, like for Irene, shear is skewed ahead-of-eye passage in the shallow water, and by substituting 0 for bottom currents, a more (but not quite fully) symmetric shear pattern in shallow water results.

The Hövmoller cross-shelf depth-averaged momentum balance terms (Fig. 3.22) show a strongly tidal signal in the acceleration, pressure gradient, and Coriolis terms across the shelf, and in the bottom stress and horizontal advection terms very near shore. Wind stress was directed onshore ahead of eye passage and weakly offshore after. Pressure gradient was primarily tidal, with more positive offshore values along the shelf break just ahead of eye compared to after eye passage. Coriolis was largely tidal and onshore, with the maximum again at the shelf break. Bottom stress was mostly tidal, but mostly negative opposing the offshore bottom currents at about 0600 UTC on June 4 ahead of eye, when the downwelling circulation aligned with the tidal signal. Finally, horizontal advection was mostly small. The dominant depth-averaged cross-shelf force balance progressed from –wind stress balanced by +pressure gradient ahead of eye passage, to +wind stress balanced by –coriolis and +/- pressure gradient (tidal periodicity)

just after eye passage, to quasi-geostrophic balance with –coriolis balanced by +/-

pressure gradient (again tidal).

The Hövmoller along-shelf depth-averaged momentum balance terms (Fig. 3.23)

show a mostly tidally-forced signature. Acceleration was mostly tidal, with slightly more

negative onshore acceleration ahead of eye passage from 0000 to ~0900UTC on June 4.

Wind stress was southwestward ahead of eye passage and northeastward after. Pressure

gradient and Coriolis terms were primarily tidal, bottom stress was always northeastward

opposing the southwestward bottom currents, and horizontal advection was small. The

dominant along-shelf depth-averaged momentum balance progressed from –wind stress

balanced by +/- pressure gradient and +/- coriolis ahead of eye passage to +wind stress

and +coriolis balanced by –pressure gradient.

The shelf break maxima in the pressure gradient and Coriolis terms are potentially

due to the presence of a warm core ring starting pre-storm just north of the Hudson

Canyon and the northern cross section location (Fig. 3.7 left) and moving southeastward

by post-storm (Fig. 3.8 left). This ring, moving along the shelf break and beginning to

impinge onto the shelf, forces a geostrophic circulation at the shelf break front [*Zhang

and Gawarkiewicz*, 2015], which is evident at the shelf break in both the cross- and

along-shelf momentum balance Hövmollers (Figs. 3.22 and 3.23).

3.3.2.4 Temperature diagnostics: Irene

The temperature diagnostic equation terms were plotted (Fig. 3.24) at the points

indicated on Fig. 3.10 to determine the primary cause of cooling. The left panel is within

the upwelling, the second is at RU16, the third is in the MAB Cold Pool core, and the

fourth is in deep water. At the top is the full temperature rate term, in the middle is the

vertical diffusion term, and at the bottom are the vertical plus horizontal advection terms. Horizontal diffusion was not plotted, as it was very small. First, a general tidal signal is apparent in the full temperature rate term, primarily due to advection at all four locations. Cooling in the mixed layer was due to vertical diffusion at all four points, with ahead-of-eye-center cooling occurring at points #1, 2, and 3. At point 1 within the upwelling, surface mixed layer cooling stopped once the thermocline reached the bottom of the water column, as the source of cold water was removed (Fig. 3.24 left middle). At point 2, ahead-of-eye-center cooling was caused by vertical diffusion cooling being skewed ahead-of-eye-center. At point 3 in the Cold Pool core, vertical diffusion cooling was also skewed ahead-of-eye-center, with advection warming after eye passage. Finally, at point 4 in the deep water, a deep, cold quiescent bottom allowed for some cold water to entrain into the thick ~200m surface mixed layer ahead-of-eye passage.

3.3.2.5 Temperature diagnostics: Barry

The temperature diagnostic equation terms plotted for Irene at four locations in Fig. 3.24 were also plotted for Barry at five locations in Fig. 3.25. For Barry, the left panel is near ALSN6, the second panel is within the warm strip, the third panel is within the Cold Pool core, the fourth is near RU17, and the fifth is in deep water (Fig. 3.25). Again, a tidal advection signal is apparent, with vertical diffusion not having any tidal cooling/warming signal. Vertical diffusion again caused cooling in the mixed layer except at point 5 in the deep water. Point 5 looks primarily advective with a deep quiescent bottom. At points 1-4 the tidal advection cooling/warming periodicity was modulated by the vertical diffusion cooling, which looks to be skewed ahead-of-eye passage during the greatest shear period (Fig. 3.21 left).

3.4 Summary and Discussion

In this chapter, baroclinic coastal ocean cooling processes were investigated in detail for Hurricane Irene (2011) and Tropical Storm Barry (2007). More specifically, analysis investigated cross-shelf variability in the depth-averaged momentum balance terms, to determine the dominant force balance on the MAB shelf in the storms, as well as the cross-shelf variability in the temperature diagnostic equations, to determine whether mixing or advection caused the cooling observed in the storms. For Irene, it was previously found that cross-shelf two-layer surface to bottom opposing current shear was large and along-shelf surface to bottom shear was small at the RU16 glider location [*Glenn et al.*, 2016]. Here, for Barry, it was found that both the cross- and along-shelf components of the surface to bottom opposing current shear contributed to the mixing and cooling observed at the RU17 glider location.

For Irene, the dominant force balance ahead of eye passage was onshore wind stress balanced by offshore pressure gradient, and the large offshore pressure gradient term stretched across the whole shelf. The wind stress and pressure gradient terms switched directions right after eye passage and eventually became geostrophic long after the storm. For Barry, the dominant force balance on the shelf ahead of eye passage was modulated by the tides but also had the onshore wind stress term balanced by offshore pressure gradient, and again the large offshore pressure gradient term extended all the way across the shelf. The along-shelf force balance also played a role for Barry, potentially due to the location of the cross-section relative to the changing slopes of the bathymetry just north of the Hudson Canyon. In both the cross- and along-shelf directions, there was a maximum in the pressure gradient and Coriolis terms near the

shelf break, which coincided with a warm eddy moving southwestward along the shelf slope front with a geostrophic circulation.

Finally, cross-shelf variability in temperature rate diagnostic terms was investigated. For both storms in the shallow water on the shelf, vertical diffusion was the main cause of the mostly ahead-of-eye-center cooling in the surface mixed layer. Tidal periodicity of cooling/warming was apparent in the combined vertical and horizontal advection terms. Cooling in the surface layer did occur within the coastal upwelling during Irene, and the cooling stopped once the thermocline hit the bottom of the water column as the bottom cold water was also removed. In the deep water, vertical diffusion and advection were important drivers of mixed layer cooling for Irene, whereas for Barry advection was the main driver in the periodic and alternating warming/cooling near the surface.

The drivers in the major differences in coastal ocean response between Irene and Barry were storm track, size and structure of storm, and time of year. Irene had a more inshore MAB track during the late summer stratified season, whereas Barry was weaker with a farther offshore track during the early summer stratified season. Surface winds near Barry seemed to have a more along-shore component than the primarily cross-shore winds during Irene, leading to both cross- and along-shore components playing a larger role in the coastal ocean response for Barry, and a primarily cross-shore response for Irene.

There are two main implications of this study:

1) It informs sampling strategies for future coastal ocean observatories for tropical cyclones

- Should the extent of the MAB Cold Pool be targeted? Very few bottom observations exist, and this would tie in nicely with storm intensity impact studies

- Should the areas of greatest remaining uncertainty be targeted? What about near the Hudson Canyon, where the maximum cooling occurred in Irene?

2) It contributes to improvements in the modeling of the full range of stratified coastal ocean tropical cyclone response

- One can target sampling not just for improving initial conditions (data assimilation), but also for improving direct modeling and parameterizations of physical responses

Future work should explore causes of the variability in cooling and mixing found here—what were the pre-existing conditions? Did the eddy structure and presence of coastal upwelling largely affect the resulting response? Also, while this study examined in detail the cross-shelf variability in the depth-averaged momentum balance and mixing vs. advection for cooling, it did not investigate the along-shelf variability. Further, the depth-averaged momentum balances precluded any direct comparison between shallow and deep water. Future work should look to make those direct comparisons, for better understanding of the shallow water/coastal response and how it is different than the deep, ocean response. For Irene, an open question is the cause of the maximum cooling that occurred within the Hudson Canyon. Was this caused in part by the deep bathymetric canyon and thus large source of cold bottom water? Did upwelling occur due to the presence of the canyon?

The other nine MAB storms, and Super Typhoon Muifa identified by [*Glenn et al.*, 2016] that exhibited the ahead-of-eye-center cooling signal are left for investigation on what baroclinic coastal ocean cooling processes occurred in each storm. In addition, studies examining the impact of the cooling on storm intensity should be carried out for these remaining storms as well as for Tropical Storm Barry. Finally, data denial studies to isolate the impact of underwater glider data assimilation in forecast models should be performed. In the end, these studies show the true value of ocean observations and how they can improve the initialization and subsequent performance of TC forecast models.
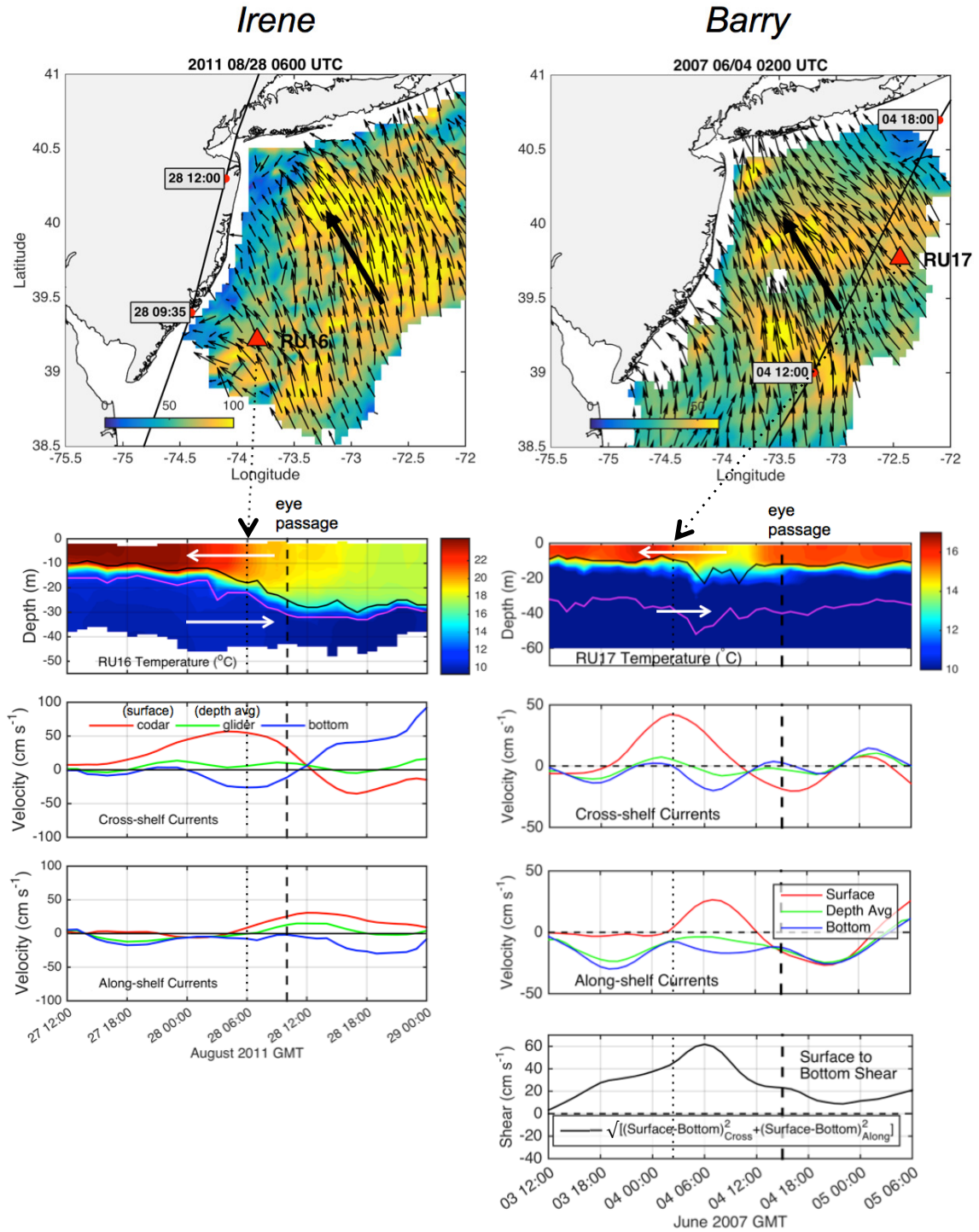
Figure 3.1 HF radar surface ocean current 1-hour center-averaged maps for Irene and Barry before eye passage by RU16 (Irene) and RU17 (Barry) (top). National Hurricane Center (NHC) best track in black, with large black arrow indicating general direction of surface currents. Location of RU16 and RU17 shown with red triangles. Time series at glider locations of temperature with thermocline depth in black contour and transition layer depth in magenta contour (second from top), cross-shelf currents (third from top),

along-shelf currents (fourth), and surface to bottom shear for Barry (bottom right). Currents and shear are smoothed using the MATLAB smooth function using a span of 8.
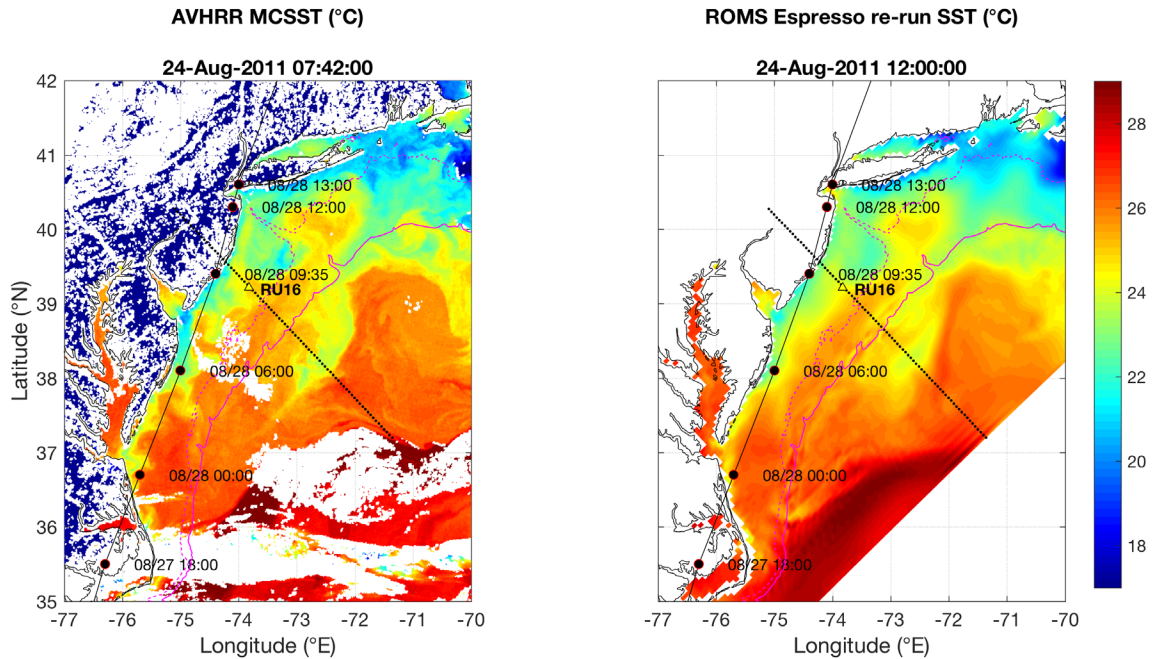
Figure 3.2 AVHRR Multi-Channel SST (MCSST) (left) and ROMS ESPreSSO re-run SST (right) pre-storm for Irene. Dashed magenta contour is 50m isobath, and solid magenta contour is 200m isobath. RU16 location throughout the storm period plotted as yellow triangle, NHC best track for Irene in black with red outlined dots, and small black dots in line northwest to southeast indicating cross section location taken for Hövmoller figures below.
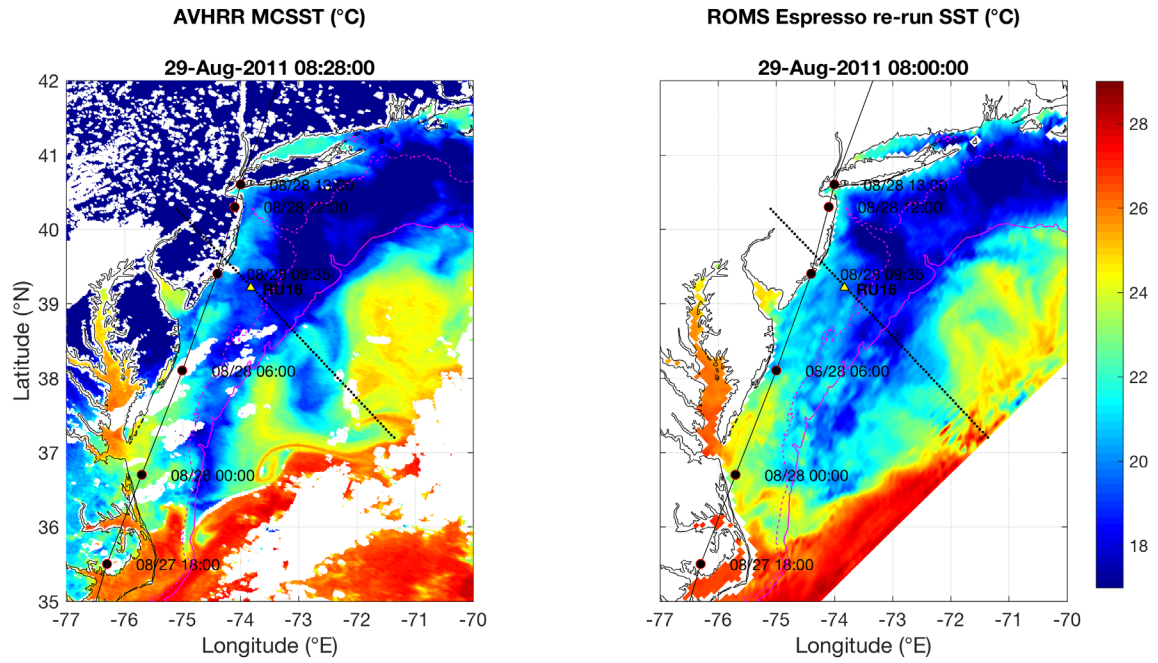
Figure 3.3 The same as Fig. 3.3, but for post-storm.
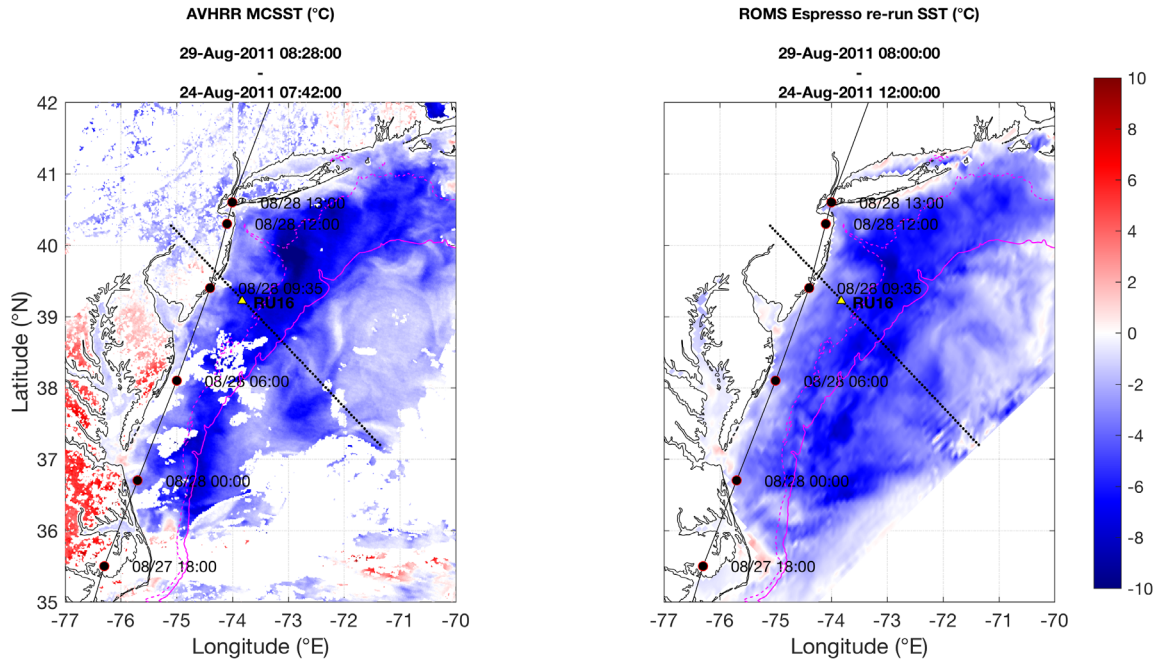
Figure 3.4 The same as Fig. 3.3, but for post-storm minus pre-storm.
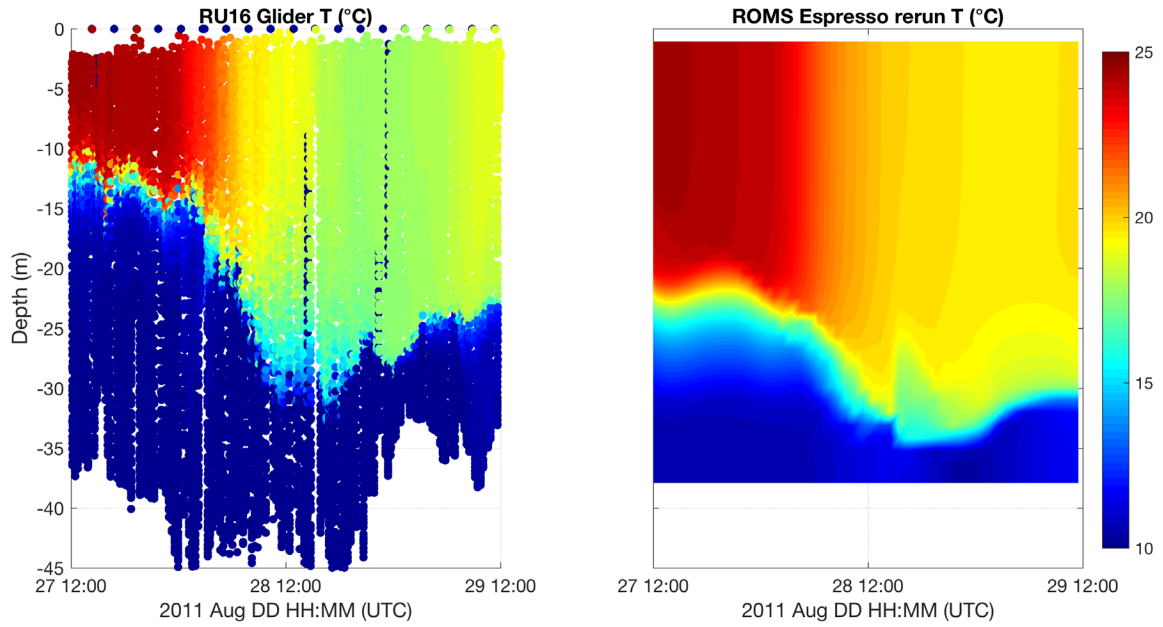
Figure 3.5 RU16 glider temperature (°C) (left) and ROMS ESPreSSO re-run temperature (°C) at the closest ESPreSSO grid point to the average RU16 glider location during the storm.

84

Figure 3.6 The same as Fig. 3.3, but for Barry. NDBC station ALSN6 and RU17 glider locations indicated with yellow triangles. Northern cross section location used for Barry plotted as west-northwest to east-southeast black dots just north of the Hudson Canyon.
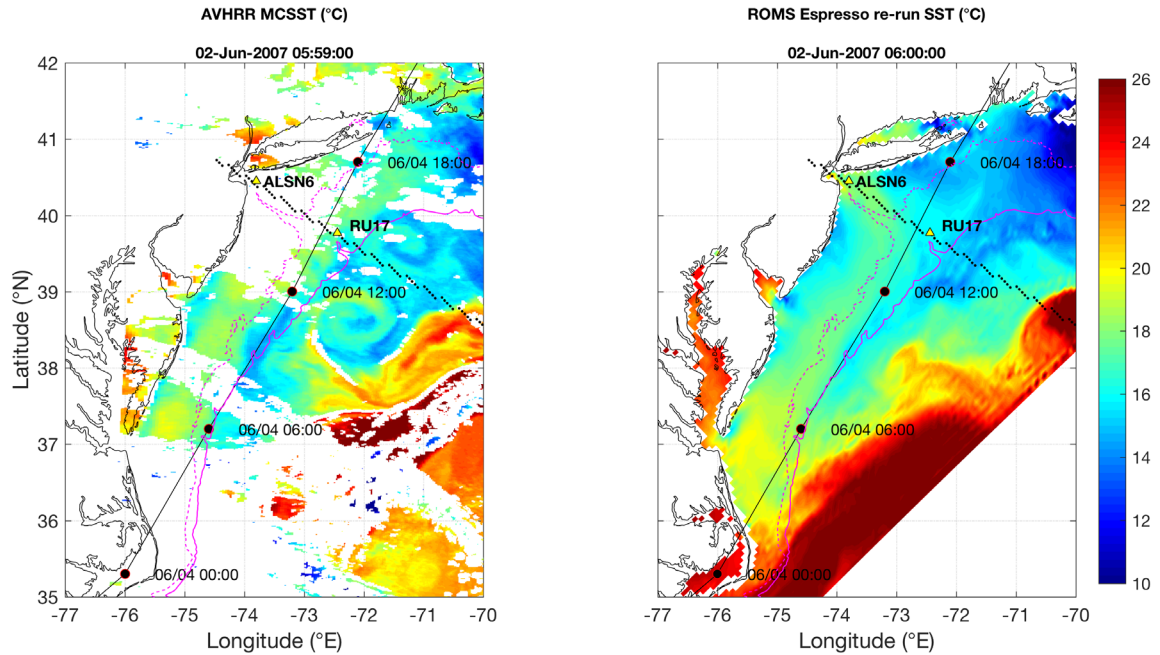
Figure 3.7 The same as Fig. 3.6, but for post-storm.

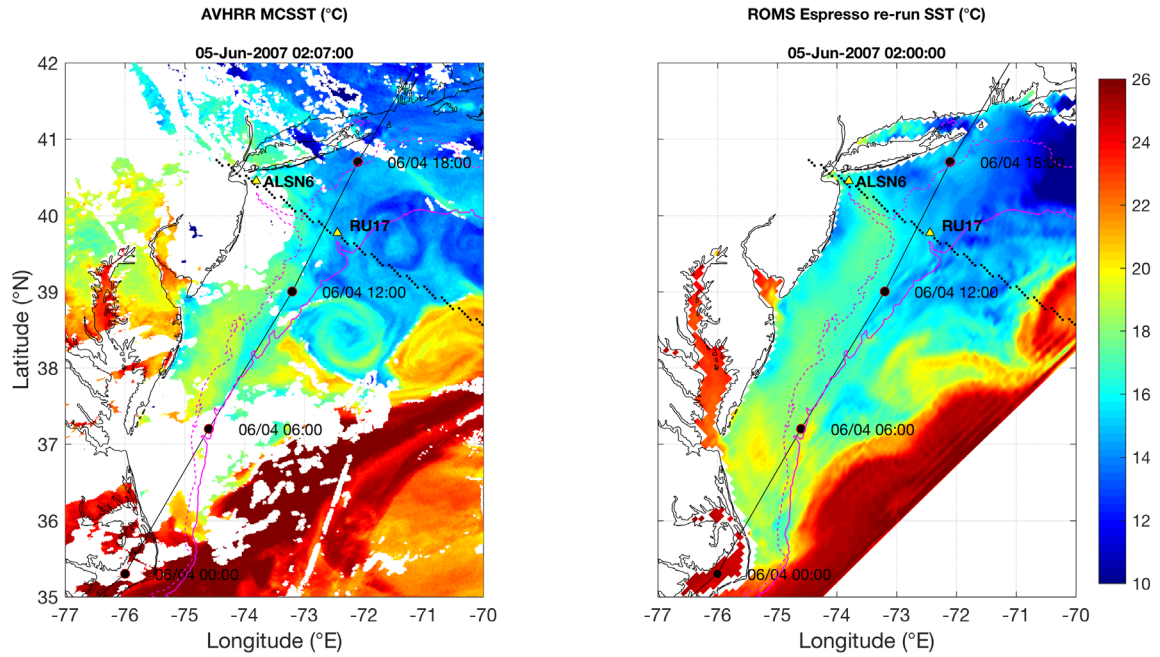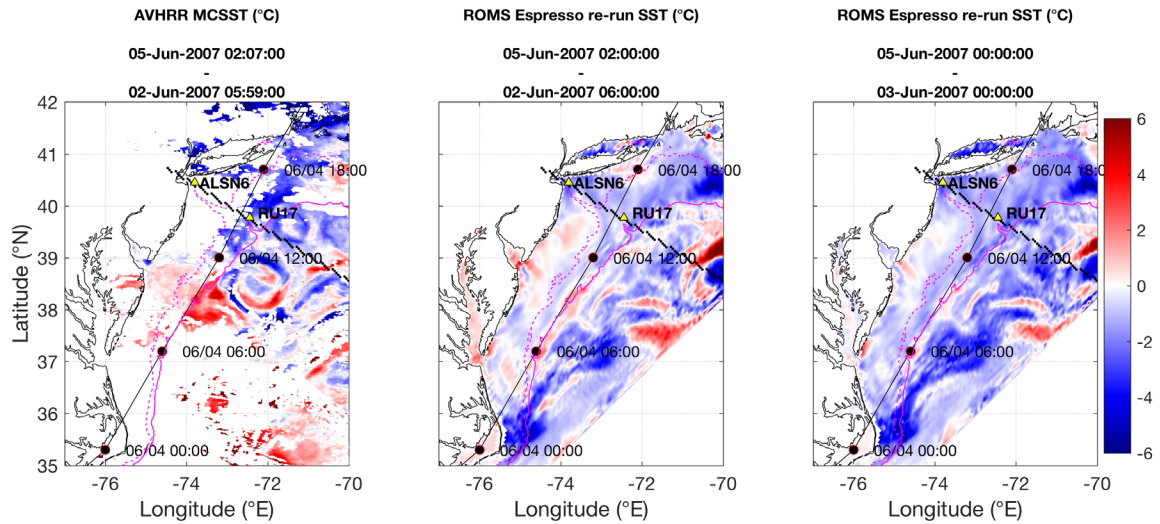**Figure 3.8** The same as Fig. 3.6, but for post-storm minus pre-storm, and adding a third panel (right) with post-storm minus pre-storm time difference chosen to maximize the cooling across the map.
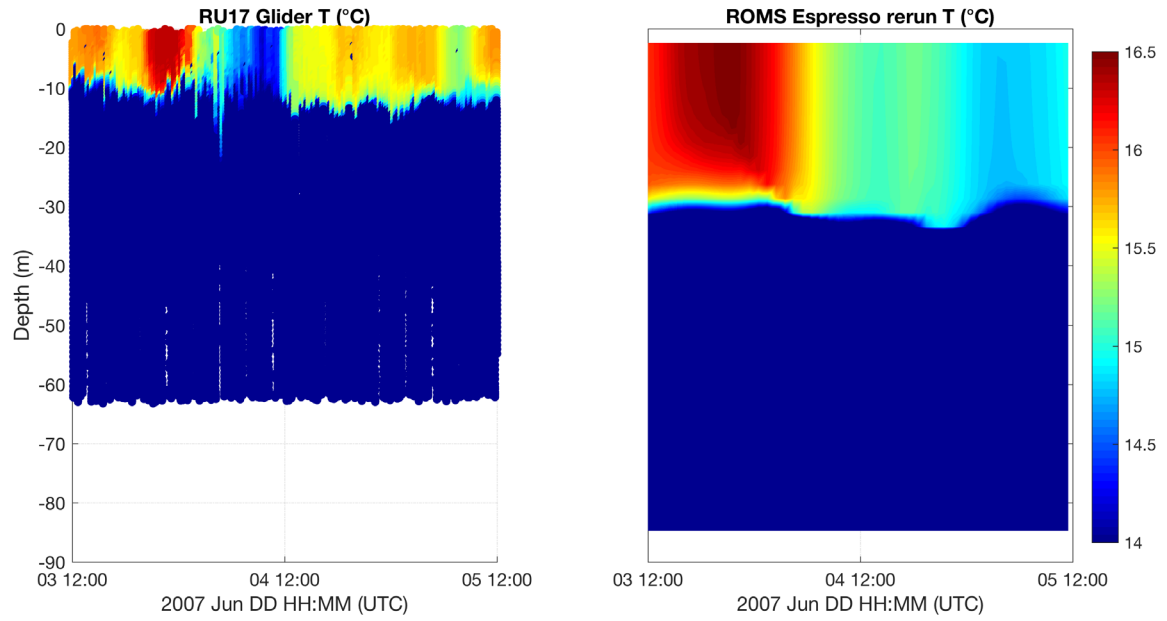
Figure 3.9 The same as Fig. 3.5, but for RU17 glider in Barry. RU17 only sampled to ~60m even though full water column depth was >80m.
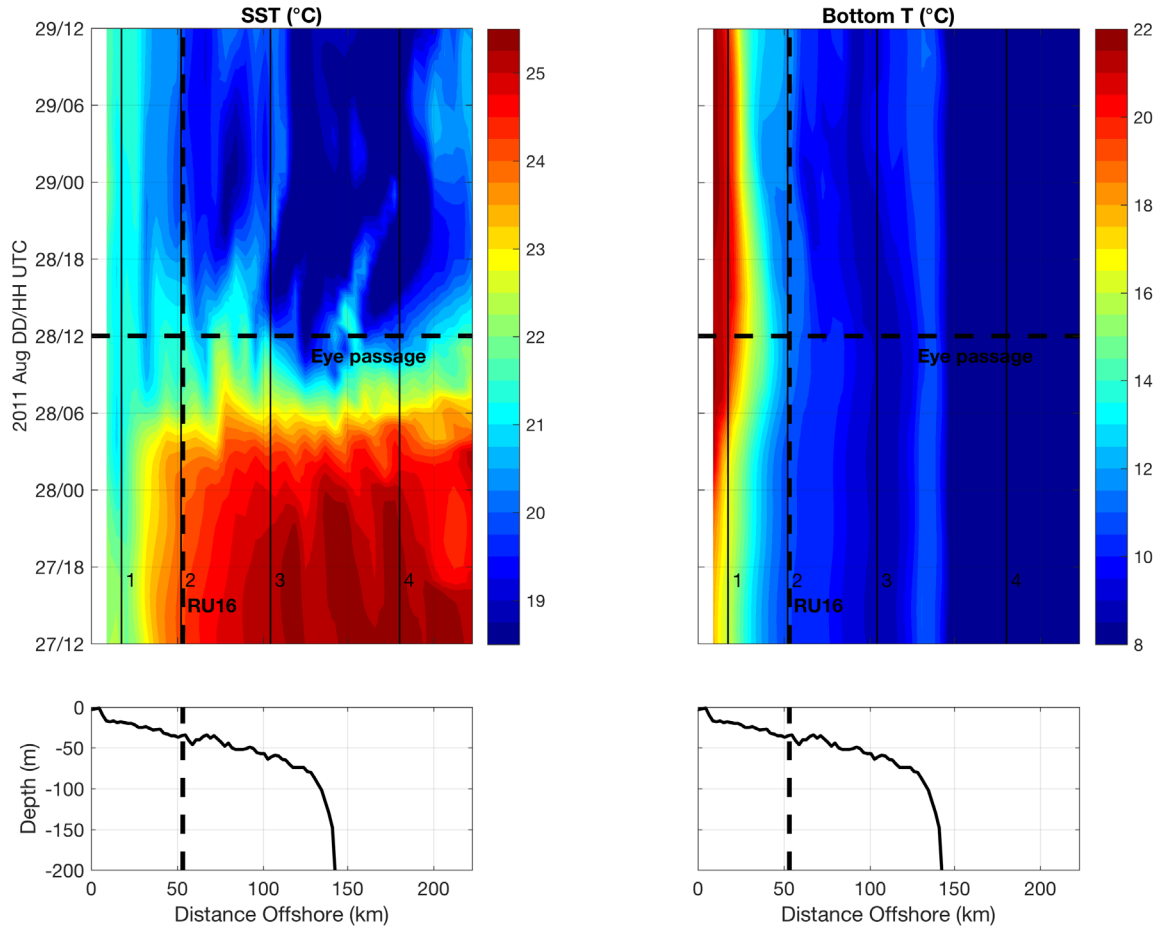
Figure 3.10 Hövmoller of SST (°C, left) and bottom temperature (°C, right) from the ROMS ESPreSSO re-run. Eye passage in NAM atmospheric forcing marked with the horizontal dashed line, and RU16 glider location marked with the vertical dashed line. Vertical solid lines 1 (upwelling), 2 (near RU16), 3 (in Cold Pool core), and 4 (in deep water) are locations where temperature diagnostics are performed in Fig. 3.24. Water depth (m) along the cross section is plotted in the bottom panels.
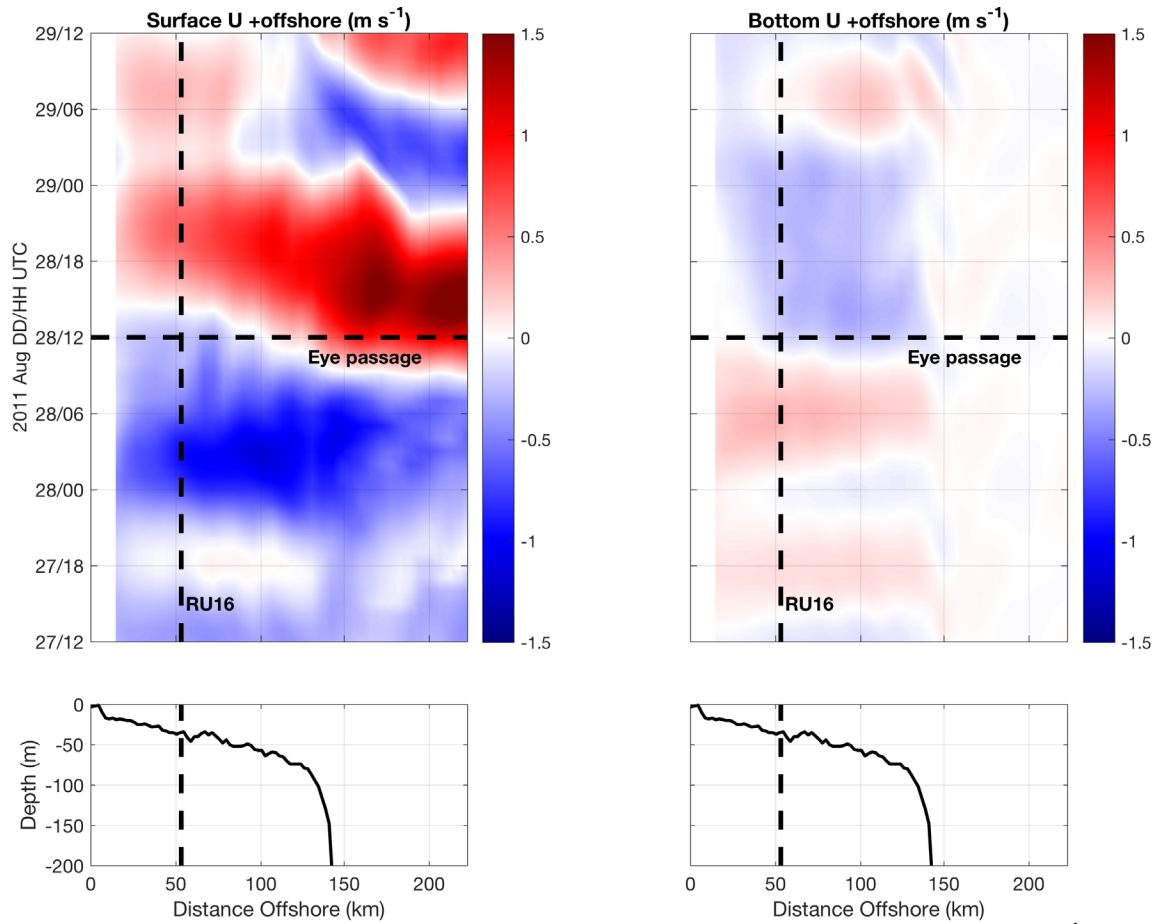
Figure 3.11 Same as Fig. 3.10 but for surface and bottom cross-shelf currents (m s^{-1}), positive reds offshore and negative blues onshore.
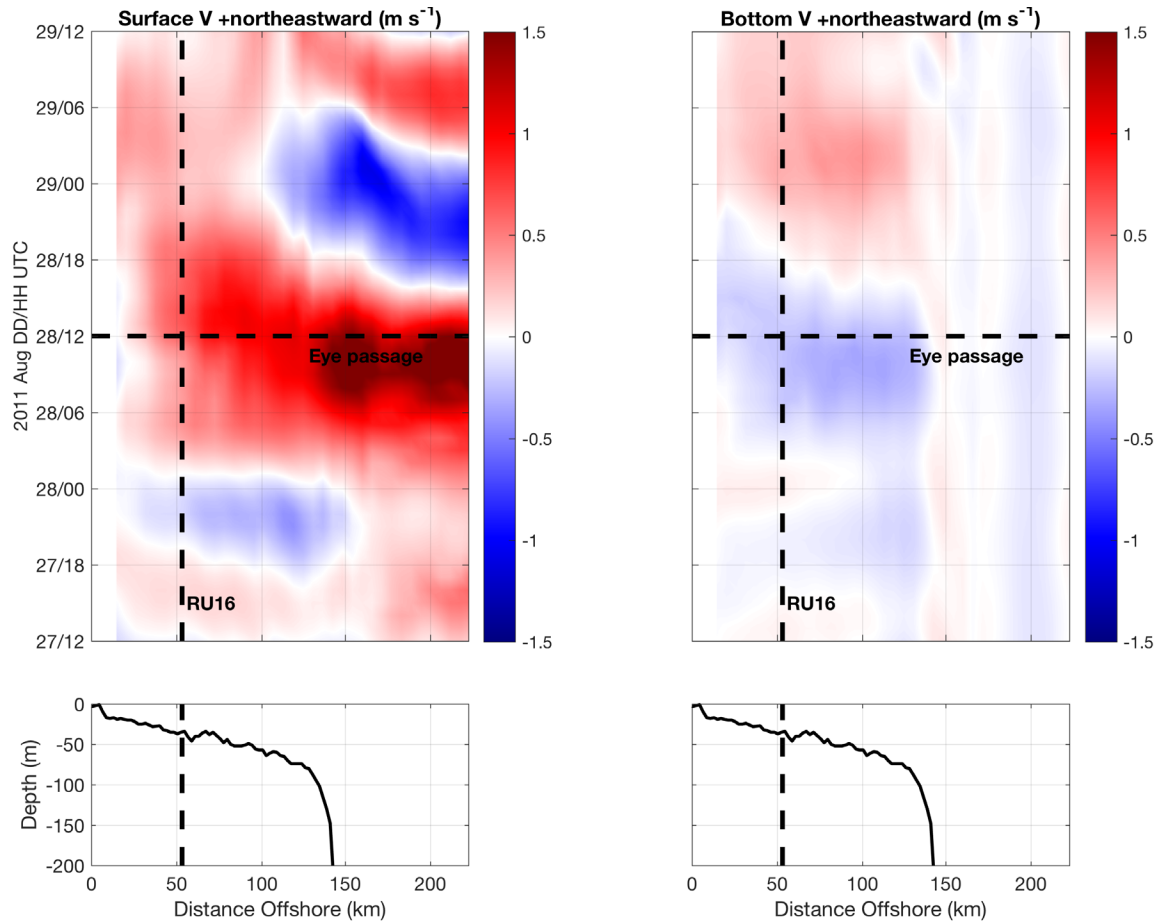
Figure 3.12 Same as Fig. 3.10 but for surface and bottom along-shelf currents (m s^{-1}), positive reds northeastward and negative blues southwestward.
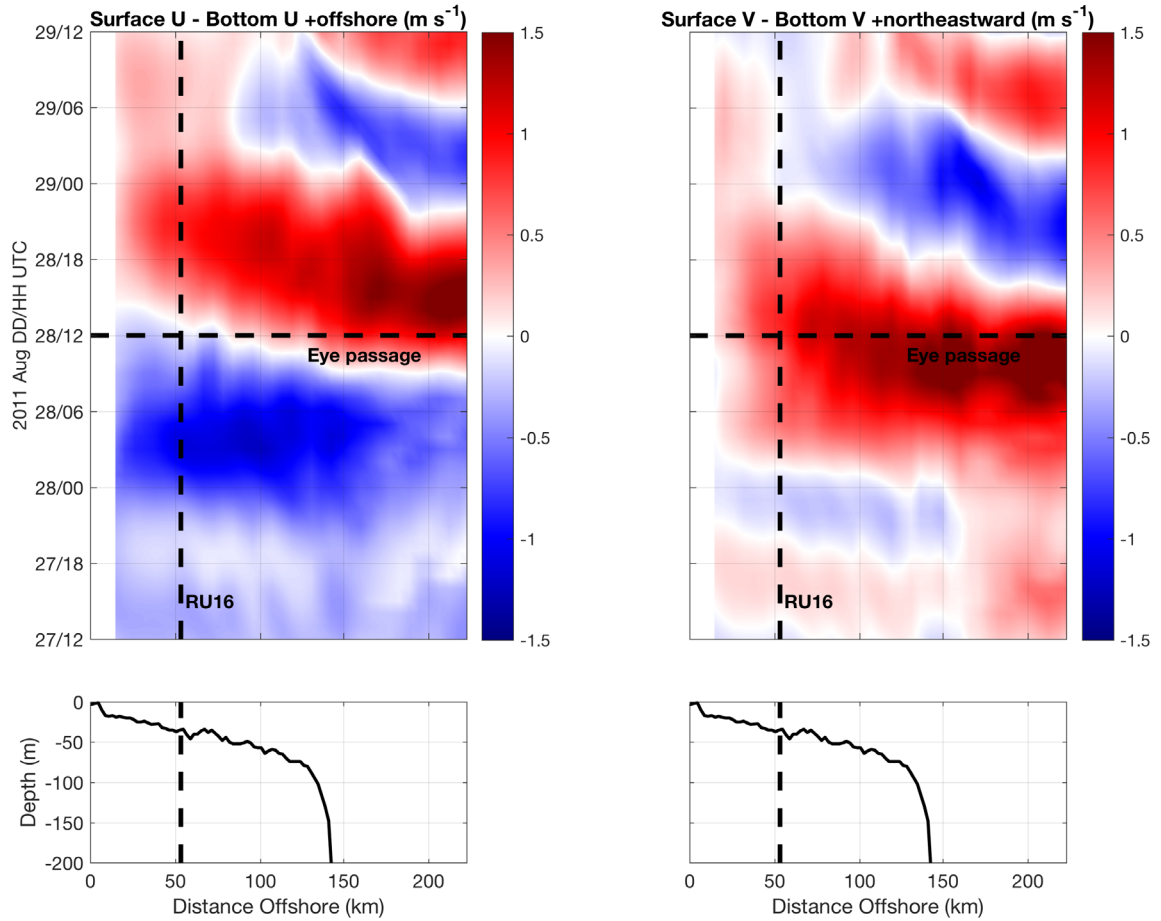
Figure 3.13 Same as Figs. 3.11 and 3.12 but for surface to bottom cross-shelf shear (left, positive reds offshore, negative blues onshore) and surface to bottom along-shelf shear (left, positive reds northeastward, negative blues southwestward) (m s^{-1}).
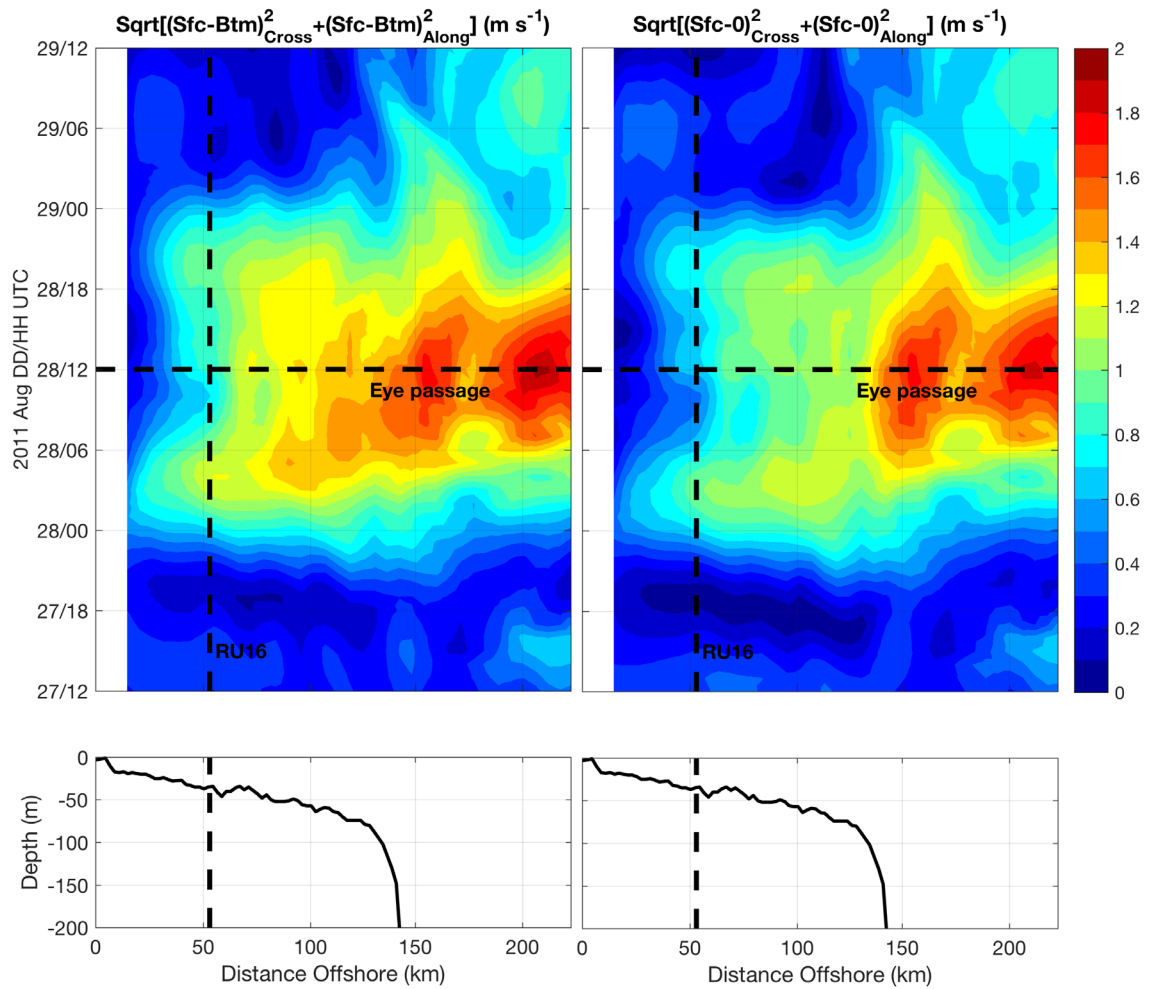
Figure 3.14 Same as Fig. 3.13 but for bulk surface to bottom cross- and along-shelf shear (left, m s^{-1}). This bulk shear is calculated according to the equation in the header: square root of the sum of the squares of the surface to bottom cross- and along-shelf shears. Right panel is the same as left but for 0 substituted for bottom currents.
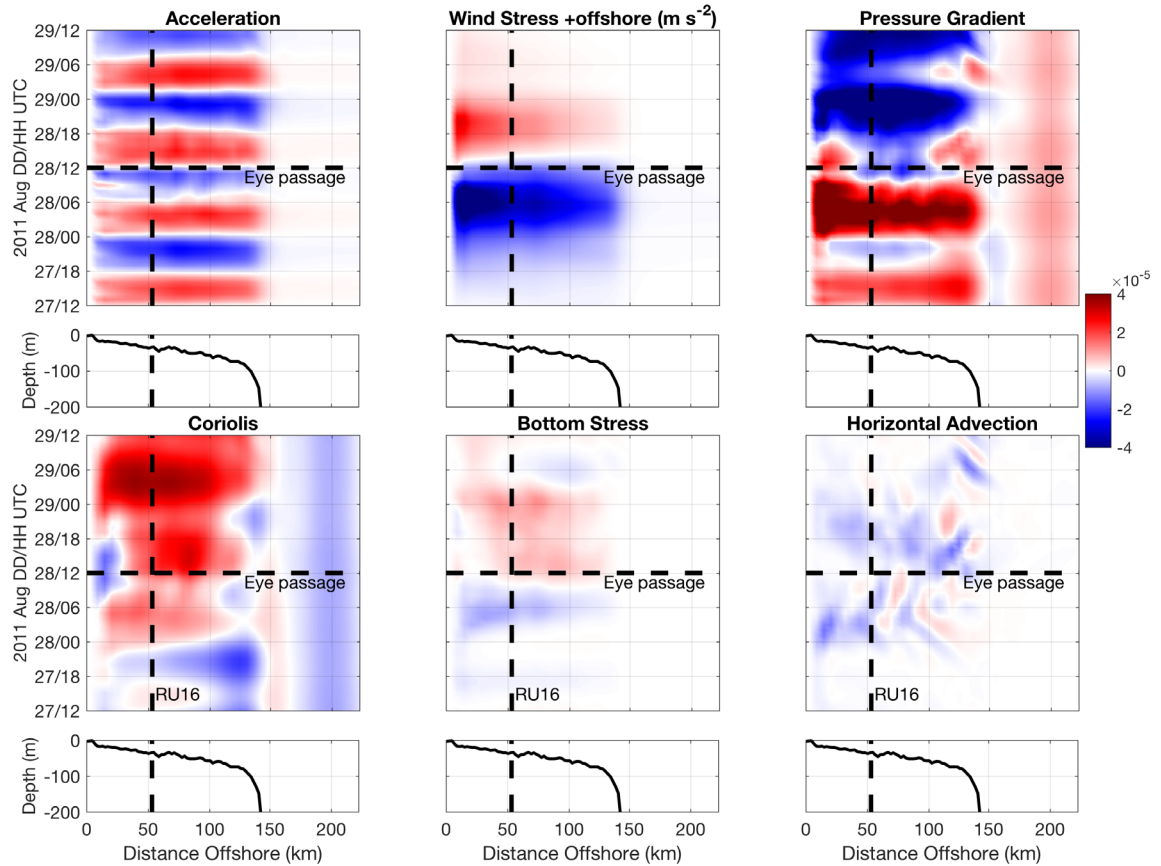
Figure 3.15 Hövmollers of the cross-shelf depth-averaged momentum balance terms (m s^{-2}), with positive reds offshore and negative blues onshore. Horizontal diffusion was small and thus not plotted.
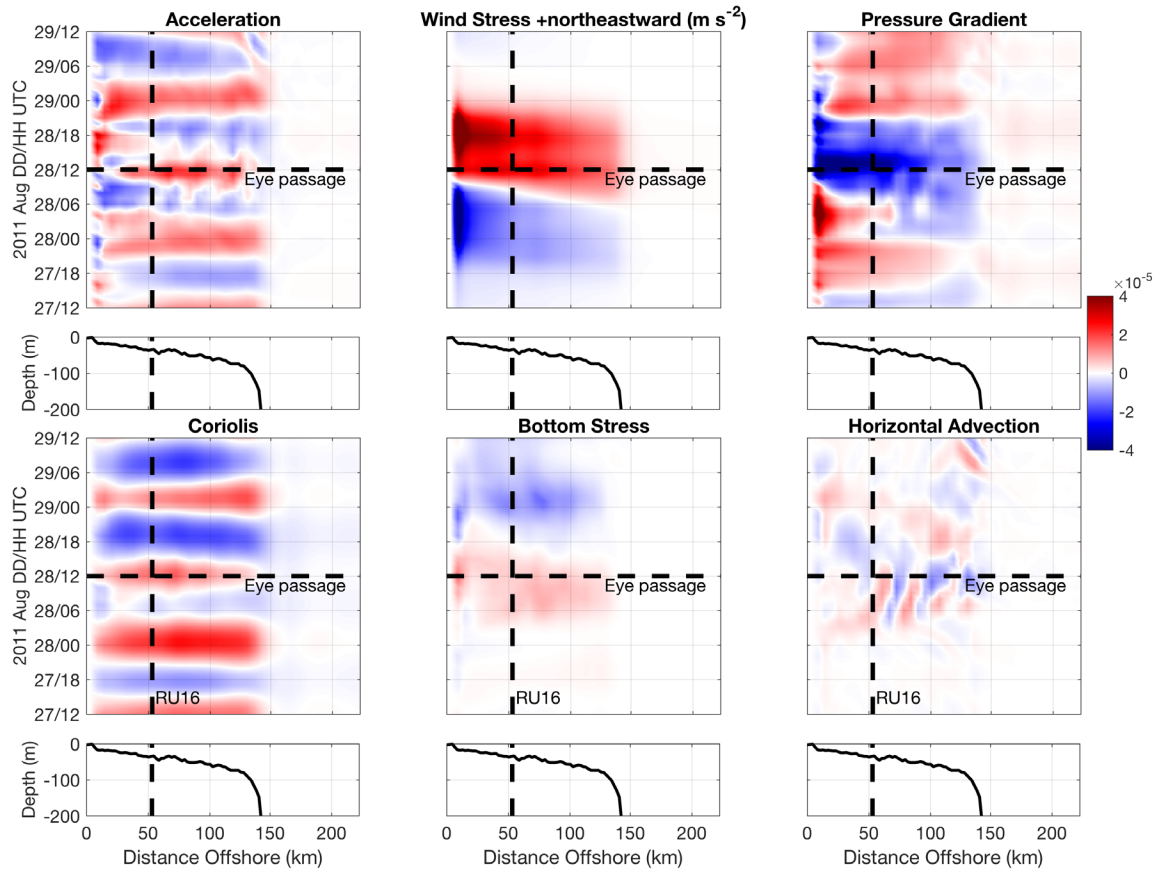
Figure 3.16 Same as Fig. 3.15 but for along-shelf depth-averaged momentum balance terms (m s^{-2}), with positive reds northeastward and negative blues southwestward.
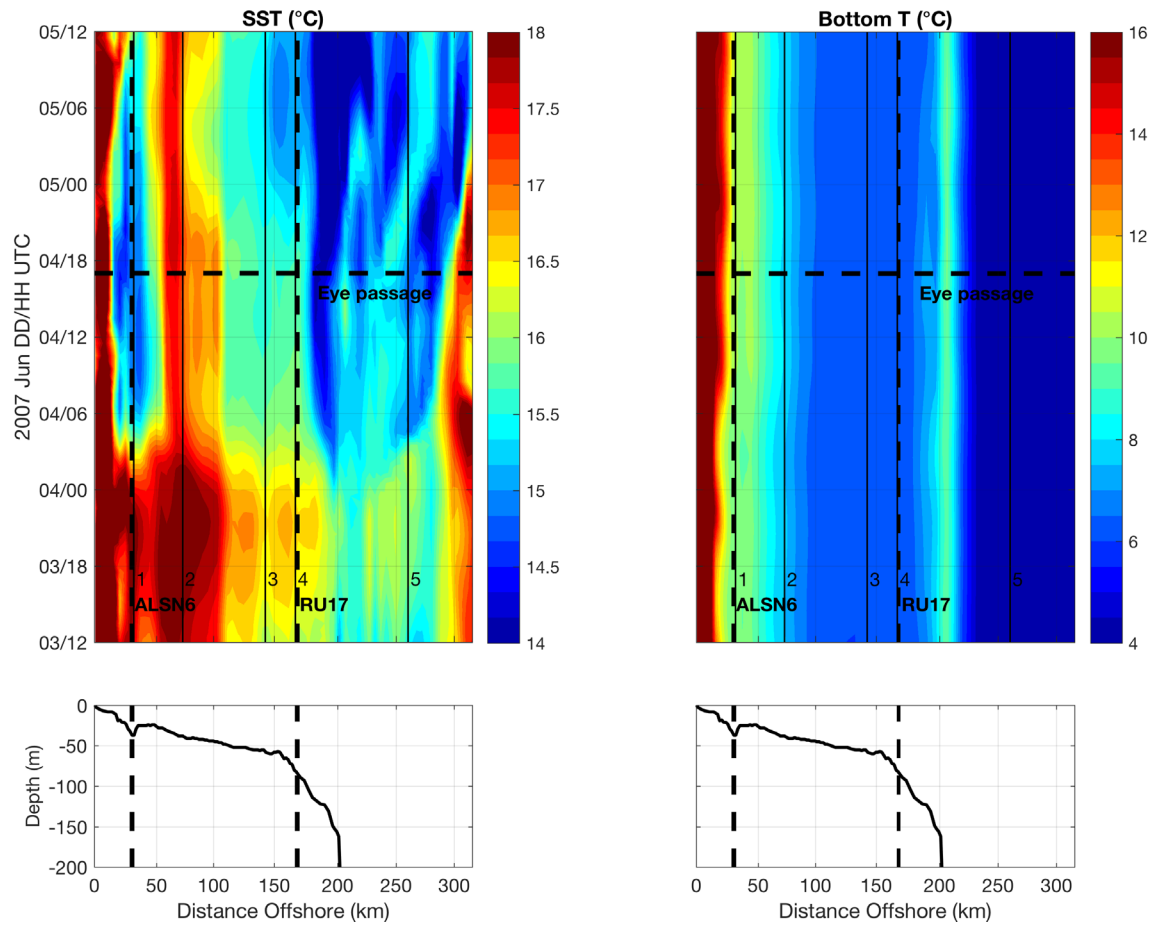
Figure 3.17 Same as Fig. 3.10 but for Barry, with ALSN6 and RU17 locations plotted as vertical dashed lines. Vertical solid lines 2 (near ALSN6), 2 (in warm strip), 3 (in Cold Pool core), 4 (near RU17), and 5 (in deep water) are locations where temperature diagnostics are performed in Fig. 3.25.
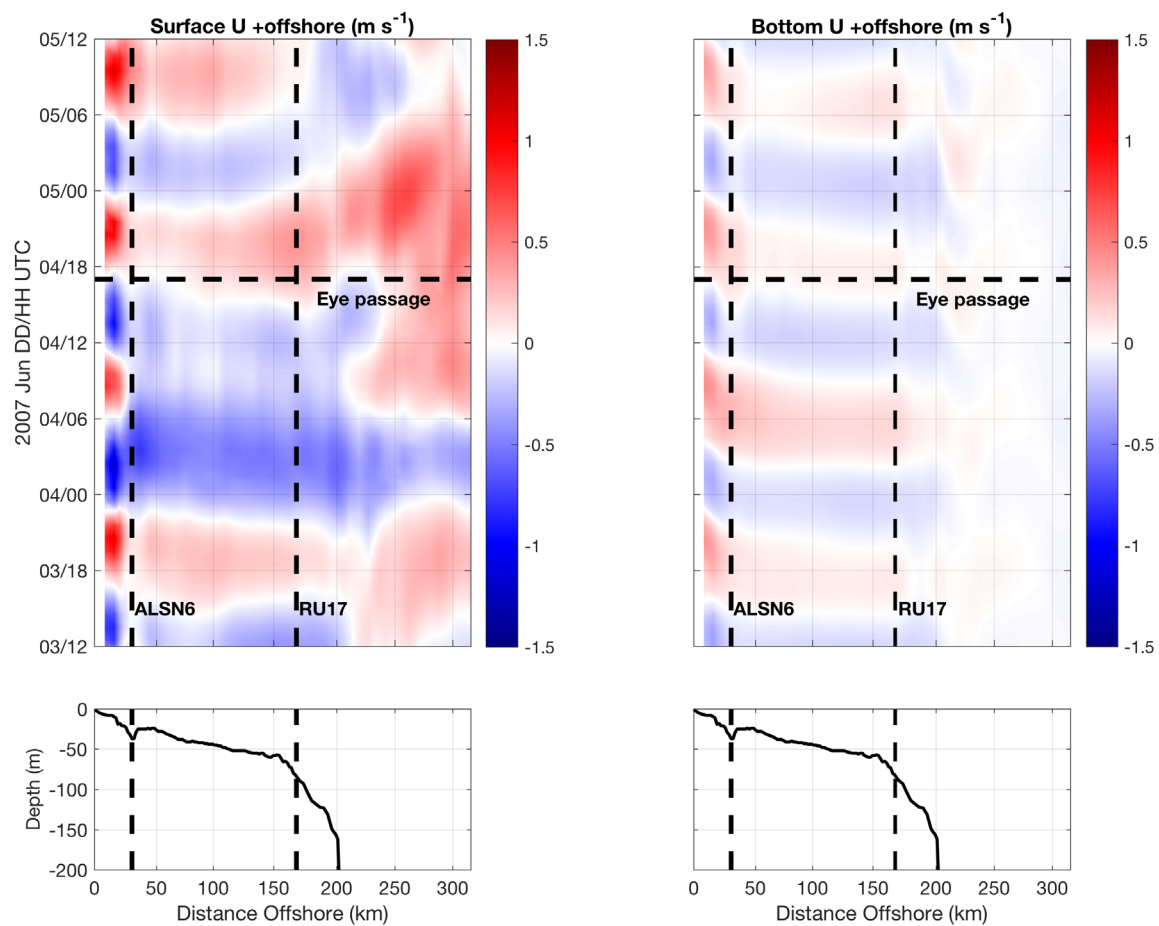
Figure 3.18 Same as Fig. 3.11 but for Barry.
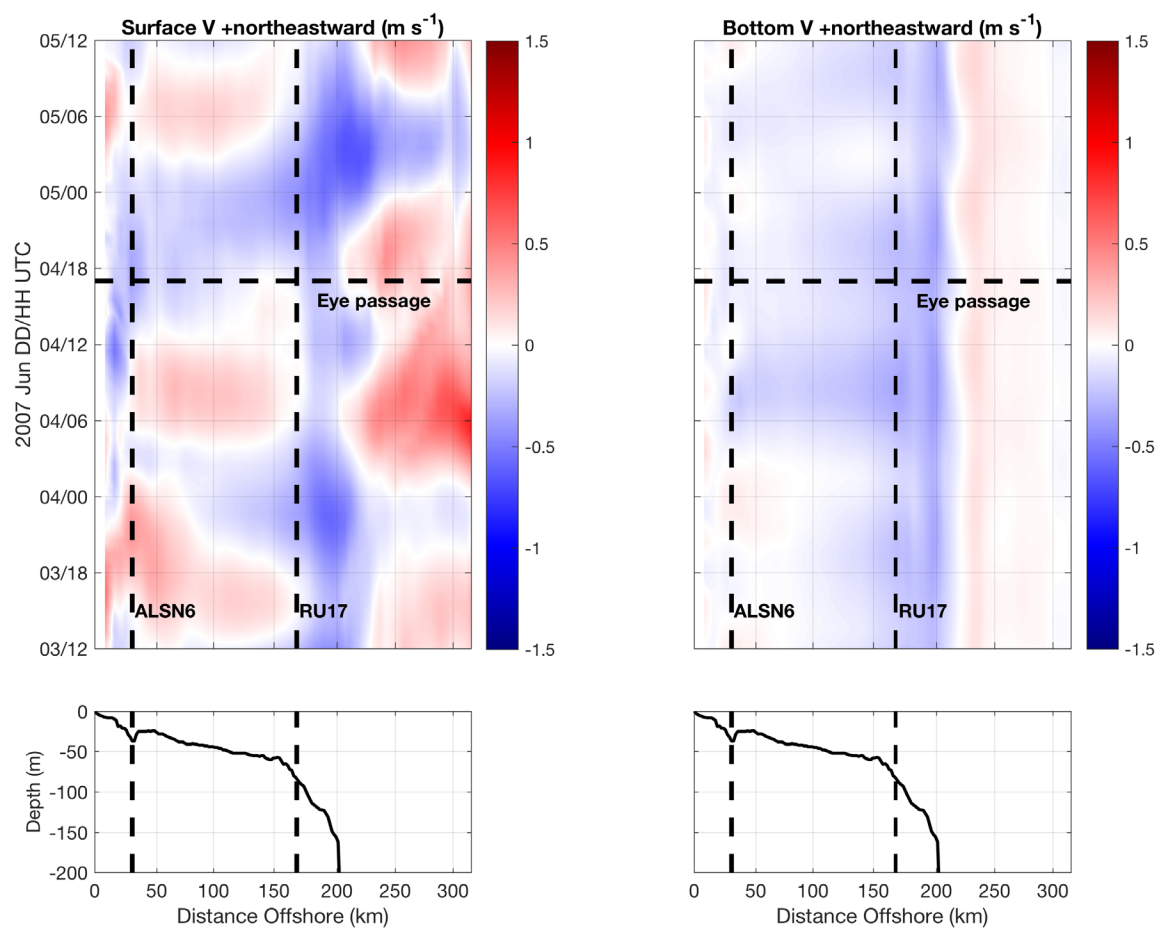
Figure 3.19 Same as Fig. 3.12 but for Barry.
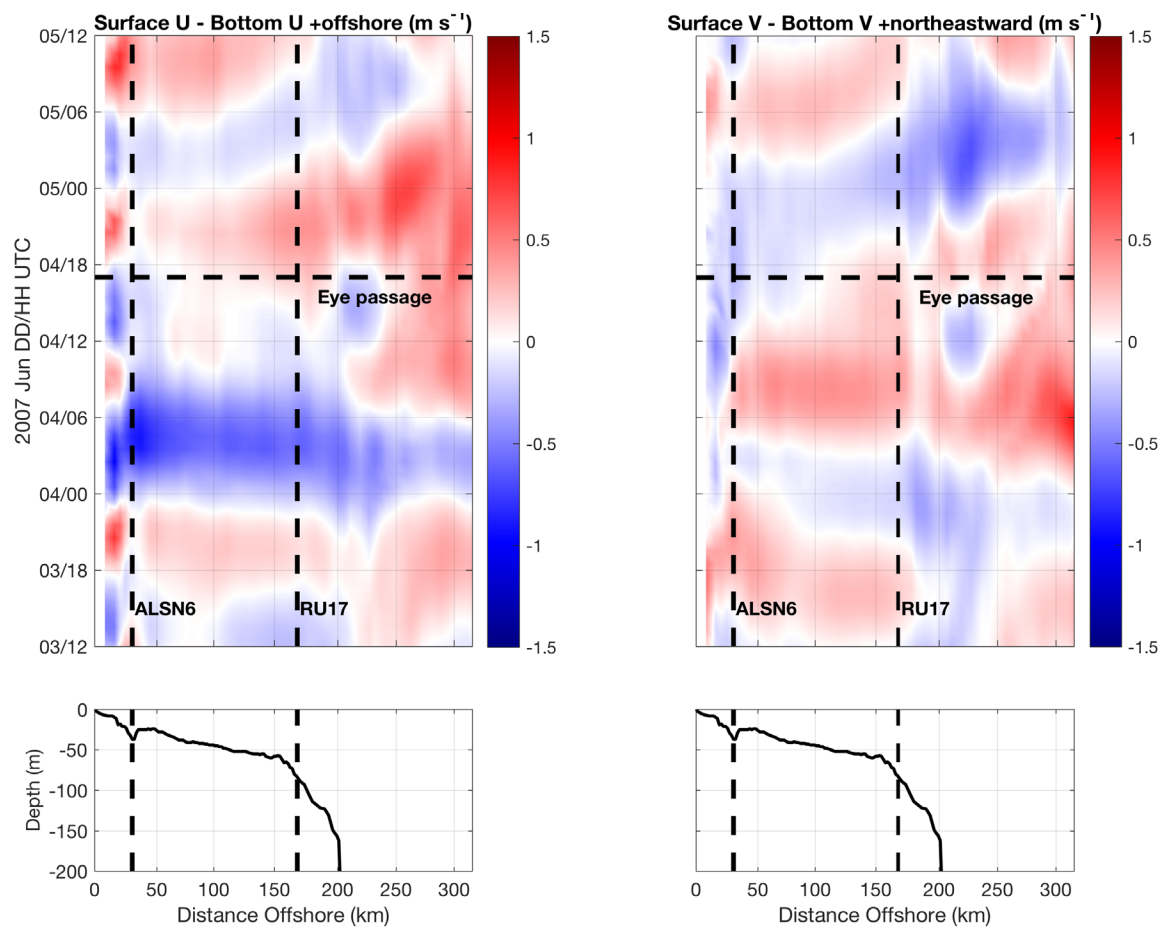
Figure 3.20 Same as Fig. 3.13 but for Barry.
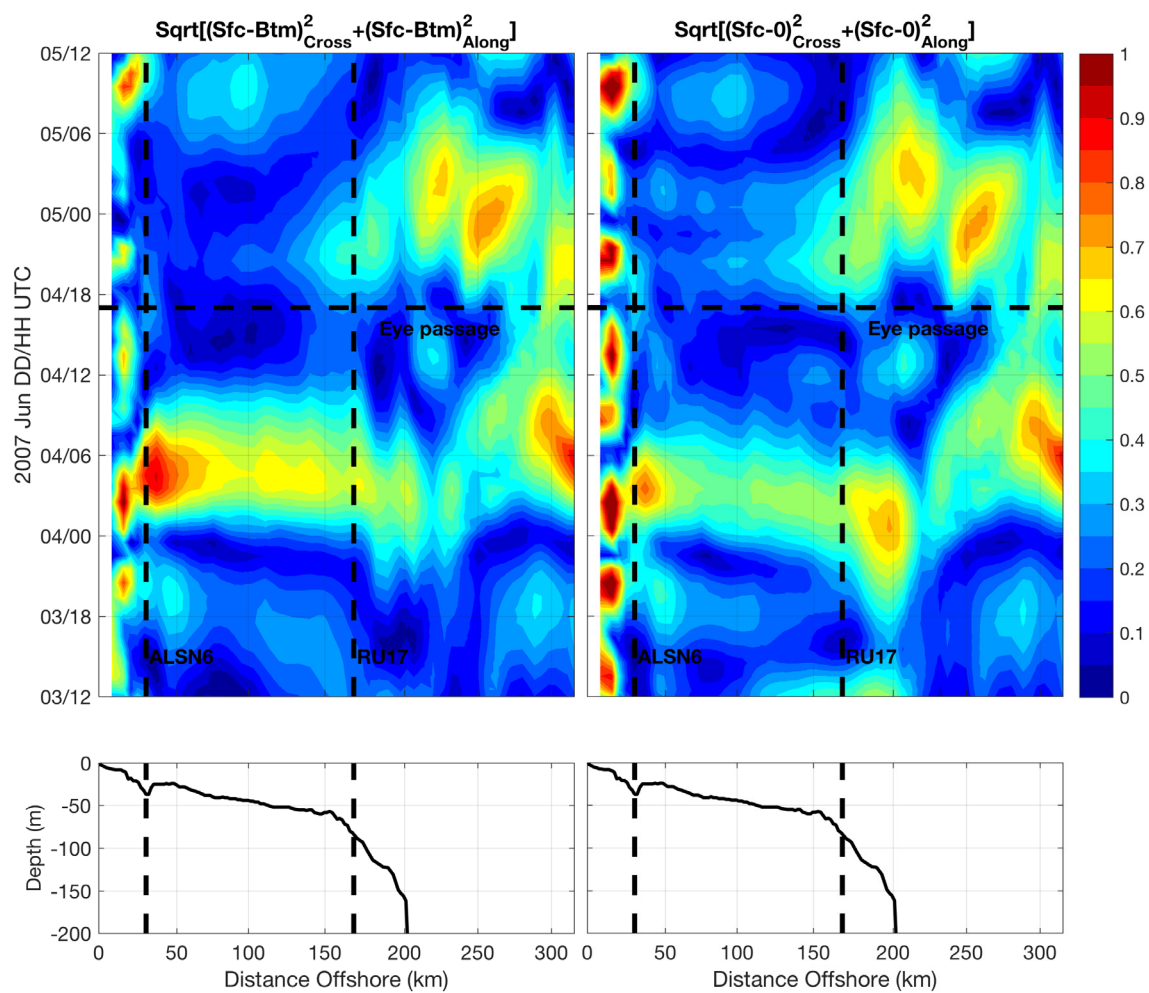
Figure 3.21 Same as Fig. 3.14 but for Barry.
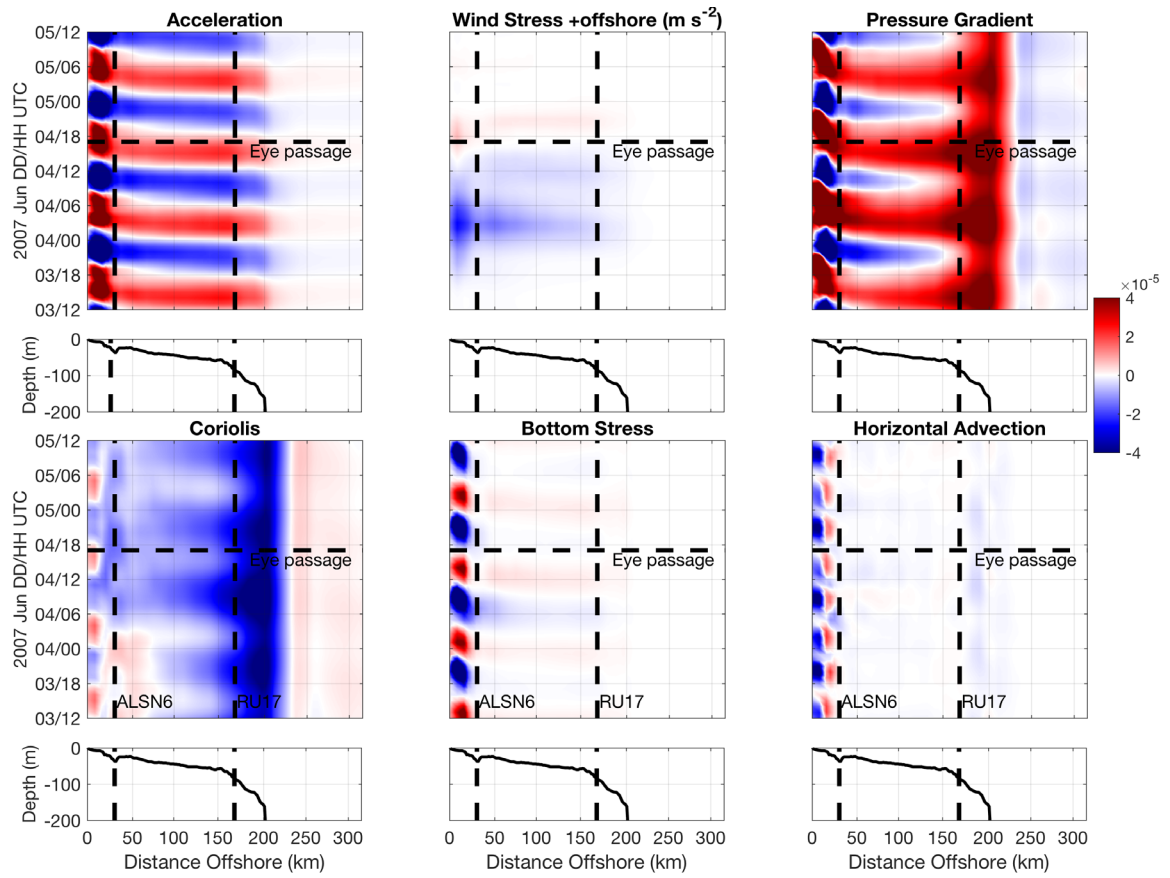
Figure 3.22 Same as Fig. 3.15 but for Barry.
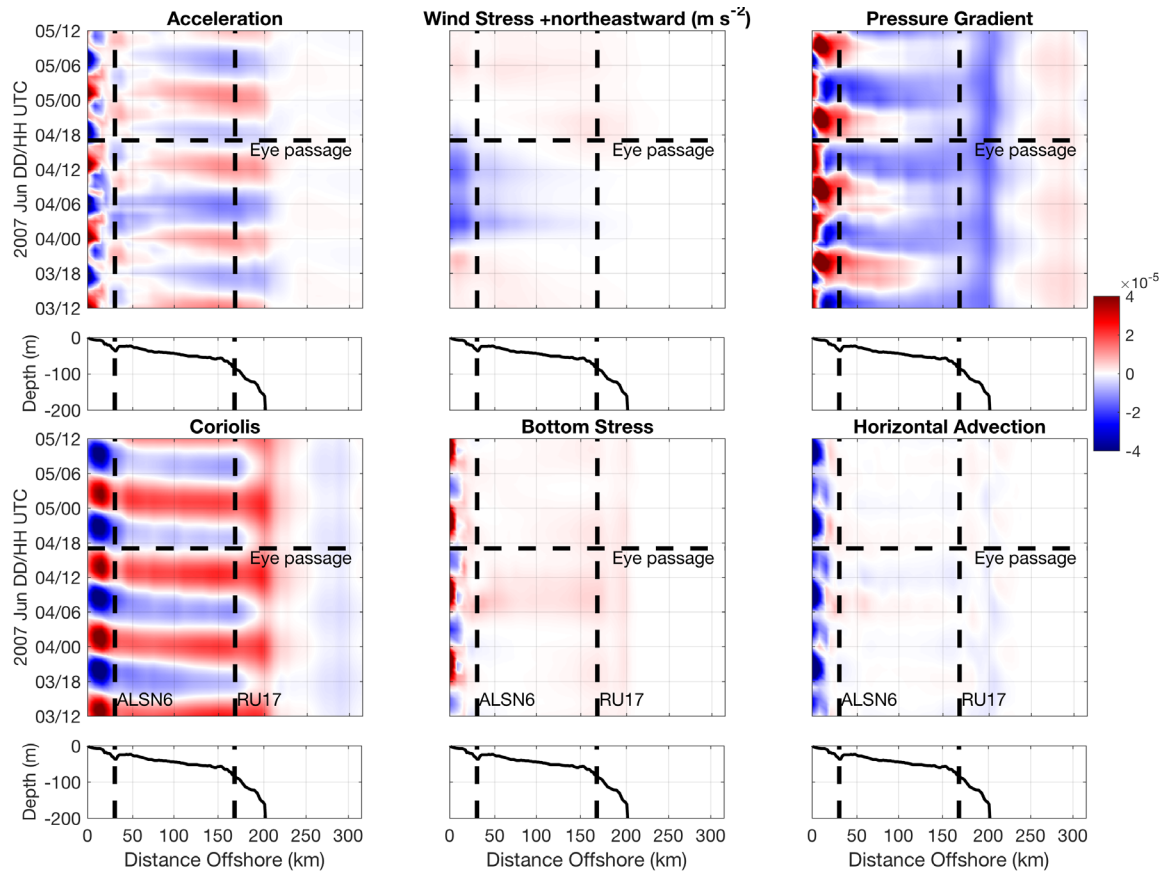
Figure 3.23 Same as Fig. 3.16 but for Barry.
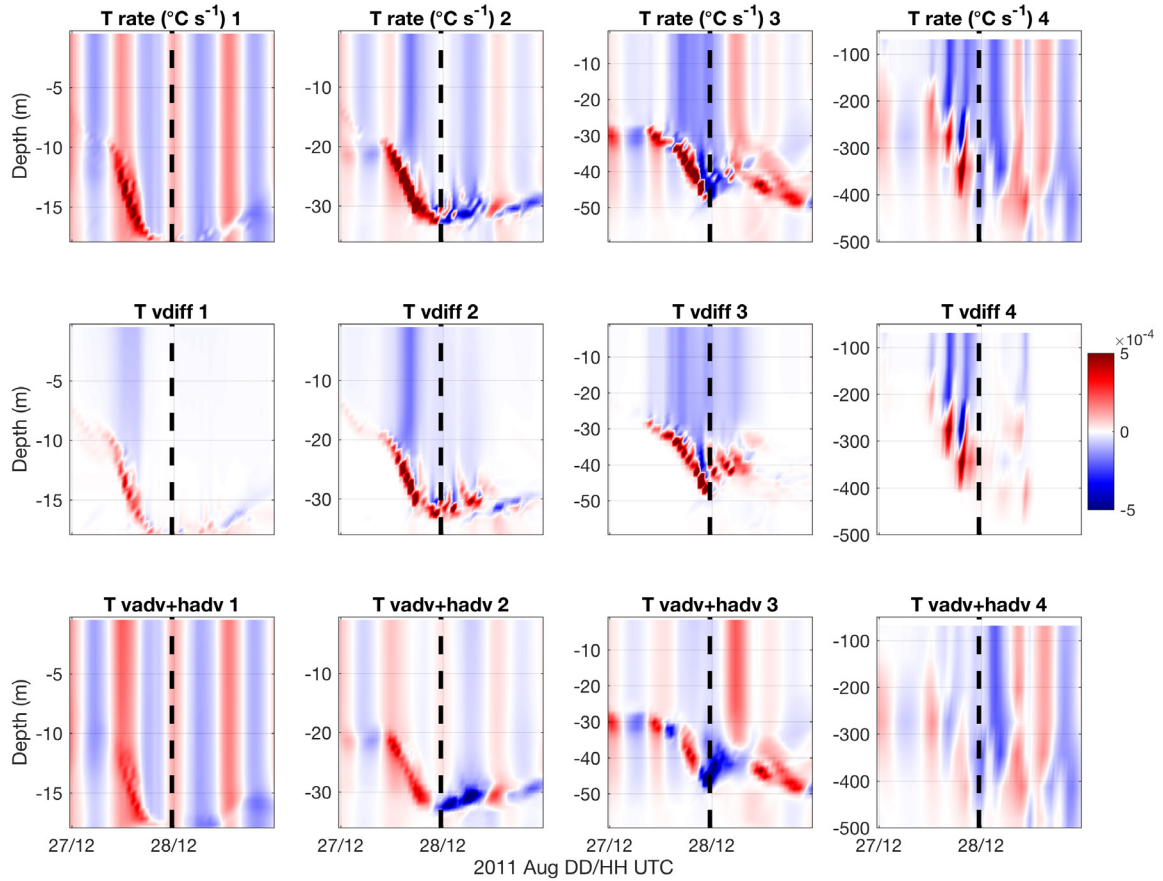
Figure 3.24 Temperature diagnostic equation terms at points 1-4 marked in Fig. 3.10, with full temperature rate term at top, vertical diffusion in middle, and vertical + horizontal advection at bottom (°C s⁻¹). Horizontal diffusion is small and thus not plotted. Eye passage marked with vertical dashed line. At point 4, only the top 500m of the water column is plotted.
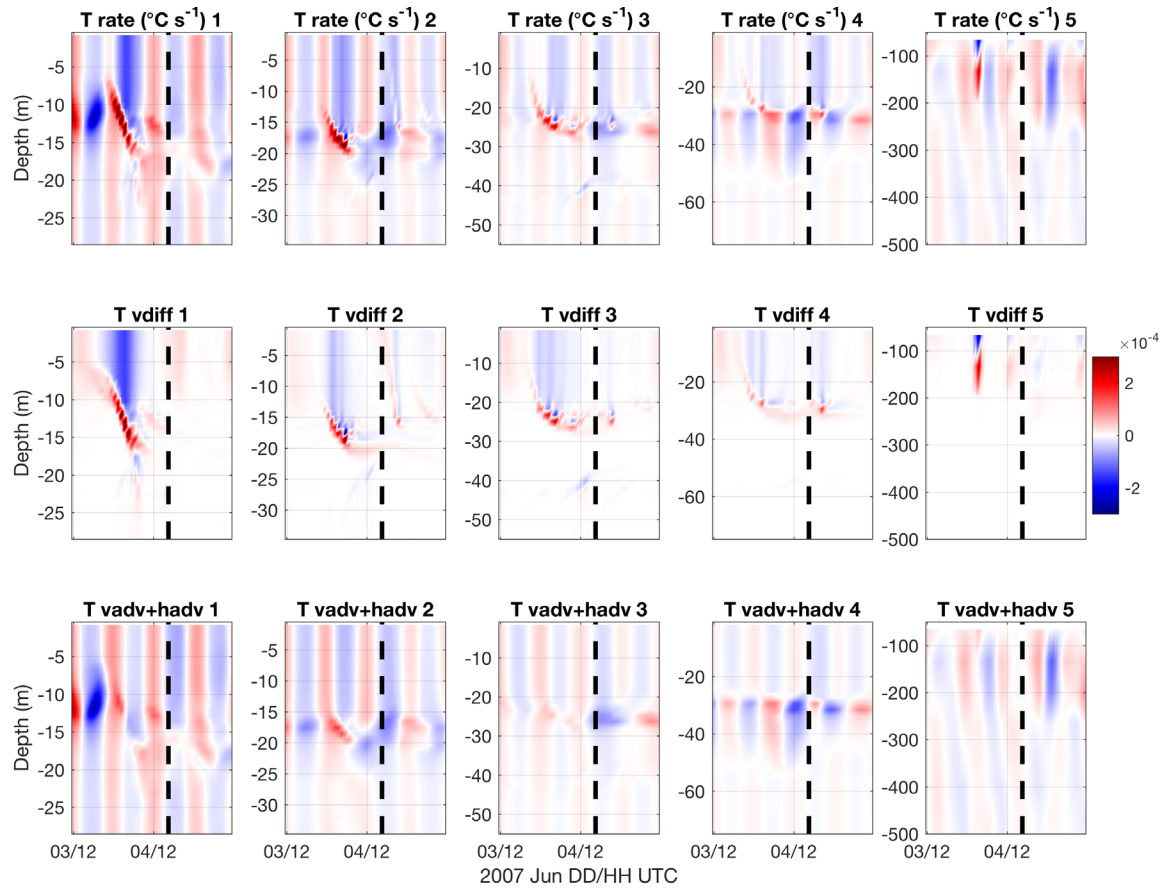
Figure 3.25 Same as Fig. 3.24 but for Barry. Points 1-5 are marked in Fig. 3.17.

Chapter 4

Offshore Sea Breeze Sensitivity to Coastal Upwelling and Synoptic Flow

4.1 Introduction

The sea breeze circulation, caused by the thermal contrast between the land and sea (Fig. 4.1), has been well-documented since at least ancient Greece [*Steele et al.*, 2013], especially over land. While observations are more prevalent on land than in water, historically there have also been many onshore implications of the sea breeze, ranging from coastal/inland air quality [*Pielke*, 1991; *Ratcliff et al.*, 1996] including low-level ozone [*Lalas et al.*, 1983], to forest fires [*Rothermel*, 1983], nuclear power plant concerns [*Venkatesan et al.*, 2002], beach recreation [*De Freitas*, 1990], and heat waves [*Papanastasiou et al.*, 2010]. The offshore component of the sea breeze, in contrast, has received less attention due to the relative paucity of observations, and offshore sea breeze studies thus have been mostly restricted to numerical simulations [e.g. *Steele et al.*, 2014 and references within].

In recent years, interest in offshore wind energy in the U.S. has increased, with the country's first offshore wind farm constructed offshore of Block Island, RI at the time of this writing. The offshore component of the sea breeze, thus, has gained significance for not only the sailing and fishing communities but now also for the offshore wind energy industry, and new methods to study the circulation offshore will be needed to fully understand its potential impact on the offshore wind energy resource. This chapter will explore one of these techniques—Lagrangian coherent structures (LCSs)—that have not yet been readily applied to study the sea breeze.

The sea breeze can be classified into four main types, dependent on synoptic wind conditions: a) *pure*, when the largest synoptic wind component is perpendicular to the coast and in the offshore direction, opposing the sea breeze flow, b) *corkscrew*, when the largest synoptic wind component is parallel to the coast with the land surface to the left, c) *backdoor*, when the largest synoptic wind component is parallel to the coast with the land surface to the right, and d) *synoptic*, when any wind—sea breeze or synoptic—is blowing onshore from sea to land and enhancing the near surface sea breeze winds [*Miller et al.*, 2003]. See [*Miller et al.*, 2003; *Steele et al.*, 2014] for graphical depictions of these main sea breeze types.

Unlike the onshore side where the inland frontal boundary is clearly marked and visible on weather radar by a distinct sea breeze front, the offshore side and its spatial scales are much more difficult to distinguish and define objectively [*Finkele*, 1998]. One definition that has been used is the cutoff of 1.0 m s^{-1} onshore wind speed within the lowest 100m of the sea breeze circulation [*Arritt*, 1989], although this can only be applied in offshore synoptic wind conditions—for *pure* sea breezes [*Finkele*, 1998]. Alternatively, the offshore extent can be defined as the point where the wind speed is uninfluenced by the sea breeze, greatly increasing the offshore boundary distance. In the "convectional" theory of the sea breeze [*Rotunno*, 1983], the extensive calm region that frequently occurs nearby this point—highly dependent on synoptic wind direction—does not necessarily represent the region of largest divergence, in contrast to the onshore front that often represents the region of largest convergence.

Lagrangian coherent structures (LCSs) are boundaries in a fluid, such as the atmosphere or ocean, that distinguish regions of differing dynamics within the

Lagrangian point of view which is frame independent [*Haller*, 2015]. Passive tracers within a coherent structure will stay within the structure for as long as it lives. LCSs are often associated with mesoscale features, such as eddies, fronts, and jets, with attracting LCSs marking regions where particles aggregate and repelling LCSs marking regions from which particles disperse. Therefore, computation of LCSs can identify regions of convergence and divergence within a fluid flow, which in our case is the sea breeze circulation. Again, in the "convectional" theory of the sea breeze, one would expect onshore convergence, rising air, and an attracting LCS marking the inland extent, and offshore divergence, sinking air, and a repelling LCS marking the offshore extent (Fig. 4.1). In this framework, the previously ill-defined offshore extent can be clarified in any synoptic flow conditions, and objective sensitivities of the offshore extent and intensity to forcings like synoptic flow strength and land-sea thermal contrast—i.e. coastal upwelling presence vs. absence, described below—can be performed.

4.1.1 Further Motivation

A *pure* sea breeze occurred across New Jersey on April 27, 2013, with light synoptic wind conditions from the northwest. The spring thermal contrast between the cold waters over the Mid-Atlantic Bight (MAB) continental shelf and the warming land surfaces produced an air temperature difference of nearly 8°C when comparing National Data Buoy Center (NDBC) 44009 air temperature to Atlantic City International Airport (KACY) 2m air temperature (Fig. 4.2B). A simulation using the Weather Research and Forecasting (WRF) model showed a skin temperature difference at 1700 UTC of at least double this air temperature difference (Fig. 4.2A). During this spring season, the ocean over the MAB continental shelf is well-mixed and cold from the previous winter

[*Bigelow*, 1933]. During the summer, the MAB becomes a two-layer stratified ocean [e.g. *Castelao et al.*, 2008] with warm surface waters approaching 26°C and cold bottom water—the MAB Cold Pool—remaining 10°C and lower from the previous winter north of the Hudson Canyon, and replenished by southwestward advection of northern cold water to south of the Hudson Canyon [*Houghton et al.*, 1982]. Although the surface waters are warming from the winter and spring, the land surfaces are warming at a greater rate, thus leading to sufficient thermal contrasts for frequent afternoon sea breezes over the coastal U.S. Mid-Atlantic.

Another phenomenon that occurs in this region during the summer is coastal upwelling, caused by the persistent southwesterly winds as they flow around the persistent summertime Bermuda High, the associated offshore Ekman transport, and the upwelling of cold water near the coast to replace the warmer water transported offshore [e.g. *Glenn et al.*, 2004]. The mean 2012-2014 upwelling sea surface temperature (SST) signal, attained by averaging across the 12 events with one representative Advanced Very High Resolution Radiometer (AVHRR) image per event, shows a recurrent node of upwelling south of Long Island, three recurrent nodes along the New Jersey (NJ) coast, and one node offshore of northern Delmarva (Fig. 4.3A). The recurrent nodes along NJ have been noted to occur downstream of a series of topographic highs associated with ancient river deltas [*Glenn et al.*, 1996, 2004]. The maximum extent of coastal upwelling during the 2012-2014 time period is also shown (Fig. 4.3B), with filaments of upwelling extending through the NJ Wind Energy Area (NJ WEA) and out to almost the shelf break at ~200m.

A *pure* sea breeze case occurred across NJ on August 13, 2012, with synoptic flow conditions again from the northwest. The summer thermal contrast was now between the hot land surface and the comparatively cooler ocean water. Coastal upwelling was also occurring on this day (Fig. 4.4B), but not two days prior (Fig. 4.4A). Air temperature differences between land and water approached 4°C during both the non-upwelling day and upwelling day (Fig. 4.4C), while skin surface temperature differences between land and water approached 10°C during the non-upwelling afternoon (Fig. 4.4A) and 12°C during the upwelling day afternoon (Fig. 4.4B).

Archived mean 2012-2014 daily max load data from the Mid-Atlantic Region of the Pennsylvania-New Jersey-Maryland (PJM) interconnection, paired with monthly frequency of NJ sea breeze and coastal upwelling days, show that the seasonal peak in sea breeze and coastal upwelling are both coincident with the seasonal peak in electricity demand in the region (Fig. 4.5). The spring peak as well as the summer peak in sea breeze days is also apparent, as is the summer to early fall peak in upwelling days. Therefore, a more complete understanding of the impact of coastal upwelling on the offshore component of the NJ sea breeze circulation is critical for a comprehensive offshore wind resource assessment during peak energy demand periods.

As stated above, synoptic flow determines the type of sea breeze that occurs, and is a significant modulator to the evolution of both the inshore and offshore components and expansion of the sea breeze cell. In spring 2002-2007 over the NJ shelf, dominant wind direction was from the SSW (~32% of the time), with secondary peaks in wind direction from the NW (21%) and NE (21%). In summer 2002-2007, dominant wind direction was again from the SSW (48%), with secondary peaks from the NE (15%) and

NW (11%) [*Gong et al.*, 2010]. This synoptic wind climatology reveals that during the spring and summer in the six-year period, dominant sea breeze type would have been *corkscrew* or *pure*.

It has been previously found in Australia that the offshore extent of the sea breeze is less sensitive to offshore synoptic wind (*pure* sea breeze) than its inland extent [*Finkele*, 1998]. By also testing the sensitivity of the NJ sea breeze circulation to synoptic flow strength in this chapter, the impact of coastal upwelling on the sea breeze will be placed in context.

This chapter will integrate:

    (a) validated numerical modeling techniques (WRF)

    (b) high-resolution satellite SST composites designed to capture and not remove coastal upwelling,

    (c) weather radar observations of the inland sea breeze front, and

    (d) the LCS method to objectively define the offshore extent and intensity of the NJ sea breeze,

in order to investigate the sensitivity of the offshore and onshore NJ sea breeze circulation components to synoptic flow and coastal upwelling. In section 4.2, materials, data, and methods will be described; in section 4.3, results from the analyses will be shown; and in section 4.4, conclusions, comparisons to relevant past studies, and future work will be discussed.

4.2 Data and Methods

4.2.1 Buoys

National Data Buoy Center (NDBC) buoys 44009 and 44065 were used in this chapter (Fig. 4.2 and 4.4). Water temperature was used, which is measured at 0.6 m depth at both buoys, and air temperature was also used, which is measured at 4m. These data provide near-surface water and over-water air temperatures for the spring non-upwelling and summer upwelling cases.

4.2.2 KACY

Atlantic City International Airport (KACY) 2m hourly air temperature data were used for Figs. 4.2 and 4.4.

4.2.3 Bathymetry

U.S. Coastal Relief Model data from the NOAA National Centers for Environmental Information were used for water depth and coastlines throughout this chapter [*NOAA National Centers for Environmental Prediction*, 2016].

4.2.4 Satellite SST

The empirically-derived declouding techniques specific for the MAB and described in Glenn et al. (2016) were used to remove bright cloud covered pixels from AVHRR data while retaining the darker ocean pixels. These declouded AVHRR passes were used in Fig. 4.3. The same three-day 'coldest dark pixel' SST compositing technique described in Glenn et al. (2016) and used in Chapter 2 was used to map and preserve cold coastal upwelling regions. These SST composites were used in Figs. 4.2 and 4.4, and as bottom boundary conditions over water for WRF simulations (described below).

4.2.5 Weather Radar

Next-Generation Radar (NEXRAD) clear-air mode Level-II data from KDIX (New Jersey) and KDOX (Delaware) were used for inland sea breeze front identification. Dust and insects can be collected within the inland sea breeze frontal convergence zone, producing high reflectivities in the weather radar return [*Atlas*, 1960]. Base elevation scans were used in Figs. 4.6 and 4.8, for observational verification of the LCS identification of the inland sea breeze front.

4.2.6 WRF

The same WRF-ARW dynamical core used in Chapter 2 was used in this chapter, but Version 3.6.1 here. The 3km resolution WRF-ARW domain is depicted in Fig 4.2. North American Mesoscale model (NAM) 12km data were used for initial conditions and lateral boundary conditions. The coldest dark pixel SST composites described above in section 4.2.3 were used for bottom boundary conditions over the ocean. The following physics options are used: longwave radiation physics were computed by the Rapid Radiative Transfer Model; shortwave radiation physics were computed by the Dudhia scheme; the MM5 Monin-Obukhov atmospheric layer model and the Noah Land Surface Model were used with the Yonsei University (YSU) planetary boundary layer (PBL) scheme (consistent with [*Steele et al.*, 2014]); and the WRF Single-Moment 3-class moisture microphysics scheme [*Hong et al.*, 2004] was used for grid-scale precipitation processes.

Because offshore sea breeze extent has been found to be sensitive to PBL scheme [*Steele et al.*, 2014], sensitivity to PBL scheme was tested on the spring sea breeze case, comparing YSU to Mellor–Yamada–Nakanishi–Niino PBL scheme [MYNN, *Nakanishi and Niino*, 2004, 2006]. MYNN has been found to be the best PBL scheme for the

offshore environment [*Munoz-Esparza and Canadillas*, 2012], while YSU has been used in a previous offshore sea breeze climatology study for the UK [*Steele et al.*, 2014]. Results of this comparison show that both inland and offshore extent are not sensitive to choice of PBL scheme.

A similar WRF configuration (Rutgers University-WRF, or RU-WRF) used for NJ offshore wind energy applications was validated against coastal and offshore monitoring systems using criteria accepted by the wind energy industry and the National Renewable Energy Laboratory's (NREL's) National Wind Technology Center (NWTC) for determining model performance [*Dvorak et al.*, 2013]. Results show that the model is validated and can be used to analyze and predict NJ's coastal/offshore wind resource [*Dunk and Glenn*, 2013].

WRF output was set for every 10-minutes and simulations were initialized at 00Z on the day of the sea breeze.

4.2.7 LCS

LCS techniques [*Gildor et al.*, 2009] were used to clarify the onshore and offshore boundaries of the sea breeze circulation. Conventional divergence fields of the WRF winds would produce a low signal-to-noise ratio, but by using the Lagrangian framework we are able to increase the signal-to-noise ratio to produce a more effective sea breeze boundary clarification, especially in the traditionally difficult-to-define offshore zone.

First, particles were placed on a 10km resolution grid within the 3km WRF wind fields. Then, the particles were forced to move by the horizontal winds every 10 minutes over one hour—i.e. forward trajectories—at various levels throughout the marine

atmospheric boundary layer. These 1-hour short trajectory "simulations" were performed for 17-18, 18-19, 19-20, 20-21, 21-22, 22-23, and 23-00 UTC, as determined by peak sea breeze time for both the spring and summer sea breeze cases. Further, only 2D trajectories were performed, and not full 3D trajectories, as vertical velocities were $O(100)$ times smaller than horizontal velocities during the sea breeze cases analyzed.

Numerous ways exist to identify LCSs from the trajectories, including finite time Lyapunov exponent (FTLE), finite size Lyapunov exponent (FSLE), and relative dispersion (RD) [*Haller*, 2015]. Here, we have chosen to use RD, defined as the mean separation distance between two particles after the 1-hour simulation. For example, two particles start 10km apart, and move 2km farther away from each other, thus resulting in an RD value of 12km.

Let us define $R(t) = \|r^{(1)} - r^{(2)}\|$ as the distance between two trajectories at time t. RD is defined as the second order moment of $R(t)$

$$\langle R^2(t) \rangle = \langle \|r^{(1)} - r^{(2)}\|^2 \rangle$$

where the average is over all the available trajectory pairs $(r^{(1)}, r^{(2)})$.

4.2.8 Sea Breeze Cases, Synoptic Wind Conditions, and WRF Sensitivities

As described above in Figs. 4.2 and 4.4, two sea breeze cases were used in this study. Both cases were *pure* sea breezes; that is, their largest synoptic wind component throughout the sea breeze time (17-00 UTC) was perpendicular to the NJ coastline. A WRF vertical level of 925mb was chosen as the height to determine the synoptic wind, consistent with [*Steele et al.*, 2014]. The choice of using only *pure* sea breeze cases is an important one because cross sections perpendicular to the NJ coastline will be taken. These cross sections will be parallel to the dominant synoptic flow component, thus

making the synoptic flow sensitivities clear and effective. Because *corkscrew* and *backdoor* sea breezes have their largest synoptic wind component parallel to the coastline, any synoptic flow sensitivities will become that much more complicated and less effective.

The first sea breeze case again occurred in the spring on April 27, 2013 with no coastal upwelling (Fig. 4.2). This sea breeze case will be used for demonstration of the new LCS technique, and will be used to test the limits of the offshore extent when the onshore front propagates all the way across the state of NJ.

The second sea breeze case occurred in the summer on August 13, 2012 with coastal upwelling (Fig. 4.4). This sea breeze case will be used to perform both the synoptic flow and upwelling sensitivities. For the synoptic flow sensitivity, weak synoptic offshore flow occurred over the Delmarva Peninsula with large inland frontal propagation, and strong synoptic offshore flow occurred over NJ with the inland front stalling near the coastline. For the upwelling sensitivity, a WRF simulation performed with August 13, 2012 upwelling SST conditions, was compared to another WRF simulation using the two days prior August 11, 2012 non-upwelling SST conditions.

4.3 Results

4.3.1 Case 1

During clear-air mode, KDIX weather radar base elevation scans first captured a sea breeze front stretching up and down and just inshore of the NJ coastline at ~1600 UTC on April 27, 2013. The front propagated inland to just east of the KDIX radar location at 1700 UTC (Fig. 4.6A), to just west of KDIX at 2000 UTC (Fig. 4.6C), to near

Trenton, NJ at 2300 UTC (Fig. 4.6E), and dissipating just west of Philadelphia, PA at ~0000 UTC on April 28, 2013.

LCS results at 100m at the same times (1700, 2000, and 2300 UTC) show a similar inshore picture (Figs. 4.6B, D, F). Vectors with a green 5 m s^{-1} legend show Eulerian WRF 100m horizontal winds averaged across the hour beginning at the time indicated on the panel (e.g. 17-18 UTC for Fig. 4.6B). Red and blue shading indicate RD minus the initial 10km separation distance of the particles. The result is the mean rate of separation of particles relative to the initial separation distance. This provides a speed (km/hr) of divergence (red) and convergence (blue). Based on the "convectional" theory of the sea breeze, blue convergent areas at 100m should align with the inland sea breeze front and red divergent areas at 100m should align with the offshore sea breeze divergence zone. The yellow dot indicates weather radar-captured position of the inland sea breeze front along the NW to SE cross section black line. The height of 100m was chosen for WRF winds and LCS results because a) the maximums in onshore convergence and offshore divergence are most pronounced at this height, b) the wind speed vectors are stronger at 100m than at 10m, and c) 100m corresponds to approximate hub height of offshore wind turbines, making this work more broadly applicable. The conclusions are insensitive to the choice of height as long as the choice is within the lower portion of the sea breeze circulation, or <~500m.

At 1700 UTC, the blue convergence zone stretches just inshore of the NJ coast, and aligns well with the yellow dot for weather radar frontal location (Fig. 4.6B). Blue convergent areas are also apparent along the Delmarva and Long Island coastlines. Offshore there is a broad area of red divergence, with local maxima in divergence just

offshore of NJ, in the Delaware Bay, and just offshore of Raritan Bay. Three hours later at 2000 UTC, the blue convergent area has progressed farther onshore with the yellow dot, and the red divergent area has progressed farther offshore, now southeast of the NJ WEA depicted with the black boxed outline southeast of NJ (Fig. 4.6D). Finally, at 2300 UTC, the blue convergent area has progressed all the way to the Delaware River/Philadelphia with the yellow weather radar dot, and the red divergent area has propagated offshore to southeast of the 50m isobath (black, Fig. 4.6F). Inshore of the red divergent area there is a zone of white, indicating neither divergence nor convergence in the Lagrangian wind field.

A Hövmoller diagram along the cross section indicated by the black line in Fig. 4.6B, D, and F is depicted in Fig. 4.7A, with time increasing down on the y-axis and distance offshore (km) increasing to the right on the x-axis. The same red/blue shading for Lagrangian divergent/convergent areas is used but here averaged across 50, 100, and 150m, as are the black WRF x-y wind vectors again averaged across 50, 100, and 150m, with the same yellow weather radar inland sea breeze front dot. The solid black vertical line indicates coastline location, and the two dashed vertical lines indicate the inshore and offshore boundaries of the NJ WEA. Finally, the green dotted lines indicate the trace of the maximum blue convergence onshore and the maximum red divergence within 150km offshore. Fig. 4.7B shows SST (°C) under the same cross section, while Fig. 4.7C shows terrain height and water depth (m) from the U.S. Coastal Relief Model data. SST is uniformly cold across the entire shelf out to ~130km offshore, increasing in temperature in the deep water off the shelf.

The blue convergence zone begins ~25km onshore at 1700 UTC, slowly propagating farther onshore to >100km onshore at 2300 UTC and well-aligned with the yellow weather radar dot (Fig. 4.7A). This is highlighted by the green dotted trace of the maximum blue convergence. The red divergence zone begins just offshore of the coast and propagates farther offshore at a similar rate as the inshore side, reaching almost to the shelf break by 2300 UTC, and again highlighted by the green dotted trace of maximum divergence. This maximum divergence—what we use as the offshore extent of the sea breeze cell—crosses the NJ WEA at ~1900 UTC. Thus, the sea breeze cell begins at a width of about 30 km centered on the coast and slowly and symmetrically expands onshore and offshore to about a width of nearly 250km after six hours.

4.3.2 Case 2

A sea breeze occurred along both the NJ (Fig. 4.8 left panel) and Delmarva (Fig. 4.8 right panel) coastlines on August 23, 2012 (Fig. 4.8). Due to strong northwest synoptic wind conditions, the sea breeze front stalled out along the NJ coastline from 1700 UTC (Fig. 4.8A) to 2300 UTC (Fig. 4.8E). At the Delmarva peninsula and due to lighter northwest synoptic winds, the sea breeze propagated through almost the entire state of Delaware by 2300 UTC (Fig. 4.8F).

LCS simulation results at 100m are shown at the same three times as the weather radar, with WRF 100m wind vectors and yellow dots for NJ and Delmarva weather radar inland sea breeze front locations along the NJ cross section and a new Delmarva cross section, both shown in the northwest to southeast lines. The left panel (Fig. 4.9 A, C, and E) shows WRF and LCS simulation results from the August 13, 2012 upwelling SST bottom boundary condition, and the right panel (Fig. 4.9 B, D, and F) shows the August

11, 2012 non-upwelling bottom boundary condition. The stalled out front over the NJ coastline is again apparent in the blue convergence shading for both upwelling and non-upwelling, with the blue convergence zone expanding in size onshore through time. Over the Delmarva peninsula, the blue convergence zone propagates onshore with the yellow weather radar dot. Offshore, though more subtle than the April 27, 2013 case, the red divergence zone can be seen propagating offshore along the NJ cross section line, and much more clearly can be seen propagating offshore of the Delmarva peninsula. Comparing upwelling to non-upwelling shows darker red divergence for the upwelling case at all three times and for both the NJ and Delmarva sea breezes. Onshore, differences in blue convergence intensities are less apparent between upwelling and non-upwelling.

Fig. 4.10 shows the same Hövmoller formatted plot (50-150m average) as Fig. 4.7, with upwelling on the left and non-upwelling on the right, and strong synoptic wind conditions (NJ) at the top and weak synoptic wind conditions (Delmarva, "MD") at the bottom. Traces of maximum onshore blue convergence and maximum offshore red divergence are colored to match Fig. 4.10, described later. Yellow weather radar dots are shown for the upwelling case (NJ and MD) on both the right and left panels for direct comparison.

It is immediately apparent that, again, blue onshore convergence aligns well with yellow weather radar dots throughout both upwelling and non-upwelling sea breezes. Comparing upwelling to non-upwelling shows small differences in propagating speeds and extents for both the onshore and offshore sides, with potentially greater differences in intensities, as will be shown in the next figure. Comparing synoptic flow strength: for

strong synoptic flow, inland blue convergence remains stationary, while the offshore red divergence propagates offshore (Fig. 4.10A1 and B1); for weak synoptic flow, inland blue convergence propagates inland, while the offshore red divergence propagates offshore (Fig. 4.10C1 and D1).

4.3.3 Composite of Sea Breeze Sensitivities

A composite of the Hövmoller traces from Figs. 4.7 and 4.10 is shown in Fig. 4.11B. The same formatting is used, with the black solid line indicating the coastline, the colored solid lines (blue for upwelling, red for non-upwelling) representing the onshore convergence and offshore divergence traces for strong synoptic conditions (NJ), the dotted green line representing the same but for weak synoptic conditions (NJ) for the April 27, 2013 case, and the dotted blue (upwelling) and red (non-upwelling) lines representing the same but for weak synoptic conditions (MD). The blue closed dots represent weather radar inland frontal location for the strong synoptic upwelling (NJ), the blue open dots represent the same for the weak synoptic upwelling (MD), and the green open dots represent the same for the weak synoptic non-upwelling (NJ) April 27, 2013 case.

For sea breeze extent sensitivity to synoptic flow, the inshore side is sensitive with all dotted lines propagating at approximately the same speed, ending at ~80-110km onshore, and both solid lines stalling close to the coastline (within ~40km) and not propagating onshore against the strong offshore synoptic wind. The offshore side is not sensitive to synoptic flow, with both dotted and solid lines all propagating well offshore to the shelf break and beyond, and ending at ~80-130km offshore.

For sea breeze extent sensitivity to upwelling, both the inshore and offshore sides are insensitive—the red and blue dotted and solid line pairs are aligned with each other throughout the entire six-hour period. However, as will be shown next, upwelling does have an impact on the intensity of the sea breeze cell.

For the strong synoptic (NJ) case, Fig. 4.11A shows, for onshore convergence, and Fig. 4.11C shows, for offshore divergence, that upwelling produces a more intense sea breeze on both sides of the circulation. These panels show the difference between upwelling and non-upwelling of the most negative convergence onshore (Fig. 4.11A), and the same for the maximum divergence offshore (Fig. 4.11C). This difference is calculated by taking the average across the three grid cells centered on the most negative convergence inshore and most positive divergence offshore, producing a sensitivity of the intensity at both sides of the sea breeze cell to upwelling. Upwelling produces a more intense sea breeze, especially early on, with differences in convergence approaching -2 km/hr at 1800 UTC and differences in divergence approaching +2 km/hr also at 1800 UTC. On average, convergence difference is -0.58 and divergence difference is 0.45 km/hr.

To investigate possible reasons why the sea breeze is more intense on both the onshore and offshore sides, especially earlier on in the circulation, we turn to panel D. Here, the difference in SST over the NJ cross section between upwelling and non-upwelling (Fig. 4.11G) is used. This SST upwelling-non-upwelling difference is averaged from the coast to the blue solid line representing the maximum divergence location and offshore extent of the strong synoptic upwelling sea breeze. This average $SST_{upwelling}$-$SST_{non-upwelling}$ difference peaks at nearly -3°C at 1900 UTC, and is greater than -1°C

throughout the entire sea breeze lifetime (Fig. 4.11D). In other words, a greater

percentage of the sea breeze cell is "feeling" the upwelling underneath it earlier on when

the sea breeze cell is small, until the sea breeze cell expands offshore past the upwelling

and the cell "feels" the effects of the warmer waters offshore of the upwelling.

The dynamic theory of the sea breeze [*Simpson et al.*, 1977] is shown by the gray

ribbon bounded by the skin and 2m temperatures for land-sea temperature differences in

the calculation of inland sea breeze frontal propagation speed (Fig. 4.11B). From

[*Simpson et al.*, 1977], the rate of advance of the inland sea breeze front can be expressed

as:

$$u = \{ \, [\, T_{\text{Land}} - T_{\text{Water}} \,] \, g \, h \, / \, 2T \, \}^{1/2} \quad (1)$$

where T_{Land} is land temperature (K), T_{Water} is sea temperature (K), g is gravity, h is vertical

scale of the heating (350m), and T is a reference temperature ~300K. This behavior can

be expected as long as the synoptic wind component across the coast is very small

[*Simpson et al.*, 1977]. T_{Land} and T_{Water} are based on average temperatures under the three

weak synoptic wind condition cases (two non-upwelling and one upwelling, dotted lines

in Fig. 4.11B), or the sea breeze cells that are less affected by the synoptic flow. T_{Land} is

calculated by taking the average skin/2m temperature from the coast to each of the three

inland dotted lines, and averaging those three values. T_{Water} is calculated the same way

but from the coast to each of the three offshore dotted lines. Assuming that the inland sea

breeze front begins at the coastline, the gray dotted lines are plotted based on the speed u

calculated using Equation 1. Because land-sea skin temperature differences are greater

than land-sea 2m temperature differences, the skin temperature gray dotted line has a

faster inland propagation speed and ends ~150km onshore, with the 2m temperature gray

dotted line ending ~75km onshore. The three colored dotted lines inland fall within the gray ribbon bounded by the two gray dotted lines, indicating that our weak synoptic results are consistent with dynamic linear theory of the sea breeze according to [*Simpson et al.*, 1977].

In order to complete the comparison with [*Simpson et al.*, 1977], synoptic winds were "removed" from the two strong synoptic condition sea breeze cases (solid red and blue inland lines). To do this, for the August 13, 2012 strong synoptic (NJ) upwelling sea breeze case, the 925mb horizontal wind speed component parallel to the NJ cross section was taken at the closest WRF grid point to KPHL at each hour from 1700 to 2300 UTC. Then, the average of those seven values was taken, resulting in 4.56 m s^{-1}. In comparison, for the August 13, 2012 weak synoptic (MD) upwelling sea breeze case taken at KOBX gives a value of 0.61 m s^{-1}, and for the April 27, 2013 weak synoptic (NJ) non-upwelling sea breeze case taken at KPHL gives a value of 1.9 m s^{-1}. To get the inland propagation of the sea breeze that would have resulted if the strong synoptic winds were removed, the mean of 4.56 m s^{-1} was removed at each of the seven hours, resulting in the leftward black arrow labeled "Strong Synop Removed" in Fig. 4.11B. Instead of stalling near the coast due to the opposing strong synoptic winds, the sea breeze inland front would have propagated ~130 km inland, within the gray [*Simpson et al.*, 1977] ribbon.

A second comparison to dynamic linear theory of the sea breeze is plotted as the horizontal gray line at the bottom of Fig. 4.10B labeled "Rotunno 1983". This line indicates the horizontal extent of the sea breeze according to linear theory of motion:

For $f > \omega$ (latitudes>30°): $Nh(f^2 - \omega^2)^{-1/2}$ (2)

where $f = 2\Omega\sin\phi$ is the Coriolis frequency, $\omega = 2\pi$ day^{-1} is the frequency of diurnal

heating of land, $N = [(g/\theta_0)(\partial\theta/\partial z)]^{1/2}$ is the Brunt-Väisälä frequency (stratification), and h

is the vertical scale of the heating (350m as above) [*Rotunno*, 1983]. Plugging in numbers

for our sea breeze cases at latitude 40°N, we get:

$$Nh(f^2 - \omega^2)^{-1/2} = [(g/\theta_0)(\partial\theta/\partial z)]^{1/2} * 350m * [(2\pi/64800\ s)^2 - (2\pi/86400\ s)^2]^{-1/2}$$

$$= [(9.81/300K)(10K/1000m)]^{1/2} * 350m * [(2\pi/64800\ s)^2 - (2\pi/86400\ s)^2]^{-1/2}$$

$$\sim= \mathbf{\textit{100 km}}$$

This means that according to [*Rotunno*, 1983] linear theory of the sea breeze, the onshore

and offshore extents of our sea breeze cases should both reach ~100km from the coast.

All Hövmoller traces match within this +/-100km distance from the coast, again

consistent with linear dynamic theory of the sea breeze.

Fig. 4.11E ("Skin T") and Fig. 4.11F ("2m T") show the temperature difference

T_{Land} - T_{Water} that the sea breezes "feel", or the thermal gradient driving each sea breeze.

Again, this is calculated similar to the above, where T_{Land} is the average skin/2m

temperature from the coast to the inland boundary, and T_{Water} is the average skin/2m

temperature from the coast to the offshore boundary. First, skin temperature differences

are larger than 2m temperature differences for the first four hours. Second, the solid blue

upwelling lines are always greater than the solid red non-upwelling lines, indicating a

stronger thermal gradient with upwelling than without, under strong synoptic forcing.

Third, for skin T, the dotted blue upwelling line is always greater than the dotted red non-

upwelling line, again indicating stronger thermal gradient forcing with upwelling than

without, under weak synoptic forcing. For comparison, past studies have found that a

"critical" thermal land-sea gradient to allow for sea breeze formation is ~5°C using 2m temperature [*Simpson*, 1994; *Miller et al.*, 2003; *Bowers*, 2004; *Steele et al.*, 2014].

It is also stated in [*Rotunno*, 1983] that the sea breeze has "an elliptically shaped pattern of flow in the vertical plane, centered on the coast, having an aspect ratio (vertical/horizontal scale) given by:"

For $f > \omega$ (latitudes>30°): $(f^2 - \omega^2)^{1/2} N^{-1}$ (3)

where, as before, $f = 2\Omega\sin\phi$ is the Coriolis frequency, $\omega = 2\pi$ day^{-1} is the frequency of diurnal heating of land, and $N = [(g/\theta_0)(\partial\theta/\partial z)]^{1/2}$ is the Brunt-Vaisala frequency (stratification). Plugging in numbers for our sea breeze case, we get:

$(f^2 - \omega^2)^{1/2} N^{-1}$ $= [(2\pi/64800 \text{ s})^2 - (2\pi/86400 \text{ s})^2]^{1/2} * \{[(g/\theta_0)(\partial\theta/\partial z)]^{1/2}\}^{-1}$

$= [(2\pi/64800 \text{ s})^2 - (2\pi/86400 \text{ s})^2]^{1/2} * [(9.81/300\text{K})(10\text{K}/1000\text{m})]^{-1/2}$

$\sim= \textbf{0.0035}$ *vertical/horizontal scale*

Checking answer:

$h/Nh(f^2 - \omega^2)^{-1/2} = 350\text{m (vertical scale)}/100,000\text{m (horizontal scale)} = \textbf{0.0035}✔.$ For comparison, [*Rotunno*, 1983] stated an aspect ratio of 0.00685 for their idealized sea breeze case.

4.3.4 WRF Cross Sections and Profiles

To further investigate the impact of upwelling on sea breeze *intensity*, vertical cross sections at three different hours (1700, 1900, and 2200 UTC) were taken of temperature and wind velocity component along the same NJ cross section used above. These cross sections for upwelling, non-upwelling, and upwelling minus non-upwelling are shown in Fig. 4.12. Temperature (°C) is shaded and wind velocities (m s^{-1}, both horizontal and vertical component) are plotted in vectors, with weather radar sea breeze

front location indicated by the yellow closed dot, coastline indicated by the black closed

dot, NJ WEA center location indicated by the black asterisk with ~top of blade tip height

for wind turbines plotted with thick horizontal black line, and two times the distance

offshore from coastline to NJ WEA indicated by the black "x" in all figures. Wind

vectors are exaggerated in the difference plots in the middle panel (see 5 m s^{-1} legends).

Upwelling produces colder air right above the surface, with warmer air above that

at ~400-700m, at all three hours plotted (Fig. 4.12B, E, and H). The colder and warmer

air regions increase in height downstream of the synoptic wind flow in the same

difference panels. Difference vectors directly above the coast show sea breeze

enhancement due to upwelling up to ~750m, and return flow enhancement >750m in

height. Also, more sinking air due to upwelling can be seen directly above the coast,

especially by 2200 UTC.

Vertical profiles were taken at three locations along the cross sections: at the coast

(black dot), at the edge of the upwelling in the NJ WEA (black asterisk), and at the

offshore location (black "x"). These vertical profiles at 1700, 1900, and 2200 UTC are

shown on semi-log plots in Fig. 4.13. The conclusions up front are as follows:

1. Upwelling sea breeze onset is earlier

2. Upwelling sea breeze is shallower, sharper, and narrower, consistent with
    [*Clancy et al.*, 1979] and [*Bowers*, 2004]

3. Upwelling and non-upwelling sea breeze "shape" become similar by the end
    of the sea breeze

4. The difference between the upwelling and non-upwelling sea breeze profiles
    is an enhanced sea breeze near surface and an enhanced return flow aloft

The three times were chosen because at 1700 UTC the upwelling sea breeze wind speed is 0 at the coast, at 1900 UTC the non-upwelling sea breeze wind speed is 0 at the offshore location, and at 2200 UTC the non-upwelling sea breeze wind speed is 0 at the coast.

At 1700 UTC, the upwelling sea breeze cell (blue) starts just over the edge of the upwelling, but has not quite expanded to the coast or offshore yet. The non-upwelling sea breeze cell (red) onset has not occurred yet at all three locations. At 1900 UTC, the upwelling sea breeze cell has now expanded over all three locations, with the non-upwelling sea breeze cell at the edge of upwelling location but not at the other two locations yet. Finally, at 2200 UTC, the upwelling sea breeze cell strengthens at all three locations, and the non-upwelling sea breeze cell is at the edge of the upwelling and offshore, but not at the coast. These sea breeze cell onset, expansion, and evolution results can also be seen in Fig. 4.11.

At 1700 and 1900 UTC, the upwelling sea breeze profile is shallower and sharper than the non-upwelling sea breeze profile. Then, at 2200 UTC, the sea breeze shapes eventually become similar, especially at the edge of upwelling (Fig. 4.13H) and offshore (Fig. 4.13I) locations.

4.4 Summary and Discussion

In this chapter, the utility of LCS to highlight, clarify, and objectively define the offshore extent of the sea breeze has been shown, and sensitivities of both the onshore and offshore components of the sea breeze to synoptic flow and upwelling were tested using the new LCS technique. Previous studies [e.g. *Arritt*, 1989; *Finkele*, 1998] have attempted to define the offshore extent, but these definitions have remained either only

applicable for *pure* sea breeze cases (offshore synoptic wind conditions), or difficult to objectively identify. By using the Lagrangian framework, the onshore maximum convergence and the offshore maximum divergence can now be objectively and clearly marked as the onshore and offshore boundaries of the sea breeze cell, regardless of sea breeze type, geostrophic wind, or upwelling presence. The onshore convergence in LCS aligns well with weather radar observations of the sea breeze frontal convergence and propagation.

Using the objective LCS sea breeze boundary metric, sensitivities of sea breeze extent and intensity to synoptic wind strength and upwelling were performed. The inland sea breeze extent was found to be very sensitive to synoptic flow, but the offshore sea breeze extent was not, consistent with [*Finkele*, 1998] who found that offshore sea breeze extent is less sensitive to offshore synoptic wind than its inland extent. Upwelling did not have an impact on either onshore or offshore sea breeze extent, in contrast to [*Clancy et al.*, 1979] which found that upwelling sea breeze "penetrates more than twice as far inland than it would without the upwelling", and also in contrast to [*Bowers*, 2004], which found that, depending on the case, upwelling can force the inland sea breeze front to penetrate several kilometers farther onshore than without upwelling. [*Bowers*, 2004] also found that the offshore extent is roughly two to three times that of the inland penetration, whereas the results here show approximately the same offshore extent as onshore extent, depending on the synoptic wind conditions.

While upwelling did not influence the onshore or offshore sea breeze extent, it did have an impact on sea breeze *intensity*, with stronger convergence onshore and stronger divergence offshore during upwelling conditions. The sea breeze intensity starts much

stronger with upwelling, with the upwelling minus non-upwelling sea breeze intensity difference gradually decreasing as the sea breeze cell expands outward and offshore of the upwelling. Further, upwelling causes an earlier sea breeze onset, and a shallower, sharper, and narrower sea breeze profile, consistent with idealized modeling [*Clancy et al.*, 1979], observations and modeling for Brazil [*Franchito et al.*, 1998], and prior studies specific to NJ [*Bowers*, 2004].

Using High Frequency (HF) Radar surface ocean current data, *Hunter et al.*, 2007 found that diurnal wind-forced motions in the NJ coastal ocean, associated with the sea/land breeze system, can extend as far as 100 km offshore. These results are consistent with findings here, which showed that the maximum divergence in the LCS field propagates to approximately 100-150km offshore, regardless of synoptic wind conditions.

Future work should investigate several more cross sections up and down the NJ coastline to study the along-coast variability in the sea breeze circulation, especially where it interacts with the Delaware Bay Breeze in far southern NJ. Also, a sea breeze climatology should be performed, similar to [*Steele et al.*, 2014], for NJ and for other upwelling-sea breeze regimes globally, and for the different sea breeze types. For a *pure* sea breeze, an inland front forms due to the presence of the land-sea thermal gradient and opposing offshore synoptic winds. During coastal upwelling in the *synoptic* sea breeze, does an offshore front form due to the presence of the thermal gradient between the cold upwelling and warmer offshore waters and opposing onshore synoptic winds? This "offshore" front was not found to occur during the *pure* sea breeze with upwelling case investigated in this chapter. Further, for a *corkscrew* sea breeze and its southwesterly

synoptic flow conditions, what is the interaction between the sea breeze and the southwest to southerly New York Bight jet, the climatology of which is described in detail by [*Colle and Novak*, 2010]?

A high-resolution fully-coupled ocean-atmosphere model that resolves coastal upwelling should be used to study the feedback processes between upwelling and sea breeze. Wind shear and turbulence dimensional characteristics of each sea breeze type should be investigated. Large eddy simulation (LES) could be used to examine the turbulence properties during sea breeze and non-sea breeze days, and potential turbulent impact on the offshore wind resource for offshore wind energy development.

Finally, observational studies should be performed, to explore air-sea interaction processes between upwelling and sea breeze, and to determine if the sinking air and offshore surface divergence has an effect on the surface current and wave field in the ocean. To accomplish this, LCS could be calculated on HF radar surface current fields to see if any coherent divergence regions in the surface ocean align with the LCS maximum divergence in winds for the offshore sea breeze extent.
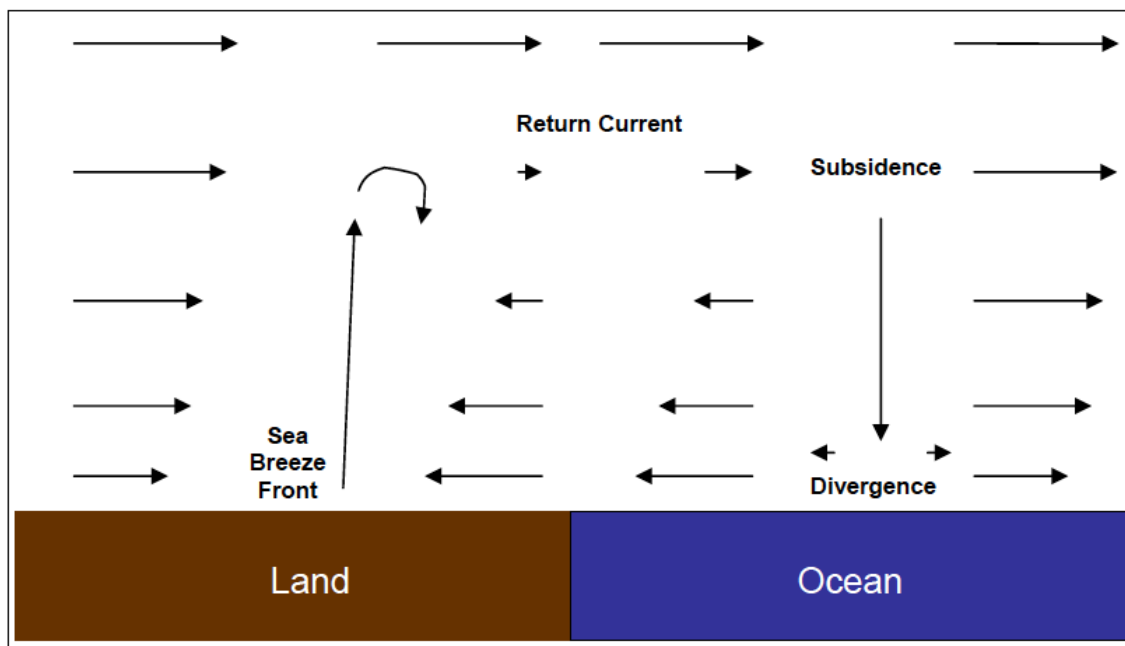
Figure 4.1 Box model of the sea breeze circulation, repeated from [*Bowers*, 2004]. Thermal contrast between land and ocean results from land heating up more quickly than water. The circulation involves rising air associated with warm air over land, sinking air (subsidence) and surface divergence associated with colder air over water, as well as sea breeze winds at the surface and return current winds aloft. Note offshore synoptic wind conditions in this figure.
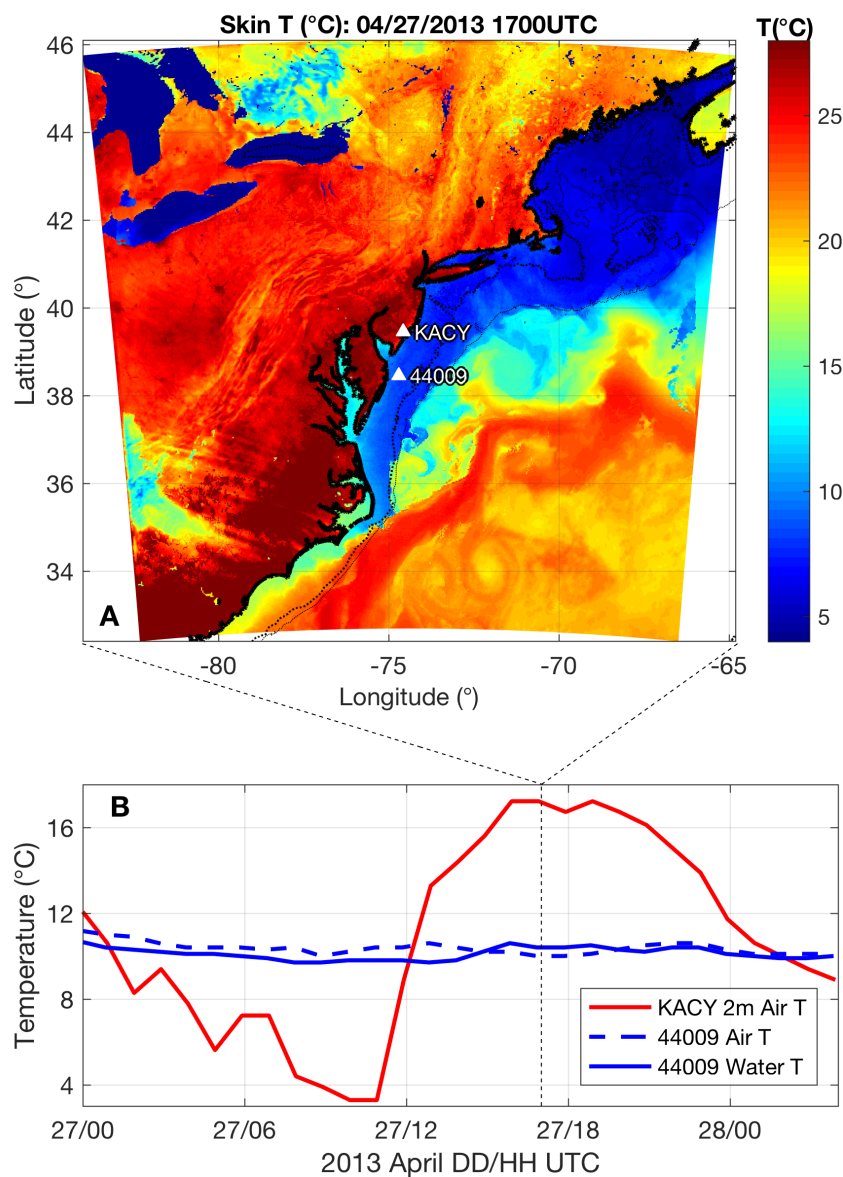
Figure 4.2 (A) WRF skin temperature (°C) at 1700 UTC on April 27, 2013, showing the entire WRF domain. Yellow triangles mark KACY and NDBC buoy 44009 locations, and thick dotted black contour 50m isobath and thin dotted black contour 200m isobath. (B) Time series of KACY 2m air temperature, 440009 air temperature, and 44009 water temperature (°C), with vertical dotted line marking time of WRF skin temperature map above.
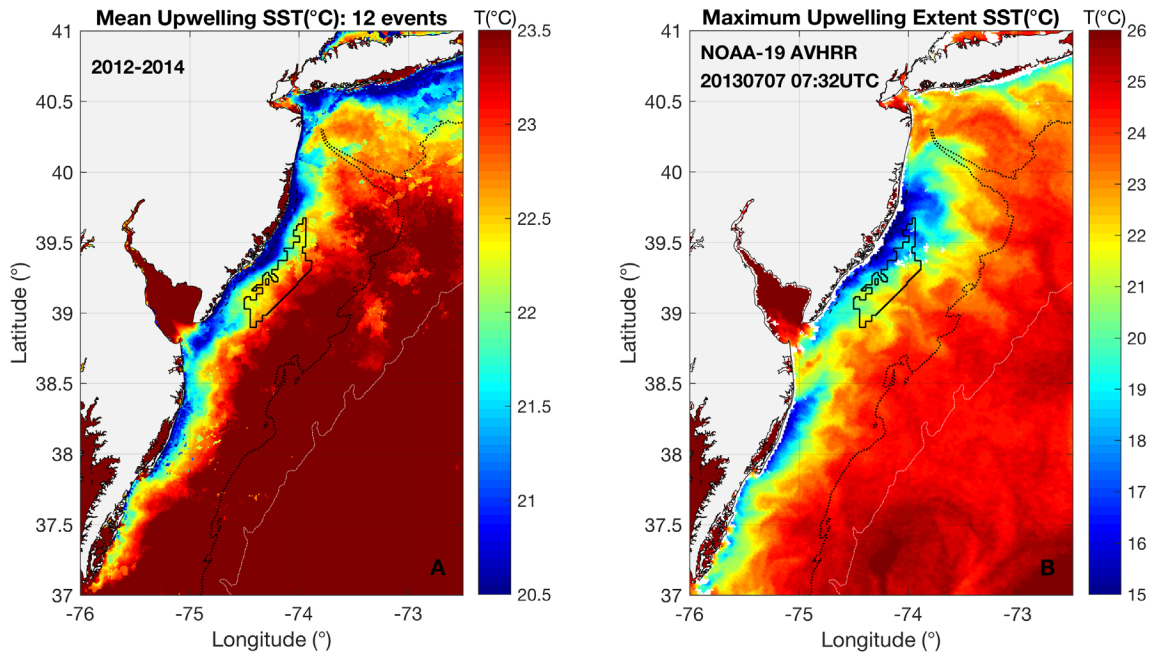
Figure 4.3 (A) The average SST (°C) across one representative AVHRR scan for each the 12 upwelling events that occurred 2012-2014. NJ WEA plotted in black boxed contour SE of NJ, black contour 50m isobath, and white contour 200m isobath. (B) Same as (A) but for maximum upwelling extent SST (°C) during the 2012-2014 period.
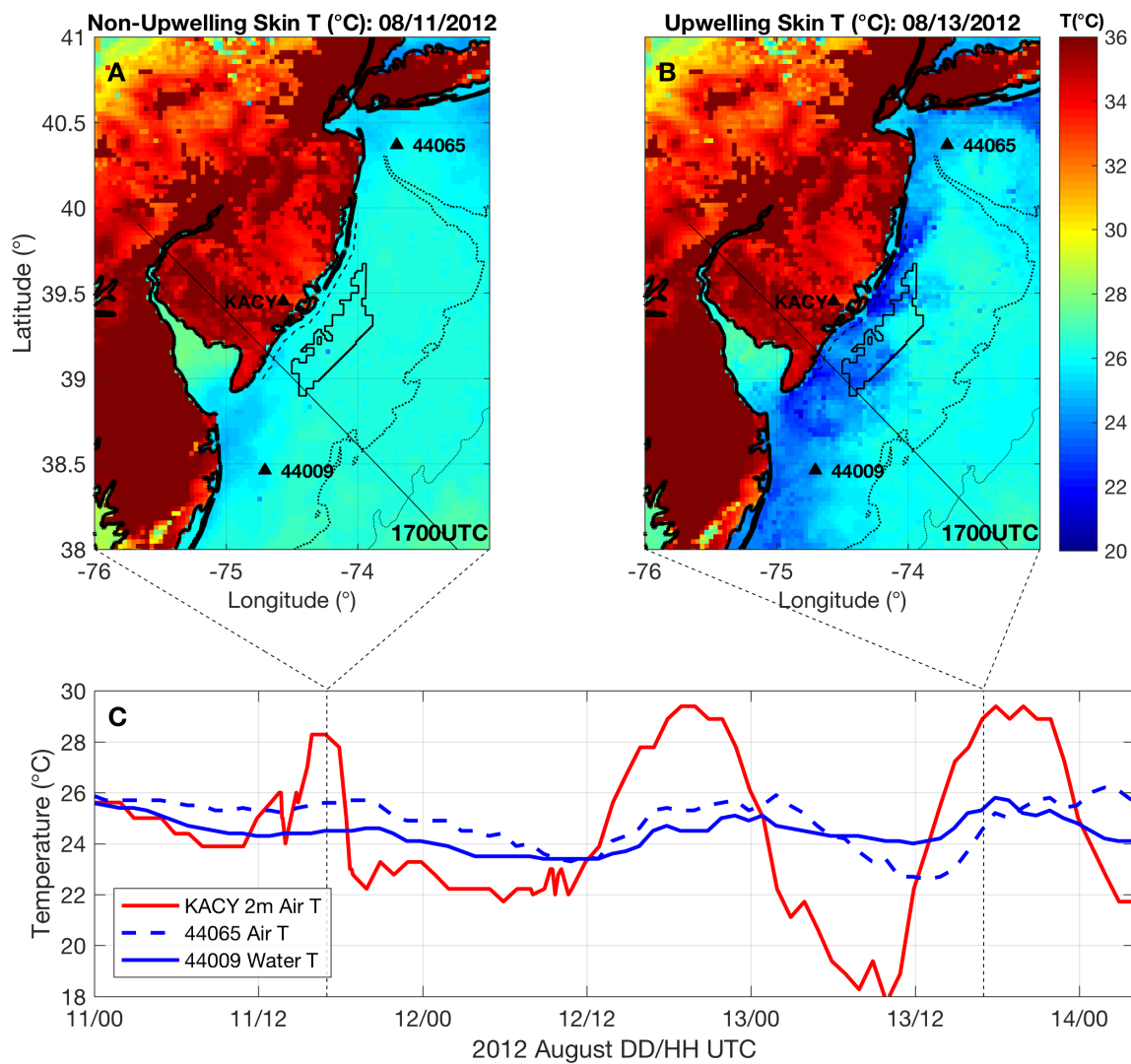
Figure 4.4 Same as Fig. 4.1 but for the August 13, 2012 upwelling case, with non-upwelling WRF skin temperature (°C) (A) two days prior to the upwelling WRF skin temperature (B). NDBC buoys 44065, 44009, and KACY marked as black triangles.
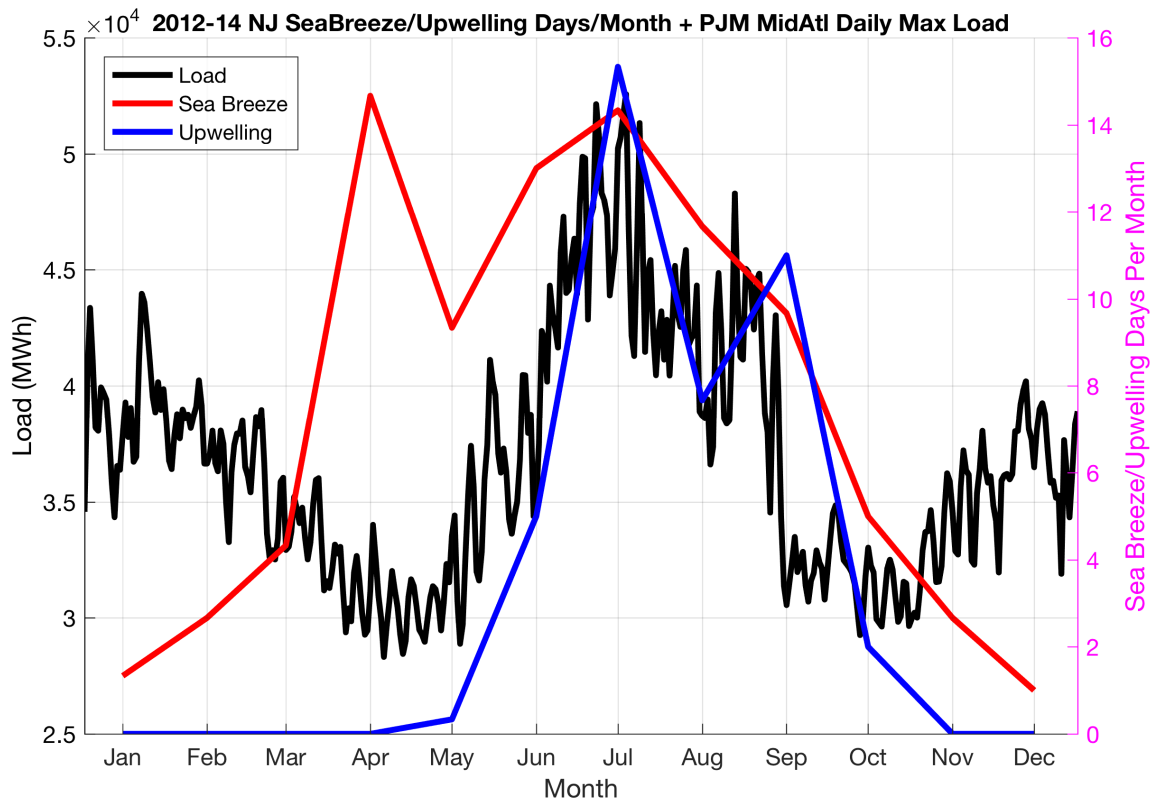
Figure 4.5 2012-2014 averaged PJM Mid-Atlantic region daily max load (black, MWh), 2012-2014 NJ sea breeze (red) and upwelling (blue) days per month.

Figure 4.6 KDIX weather radar base elevation scan in clear-air mode (left) at 1700 (top), 2000 (middle), and 2300 (bottom), showing inland propagation of sea breeze front. RD-10km (km/hr) at 100m, or mean rate of separation relative to the initial 10km separation distance, shaded red (divergence) and blue (convergence) at right and at the same three times. NJ WEA marked in black boxed contour, 50m isobath in thick dotted black

contour, 200m isobath in thin dotted black contour, cross section location used in figures below plotted northwest to southeast in black, yellow dot representing intersection of weather radar sea breeze front with cross section, and green 5 m s^{-1} legend for black WRF 100m wind vectors averaged across the hour beginning at time indicated on panel.
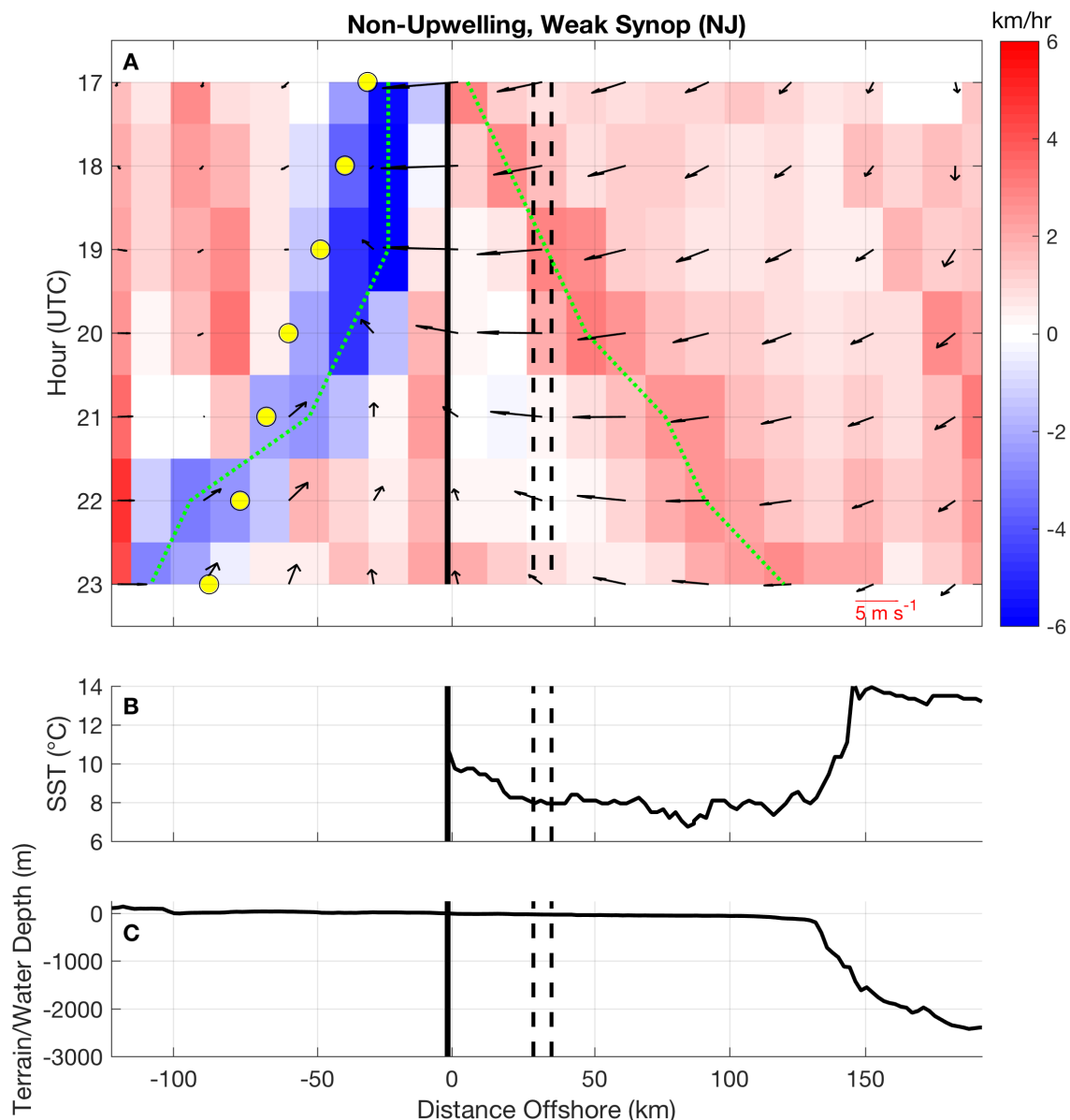
Figure 4.7 (A) Hövmoller of RD-10km (km/hr) averaged across 50, 100, and 150m shaded for the non-upwelling weak synoptic condition (NJ) case April 27, 2013, along the cross section indicated in Fig. 4.5B, D, and F; red shading for divergence and blue shading for convergence. Black vectors represent averaged WRF wind vectors across 50, 100, and 150m, and across hour beginning at time indicated on y-axis. Green dotted line traces maximum convergence onshore and maximum divergence within 150km offshore. Black solid vertical line marks the coast, and two black dashed vertical lines mark the inshore and offshore boundaries of the NJ WEA. (B) SST (°C) along the cross section. (C) Terrain height (m) onshore and water depth (m) offshore along the cross section.
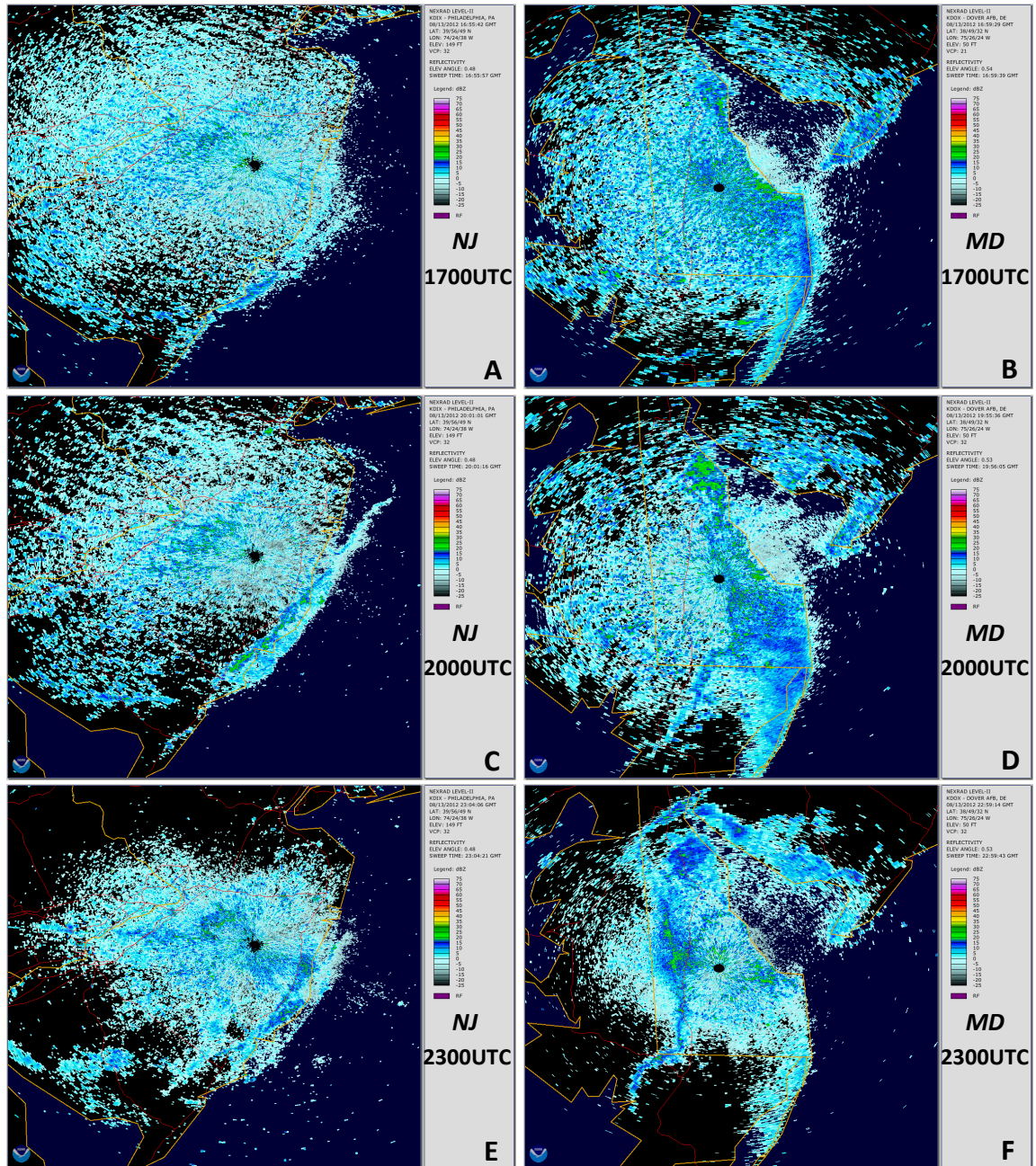
Figure 4.8 Same as Fig. 4.5 left panel but for the August 13, 2012 upwelling case, with NJ on left and MD on right.
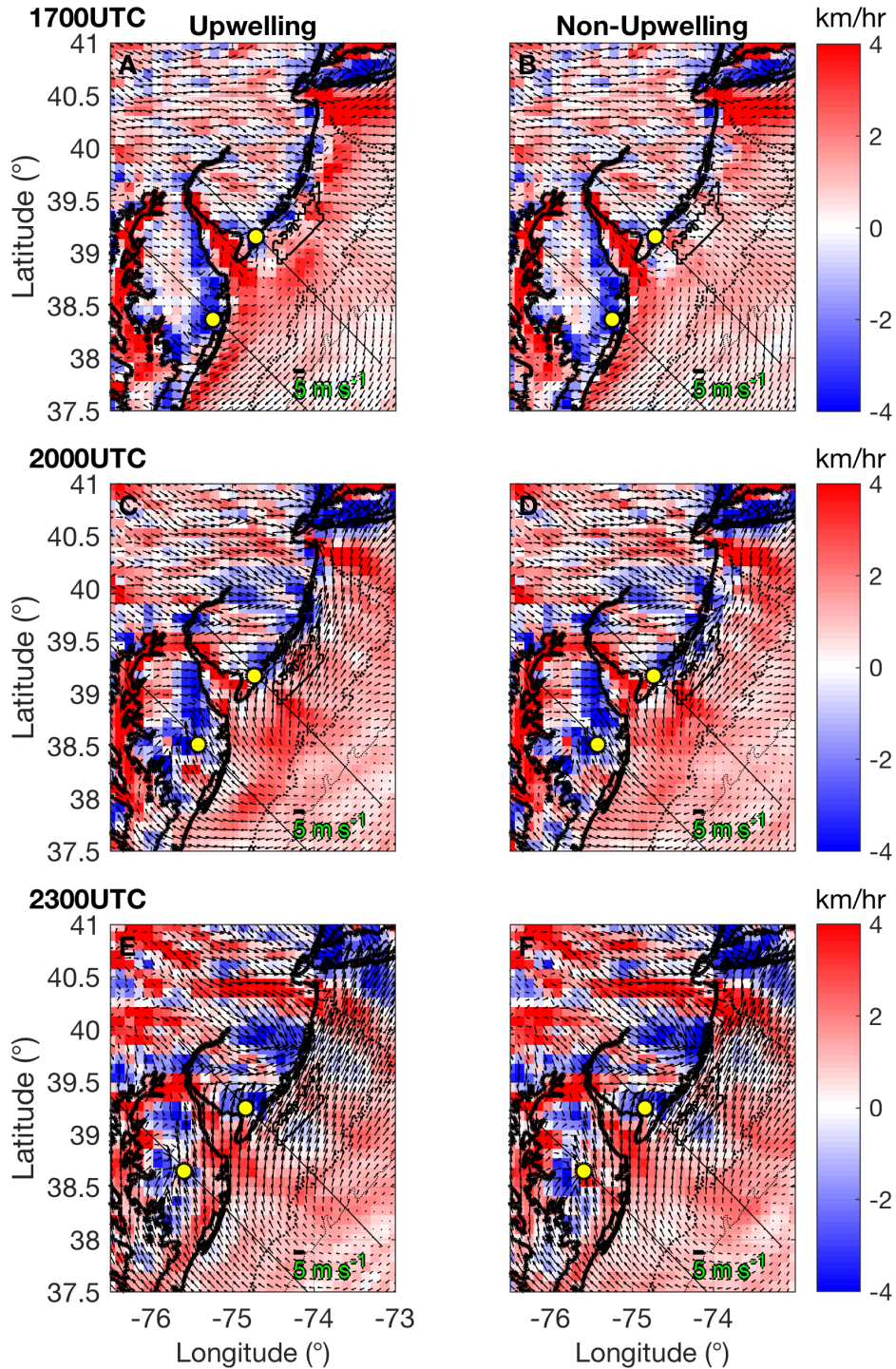
Figure 4.9 Same as Fig. 4.5 right panel but for the August 13, 2012 upwelling case, with results from the WRF simulation using upwelling SST conditions on left, and from the WRF simulation using non-upwelling SST conditions from two days prior on August 11, 2012 on right. Cross section location for both NJ and MD are shown, with yellow dots marking the intersection of the respective inland sea breeze front with the cross section.
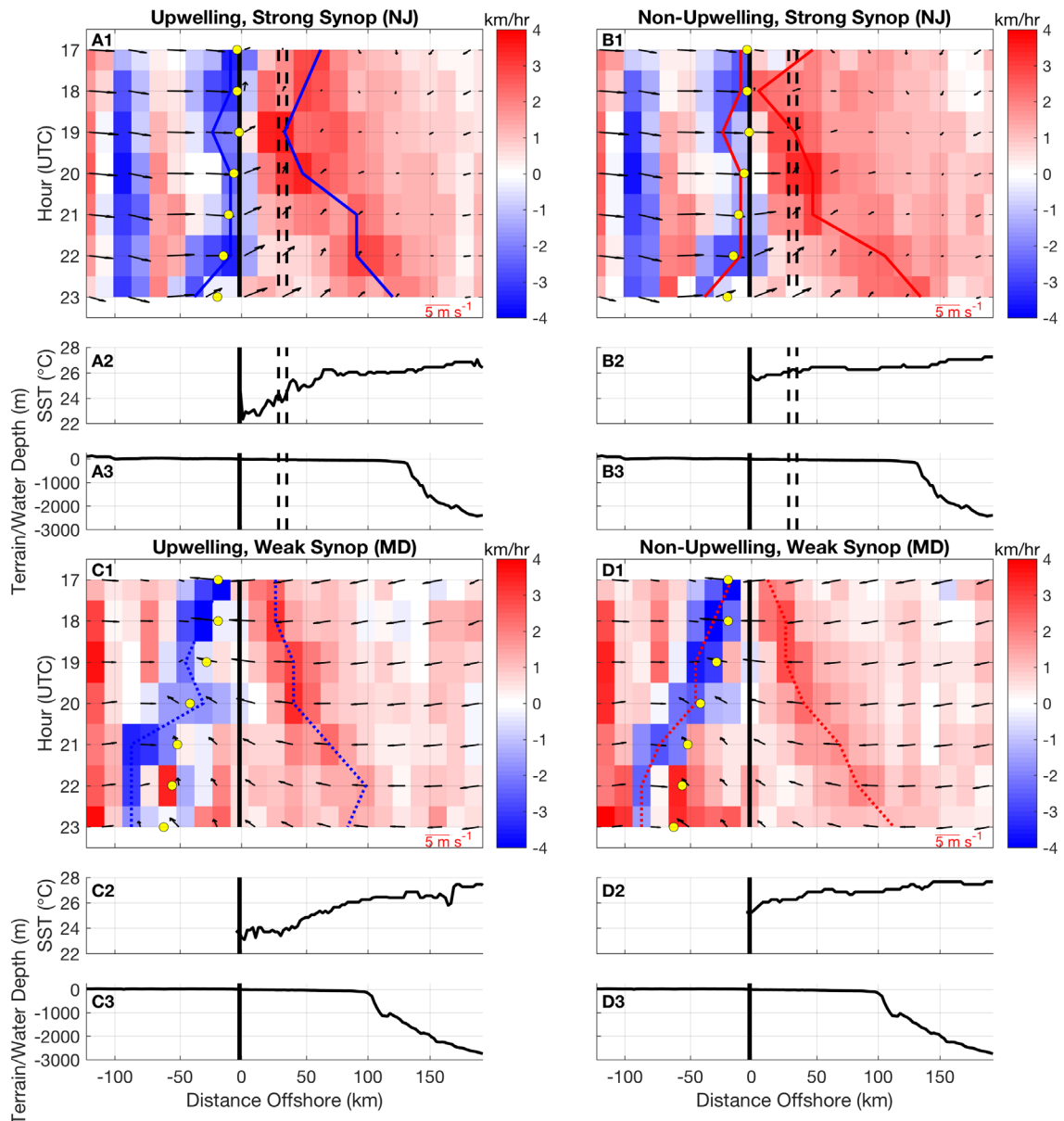
Figure 4.10 Same as Fig. 4.6 but for the August 13, 2012 upwelling case, with upwelling on left and non-upwelling on right, and strong synoptic conditions (NJ) at top and weak synoptic conditions (MD) at bottom.
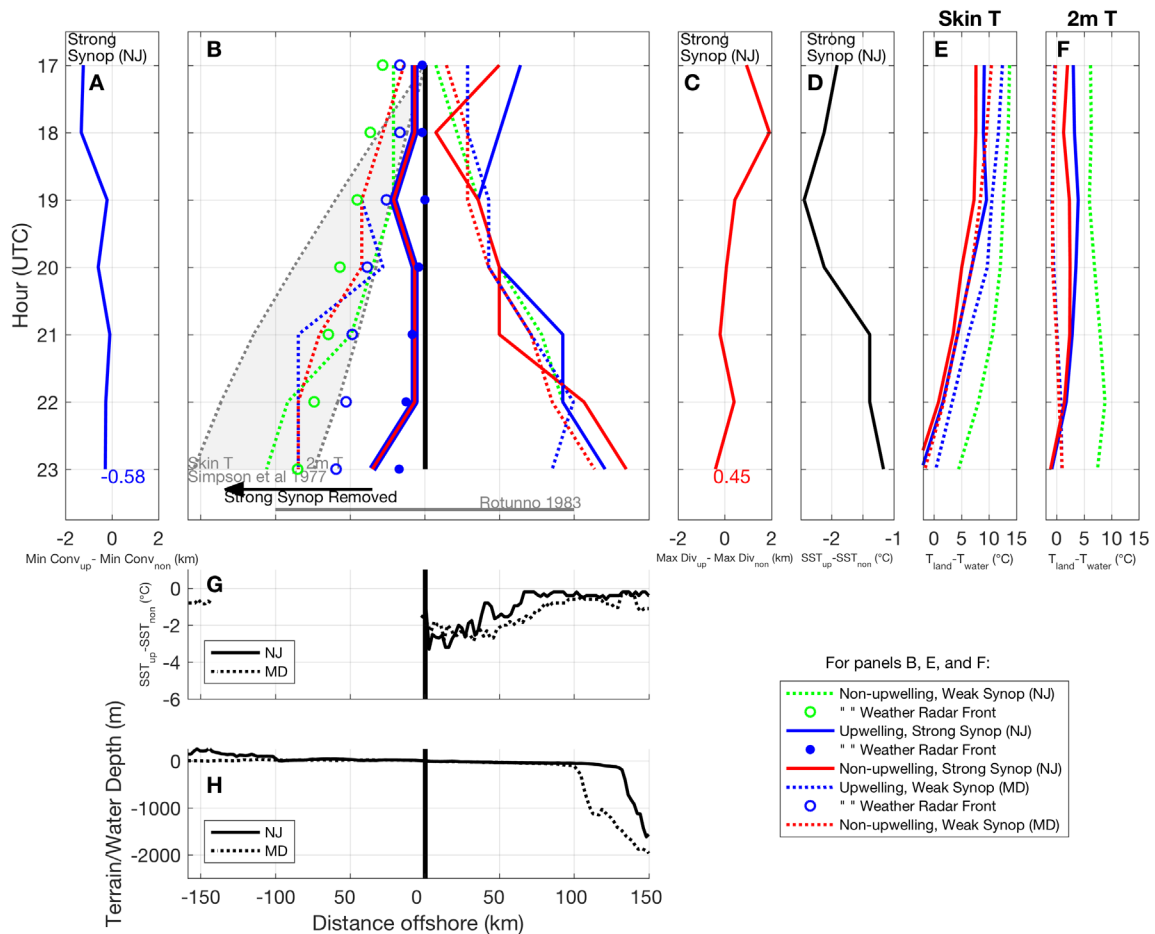
Figure 4.11 (B) Hövmoller traces of maximum convergence onshore and maximum divergence offshore, preserving the same coloring from Figs. 4.6 and 4.9. Weather radar frontal locations marked by open green circle for non-upwelling weak synoptic conditions (NJ), open blue circle for upwelling weak synoptic conditions (MD), and closed blue circle for upwelling strong synoptic conditions (NJ). Black vertical line represents the coast, and gray ribbon represents [*Simpson et al.*, 1977] linear theory of inland sea breeze propagation using WRF skin temperature (gray dotted left boundary) and 2m temperature (gray dotted right boundary). Black arrow pointing left and labeled "Strong Synop Removed" indicates the distance onshore that the solid blue and red lines would have traveled if the synoptic wind along the cross section were removed. Horizontal gray line represents sea breeze linear theory for horizontal extent from [*Rotunno*, 1983]. (A) and (C): for strong synoptic conditions (NJ), time series of upwelling minimum convergence (averaged across three grid cells around minimum) minus non-upwelling minimum convergence (A), and time series of upwelling maximum divergence minus non-upwelling maximum divergence (C). (D) For strong synoptic conditions (NJ), time series of upwelling SST minus non-upwelling SST, averaged from coast to offshore extent in panel (B). (E) and (F): $T_{Land} - T_{Water}$ time series using skin temperature (E) and 2m temperature (F), averaged from coast to onshore extent for T_{Land}, and from coast to offshore extent for T_{Water} in panel (B). (G) Upwelling SST minus non-upwelling SST (°C) for NJ (solid black) and MD (dotted black) under cross sections. (H)

Terrain height (m) onshore and water depth (m) offshore for NJ (solid black) and MD (dotted black).
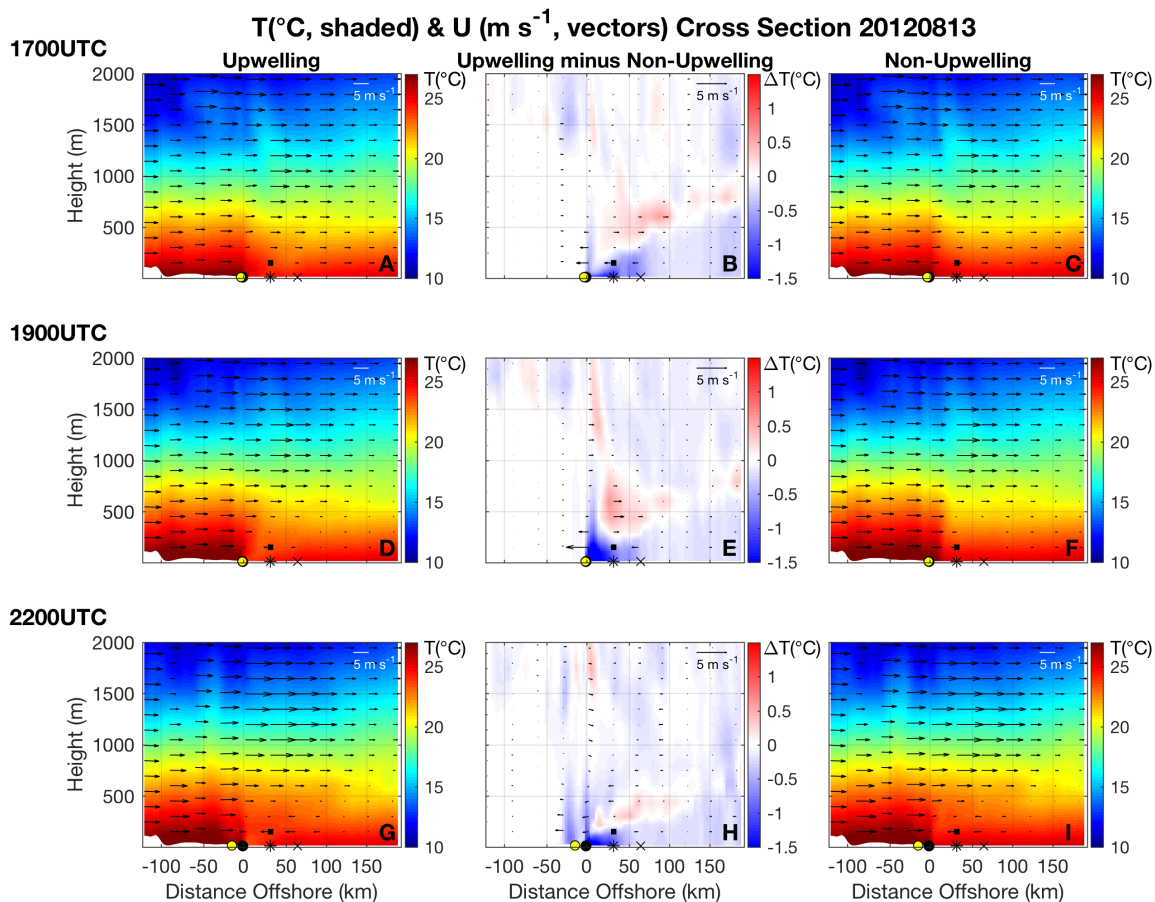
Figure 4.12 NJ vertical cross section (strong synoptic sea breeze) along location marked in Figs. 4.5 and 4.8, with upwelling (left), non-upwelling (right), and upwelling minus non-upwelling (middle), and with temperature (°C) shaded and wind vectors (m s⁻¹, both along-cross section u and w components averaged across hour beginning at time indicated at top left) in black vectors. Black dot is coast, black asterisk is at NJ WEA, black "x" is twice the distance from coast to NJ WEA offshore, black solid line is over NJ WEA at approximate blade tip height (150m), and yellow dot is weather radar sea breeze location. Note that wind vectors are exaggerated in middle difference plots.
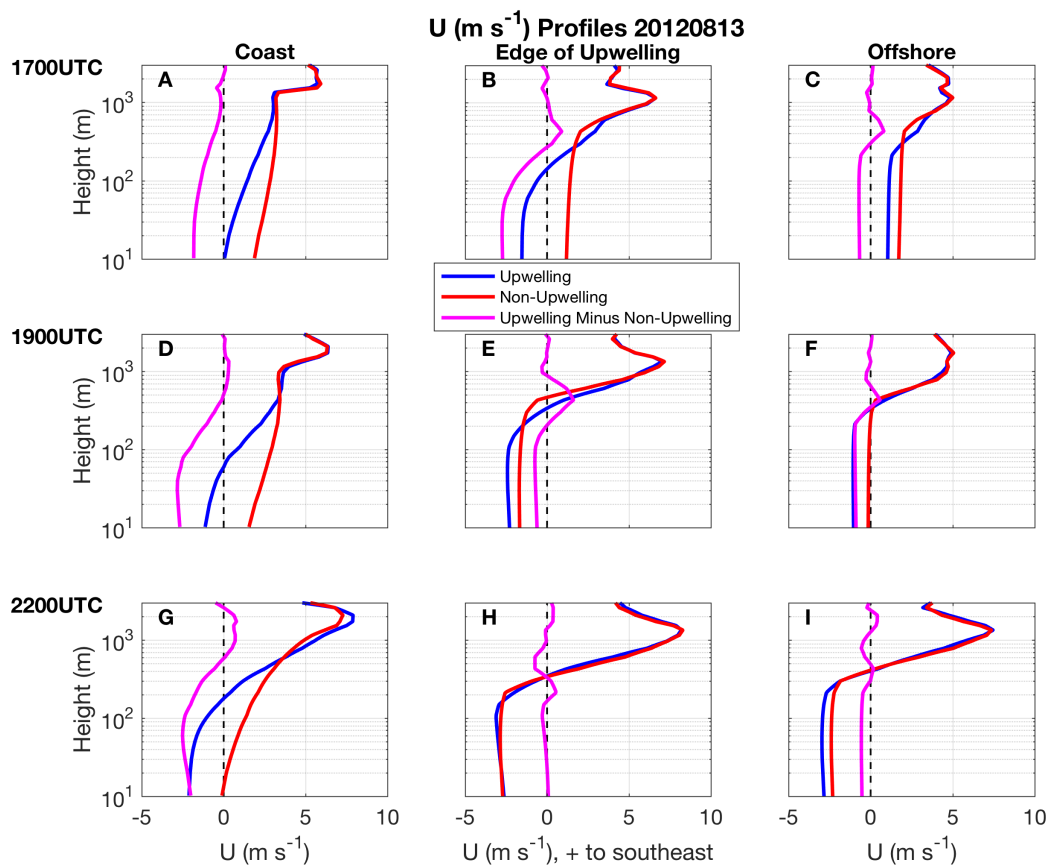
Figure 4.13 Vertical profiles of horizontal velocities (m s^{-1}, positive to the southeast) along cross section on semi-log axes at the same times as Fig. 4.12 and at the coast (left), edge of upwelling/NJ WEA (middle), and offshore (right). Upwelling (blue), non-upwelling (red), and upwelling minus non-upwelling (magenta). Vertical dashed line marks 0 horizontal velocity.

Chapter 5

Summary and Conclusions

This dissertation integrates observations (underwater gliders, HF radar, buoys, satellites, weather radar), modeling (WRF and ROMS), and innovative techniques (LCS) to improve understanding of the interaction of the summer stratified coastal ocean two-layer circulations with hurricanes and the sea breeze. Chapter 2 showed that the ahead-of-eye-center baroclinic coastal ocean cooling was the key missing contribution—not dry air intrusion, track, or wind shear—in modeling Irene's rapid decay just prior to NJ landfall. Irene's intensity was more sensitive to this cooling than any other WRF parameter tested. Chapter 3 examined the spatiotemporal variability in the baroclinic coastal ocean cooling processes observed in Irene—late summer storm with inshore track—and Barry—early summer storm with offshore track. It was found that the dominant force balance across the entire shelf ahead of eye passage for both storms was onshore wind stress balanced by offshore pressure gradient, and reversing to offshore wind stress balanced by onshore pressure gradient after the storm. This resulted in onshore surface currents opposing offshore bottom currents ahead-of-eye-center and enhancing surface to bottom current shear and surface cooling. Vertical diffusion (turbulent mixing) cooled the surface layer while advection was dominated by a tidal alternating warming/cooling signal. Finally, Chapter 4 used LCS to delineate the onshore surface convergent boundary and offshore surface divergent boundary of the sea breeze, and tested the sensitivity of the sea breeze extent to synoptic flow and coastal upwelling. It was found that synoptic flow impacted onshore extent more than offshore extent, and that upwelling did not impact sea breeze

extent but rather caused an earlier onset and a shallower, sharper, and more intense sea breeze cell both onshore and offshore.

The integration of modeling with unique observing systems will continue to pave the way for new understanding of the coastal ocean and its interaction with important weather processes. This dissertation uses this integration to fill the shallow water gap for TC intensity prediction, as well as the offshore sea breeze component clarification for offshore wind resource assessment. Future work should include better ocean data, e.g. more flexible platform coastal ocean profile time series, and assimilation into fully-coupled ocean-atmosphere-wave TC models for improved initialization; data denial studies to isolate the impact of underwater glider data assimilation in forecast models, especially in the coastal zone; and 3D LCS simulations on both the atmosphere (WRF) and ocean (2D HF radar, 3D ROMS) to better understand the air-sea interaction in the sea breeze-coastal upwelling system. Finally, the MAB's relative proximity to the Gulf Stream and its large baroclinic zones make it an important cyclogenesis region for not only winter Nor'easters but also transitioning extratropical systems like Hurricane Sandy [*Galarneau et al.*, 2013]. Future studies should investigate the competing factors of baroclinic atmospheric energy strengthening and baroclinic coastal ocean cooling weakening processes.

References

Arritt, R. W. (1989), Numerical modelling of the offshore extent of sea breezes, *Q. J. R. Meteorol. Soc.*, *115*(487), 547–570.

Atlas, D. (1960), Radar detection of the sea breeze, *J. Meteorol.*, *17*(3), 244–258.

Avila, L. A., and J. Cangialosi (2012), Tropical Cyclone Report: Hurricane Irene (AL092011), *Natl. Hurric. Cent. Trop. Cyclone Rep.*, (August 2011), 45.

Barrick, D. E., M. W. Evans, and B. L. Weber (1977), Ocean Surface Currents Mapped by Radar, *Science (80-.).*, *198*(4313), 138–144.

Bender, M. a., I. Ginis, and Y. Kurihara (1993), Numerical simulations of tropical cyclone-ocean interaction with a high-resolution coupled model, *J. Geophys. Res.*, *98*(D12), 23245, doi:10.1029/93JD02370.

Bigelow, H. B. (1933), Studies of the Waters on the Continental Shelf, Cape Cod to Chesapeake Bay: I. The Cycle of Temperature, *Pap. Phys. Oceanogr. Meteorol.*, (December).

Blumberg, A. F., and G. L. Mellor (1987), A Description of a Three-Dimensional Coastal Ocean Circulation Model, in *Three Dimensional Coastal Ocean Models*, edited by N. S. Heaps, pp. 1–16, American Geophysical Union, Washington, D.C.

Bowers, L. (2004), The Effect of Sea Surface Temperature on Sea Breeze Dynamics Along the Coast of New Jersey, Rutgers University.

Brooks, D. A. (1983), The Wake of Hurricane Allen in the Western Gulf of Mexico, *J. Phys. Oceanogr.*, *13*(1), 117–129.

Brown, B. R., and G. J. Hakim (2013), Variability and Predictability of a Three-Dimensional Hurricane in Statistical Equilibrium, *J. Atmos. Sci.*, *70*(6), 1806–1820, doi:10.1175/JAS-D-12-0112.1.

Cangialosi, J. P., and J. L. Franklin (2013a), *2012 National Hurricane Center Forecast Verification Report*.

Cangialosi, J. P., and J. L. Franklin (2013b), *2012 National Hurricane Center Forecast Verification Report*.

Cangialosi, J. P., and J. L. Franklin (2016), *National Hurricane Center Forecast Verification Report: 2015 Hurricane Season*.

Canuto, V. M., A. Howard, Y. Cheng, and M. S. Dubovikov (2001), Ocean Turbulence. Part I: One-Point Closure Model—Momentum and Heat Vertical Diffusivities, *J. Phys. Oceanogr.*, *31*(6), 1413–1426.

Canuto, V. M., A. Howard, Y. Cheng, and M. S. Dubovikov (2002), Ocean Turbulence. Part II: Vertical Diffusivities of Momentum, Heat, Salt, Mass, and Passive Scalars, *J. Phys. Oceanogr.*, *32*(1), 240–264.

Castelao, R., S. Glenn, O. Schofield, R. Chant, J. Wilkin, and J. Kohut (2008), Seasonal evolution of hydrographic fields in the central Middle Atlantic Bight from glider observations, , *35*(August 2004), 6–11, doi:10.1029/2007GL032335.

Chang, S. W., and R. A. Anthes (1979), The Mutual Response of the Tropical Cyclone and the Ocean, *J. Phys. Oceanogr.*, *9*, 128–135.

Chassignet, E. P., H. E. Hurlburt, O. M. Smedstad, G. R. Halliwell, P. J. Hogan, A. J. Wallcraft, R. Baraille, and R. Bleck (2007), The HYCOM (HYbrid Coordinate Ocean Model) data assimilative system, *J. Mar. Syst.*, *65*(1), 60–83, doi:10.1016/j.jmarsys.2005.09.016.

Clancy, R. M., J. D. Thompson, H. E. Hurlburt, and J. D. Lee (1979), A Model of Mesoscale Air-Sea Interaction in a Sea Breeze-Coastal Upwelling Regime, *Mon. Weather Rev.*, *107*(11), 1476–1505, doi:10.1175/1520-0493(1979)107<1476:AMOMAS>2.0.CO;2.

Colle, B. A., and D. R. Novak (2010), The New York Bight jet: climatology and dynamical evolution, *Mon. Weather Rev.*, *138*(6), 2385–2404, doi:10.1175/2009MWR3231.1.

Cornillon, P., C. Gilman, and L. Stramma (1987), Processing and analysis of large volumes of satellite-derived thermal infrared data, *J. Geophys. …*.

D'Asaro, E. A. (2003), The Ocean Boundary Layer below Hurricane Dennis, *J. Phys. Oceanogr.*, *33*(3), 561–579, doi:10.1175/1520-0485(2003)033<0561:TOBLBH>2.0.CO;2.

Davis, C. et al. (2008), Prediction of Landfalling Hurricanes with the Advanced Hurricane WRF Model, *Mon. Weather Rev.*, *136*(6), 1990–2005, doi:10.1175/2007MWR2085.1.

Dickey, T., D. Frye, J. McNeil, D. Manov, N. Nelson, D. Sigurdson, H. Jannasch, D. Siegel, T. Michaels, and R. Johnson (1998), Upper-Ocean Temperature Response to Hurricane Felix as Measured by the Bermuda Testbed Mooring, *Mon. Weather Rev.*, *126*(5), 1195–1201.

Dunk, R., and S. M. Glenn (2013), *An Advanced Atmospheric/Ocean Assessment Program Designed to Reduce the Risks Associated with Offshore Wind Energy Development Defined by the NJ Energy Master Plan and the NJ Offshore Wind Energy Economic Development Act: Phase I*, New Brunswick, NJ.

Dvorak, M. J., B. A. Corcoran, J. E. Ten Hoeve, N. G. Mcintyre, and M. Z. Jacobson (2013), US East Coast offshore wind energy resources and their relationship to peak-time electricity demand, *Wind Energy*, *16*(7), 977–997, doi:10.1002/we.

Emanuel, K. (2003), Tropical Cyclones, *Annu. Rev. Earth Planet. Sci.*, *31*(1), 75–104, doi:10.1146/annurev.earth.31.100901.141259.

Emanuel, K., C. DesAutels, C. Holloway, and R. Korty (2004), Environmental Control of Tropical Cyclone Intensity, *J. Atmos. Sci.*, *61*(7), 843–858, doi:10.1175/1520-0469.

Emanuel, K. a. (1999), Thermodynamic control of hurricane intensity, *Nature*, *401*(6754), 665–669, doi:10.1038/44326.

Fairall, C. W., E. F. Bradley, D. P. Rogers, J. B. Edson, and G. S. Young (1996), Bulk parameterization of air-sea fluxes for Tropical Ocean-Global Atmosphere Coupled-Ocean Atmosphere Response Experiment, *J. Geophys. Res.*, *101*(C2), 3747, doi:10.1029/95JC03205.

Fairall, C. W., E. F. Bradley, J. E. Hare, and A. A. Grachev (2003), Bulk parameterization of air-sea fluxes: Updates and verification for the COARE algorithm, *J. Clim.*, *16*(4), 571–591.

Finkele, K. (1998), Inland and Offshore Propagation Speeds of a Sea Breeze from Simulations and Measurements, *Boundary-Layer Meteorol.*, *87*, 307–329.

Fisher, E. L. (1958), Hurricanes and the Sea-Surface Temperature Field, *J. Meteorol.*, *15*(3), 328–333, doi:10.1175/1520-0469(1958)015<0328:HATSST>2.0.CO;2.

Forristall, G. Z., R. C. Hamilton, and V. J. Cardone (1977), Continental Shelf Currents in Tropical Storm Delia: Observations and Theory, *J. Phys. Oceanogr.*, *7*(4), 532–546.

Franchito, S. H., V. B. Rao, J. L. Stech, and J. a. Lorenzzetti (1998), The effect of coastal upwelling on the sea-breeze circulation at Cabo Frio, Brazil: a numerical experiment, *Ann. Geophys.*, *16*(7), 866, doi:10.1007/s005850050656.

De Freitas, C. R. (1990), Recreation Climate Assessment, *Int. J. Climatol.*, *10*(1), 89–103.

Fuglister, F. C., and L. V. Worthington (1951), Some Results of a Multiple Ship Survey of the Gulf Stream, *Tellus A*, *3*(I), doi:10.3402/tellusa.v3i1.8614.

Galarneau, T. J., C. A. Davis, and M. A. Shapiro (2013), Intensification of Hurricane Sandy (2012) through Extratropical Warm Core Seclusion, *Mon. Weather Rev.*, *141*(12), 4296–4321, doi:10.1175/MWR-D-13-00181.1.

Gentry, M. S., and G. M. Lackmann (2009), Sensitivity of Simulated Tropical Cyclone Structure and Intensity to Horizontal Resolution, *Mon. Weather Rev.*, *138*(3), 688–704, doi:10.1175/2009MWR2976.1.

Gildor, H., E. Fredj, J. Steinbuck, and S. Monismith (2009), Evidence for Submesoscale Barriers to Horizontal Mixing in the Ocean from Current Measurements and Aerial Photographs, *J. Phys. Oceanogr.*, *39*(8), 1975–1983, doi:10.1175/2009JPO4116.1.

Glenn, S. et al. (2004), Biogeochemical impact of summertime coastal upwelling on the New Jersey Shelf, *J. Geophys. Res. C Ocean.*, *109*(12), 1–15, doi:10.1029/2003JC002265.

Glenn, S., C. Jones, M. Twardowski, L. Bowers, J. Kerfoot, J. Kohut, D. Webb, and O. Schofield (2008), Glider observations of sediment resuspension in a Middle Atlantic Bight fall transition storm, *Limnol. Oceanogr.*, *53*(5 part 2), 2180–2196, doi:10.4319/lo.2008.53.5_part_2.2180.

Glenn, S. M., M. F. Crowley, D. B. Haidvogel, and Y. T. Song (1996), Underwater Observatory Captures Coastal Upwelling Events Off New Jersey, *Eos (Washington. DC).*, *77*(25), 233–240.

Glenn, S. M., T. N. Miles, G. N. Seroka, Y. Xu, R. K. Forney, F. Yu, H. Roarty, O. Schofield, and J. Kohut (2016), Stratified Coastal Ocean Interactions with Tropical Cyclones, *Nat. Commun.*, *7*(08 March 2016), doi:10.1038/ncomms10887.

Gong, D., J. T. Kohut, and S. M. Glenn (2010), Seasonal climatology of wind-driven circulation on the New Jersey Shelf, *J. Geophys. Res. Ocean.*, *115*(4), 1–25, doi:10.1029/2009JC005520.

Gould, W. J., S. Wijffels, S. Pouliquen, and B. Owens (2004), Argo Profiling Floats Bring New Era of In Situ Ocean Observations, *Eos (Washington. DC).*, *85*(19), 179–184, doi:10.1029/2004EO190002.

Green, B. W., and F. Zhang (2013), Impacts of Air–Sea Flux Parameterizations on the Intensity and Structure of Tropical Cyclones, *Mon. Wea. Rev.*, *141*(7), 2308–2324, doi:10.1175/MWR-D-12-00274.1.

Haidvogel, D. B. et al. (2008), Ocean forecasting in terrain-following coordinates: Formulation and skill assessment of the Regional Ocean Modeling System, *J. Comput. Phys.*, *227*(7), 3595–3624, doi:10.1016/j.jcp.2007.06.016.

Haller, G. (2015), Lagrangian Coherent Structures, *Annu. Rev. Fluid Mech.*, *47*, 137–162, doi:10.1146/annurev-fluid-010313-141322.

Halliwell, G. R., L. K. Shay, J. K. Brewster, and W. J. Teague (2011), Evaluation and Sensitivity Analysis of an Ocean Model Response to Hurricane Ivan, *Mon. Weather Rev.*, *139*(3), 921–945, doi:10.1175/2010MWR3104.1.

Hill, K. A., and G. M. Lackmann (2009), Analysis of Idealized Tropical Cyclone Simulations Using the Weather Research and Forecasting Model : Sensitivity to Turbulence Parameterization and Grid Spacing, *Mon. Weather Rev.*, *137*(2), 745–765, doi:10.1175/2008MWR2220.1.

Hong, S.-Y., J. Dudhia, and S.-H. Chen (2004), A Revised Approach to Ice Microphysical Processes for the Bulk Parameterization of Clouds and Precipitation, *Mon. Weather Rev.*, *132*(1), 103–120.

Houghton, R. W., R. Schlitz, R. C. Beardsley, B. Butman, and J. L. Chamberlin (1982), The Middle Atlantic Bight Cold Pool: Evolution of the Temperature Structure During Summer 1979, *J. Phys. Oceanogr.*, *12*(10), 1019–1029, doi:10.1175/1520-0485.

Hunter, E., R. Chant, L. Bowers, S. Glenn, and J. Kohut (2007), Spatial and temporal variability of diurnal wind forcing in the coastal ocean, *Geophys. Res. Lett.*, *34*(3), 1–5, doi:10.1029/2006GL028945.

Jacob, S. D., and L. K. Shay (2003), The Role of Oceanic Mesoscale Features on the Tropical Cyclone–Induced Mixed Layer Response: A Case Study, *J. Phys. Oceanogr.*, *33*(4), 649–676, doi:10.1175/1520-0485(2003)33<649:TROOMF>2.0.CO;2.

Jaimes, B., and L. K. Shay (2009), Mixed Layer Cooling in Mesoscale Oceanic Eddies during Hurricanes Katrina and Rita, *Mon. Weather Rev.*, *137*(12), 4188–4207, doi:10.1175/2009MWR2849.1.

Jaimes, B., and L. K. Shay (2010), Near-Inertial Wave Wake of Hurricanes Katrina and Rita over Mesoscale Oceanic Eddies, *J. Phys. Oceanogr.*, *40*(6), 1320–1337, doi:10.1175/2010JPO4309.1.

Jaimes, B., and L. K. Shay (2015), Enhanced Wind-Driven Downwelling Flow in Warm Oceanic Eddy Features during the Intensification of Tropical Cyclone Isaac (2012): Observations and Theory, *J. Phys. Oceanogr.*, *45*(6), 1667–1689, doi:10.1175/JPO-D-14-0176.1.

Jaimes, B., L. K. Shay, and G. R. Halliwell (2011), The Response of Quasigeostrophic Oceanic Vortices to Tropical Cyclone Forcing, *J. Phys. Oceanogr.*, *41*(10), 1965–1985, doi:10.1175/JPO-D-11-06.1.

Kain, J. S. (2004), The Kain–Fritsch Convective Parameterization: An Update, *J. Appl. Meteorol.*, *43*(1), 170–181, doi:http://dx.doi.org/10.1175/1520-0450(2004)043<0170:TKCPAU>2.0.CO;2.

Keen, T. R., and S. M. Glenn (1995), A coupled hydrodynamic-bottom boundary layer model of storm and tidal flow in the Middle Atlantic Bight of North America, *J. Phys. Oceanogr.*, *25*(3), 391–406.

Khain, A., B. Lynn, and J. Shpund (2016), High resolution WRF simulations of Hurricane Irene : Sensitivity to aerosols and choice of microphysical schemes, *Atmos. Res.*, *167*, 129–145, doi:10.1016/j.atmosres.2015.07.014.

Khain, A. P., and I. Ginis (1991), The mutual response of a moving tropical cyclone and the ocean, *Contrib. to Atmos. Phys.*, *64*(2), 125–141.

Khain, A. P., B. Lynn, and J. Dudhia (2010), Aerosol Effects on Intensity of Landfalling Hurricanes as Seen from Simulations with the WRF Model with Spectral Bin Microphysics, *J. Atmos. Sci.*, *67*, 365–384, doi:10.1175/2009JAS3210.1.

Kim, H. S., C. Lozano, V. Tallapragada, D. Iredell, D. Sheinin, H. L. Tolman, V. M. Gerald, and J. Sims (2014), Performance of ocean simulations in the coupled HWRF-HYCOM model, *J. Atmos. Ocean. Technol.*, *31*(2), 545–559, doi:10.1175/JTECH-D-13-00013.1.

Lalas, D. P., D. N. Asimakopoulos, and D. G. Deligiorgi (1983), Sea-Breeze Circulation and Photochemical Pollution In Athens, Greece, , *17*(9), 1621–1632.

Landsea, C. W., and J. L. Franklin (2013), Atlantic Hurricane Database Uncertainty and Presentation of a New Database Format, *Mon. Weather Rev.*, *141*(10), 3576–3592, doi:10.1175/MWR-D-12-00254.1.

Lee, C.-Y., and S. S. Chen (2014), Stable Boundary Layer and Its Impact on Tropical Cyclone Structure in a Coupled Atmosphere–Ocean Model, *Mon. Weather Rev.*, *142*(5), 1927–1945, doi:10.1175/MWR-D-13-00122.1.

Leipper, D. F. (1967), Observed Ocean Conditions and Hurricane Hilda, 1964, *J. Atmos. Sci.*, *24*(2), 182–186, doi:10.1175/1520-0469(1967)024<0182:OOCAHH>2.0.CO;2.

Lentz, S. J. (2008), Observations and a Model of the Mean Circulation over the Middle Atlantic Bight, *J. Phys. Oceanogr.*, *38*(6), 1203–1221, doi:10.1175/2007JPO3768.1.

Lim, K.-S. S., and S.-Y. Hong (2010), Development of an Effective Double-Moment Cloud Microphysics Scheme with Prognostic Cloud Condensation Nuclei (CCN) for Weather and Climate Models, *Mon. Weather Rev.*, *138*(5), 1587–1612, doi:10.1175/2009MWR2968.1.

Lin, I.-I., C.-H. Chen, I.-F. Pun, W. T. Liu, and C.-C. Wu (2009), Warm ocean anomaly, air sea fluxes, and the rapid intensification of tropical cyclone Nargis (2008), *Geophys. Res. Lett.*, *36*(3), 1–5, doi:10.1029/2008GL035815.

Liu, B., H. Liu, L. Xie, C. Guan, and D. Zhao (2011), A Coupled Atmosphere – Wave –

Ocean Modeling System Simulation of the Intensity of an Idealized Tropical Cyclone, *Mon. Weather Rev.*, *139*(1), 132–152, doi:10.1175/2010MWR3396.1.

Lynn, B. H., A. P. Khain, J. W. Bao, S. a. Michelson, T. Yuan, G. Kelman, D. Rosenfeld, J. Shpund, and N. Benmoshe (2015), The sensitivity of Hurricane Irene to aerosols and ocean coupling: simulations with WRF spectral bin microphysics, *J. Atmos. Sci.*, 150413133444005, doi:10.1175/JAS-D-14-0150.1.

Marks, F. D. et al. (1998), Landfalling Tropical Cyclones:Forecast Problems and Associated Research Opportunitis, *Bull.*, *79*(2), 305–321.

Mayer, D. A., and H. O. Mofjeld (1981), Near-Inertial Internal Waves Observed on the Outer Shelf in the Middle Atlantic Bight in the Wake of Hurricane Belle, *J. Phys. Oceanogr.*, *11*(1), 87–106.

Mehra, A., and I. Rivin (2010), A Real Time Ocean Forecast System for the North Atlantic Ocean, *Terr. Atmos. Ocean. Sci.*, *21*(1), 211–228, doi:10.3319/TAO.2009.04.16.01(IWNOP)A.

Mei, W., C. Pasquero, and F. Primeau (2012), The effect of translation speed upon the intensity of tropical cyclones over the tropical ocean, *Geophys. Res. Lett.*, *39*(7), 1–6, doi:10.1029/2011GL050765.

Mesinger, F. et al. (2006), North American Regional Reanalysis, *Bull. Am. Meteorol. Soc.*, *87*(3), 343–360, doi:10.1175/BAMS-87-3-343.

Miles, T., S. Glenn, and O. Schofield (2013), Temporal and spatial variability in fall storm induced sediment resuspension on the Mid-Atlantic Bight, *Cont. Shelf Res.*, *63*.

Miles, T. N., G. N. Seroka, J. T. Kohut, O. Schofield, and S. M. Glenn (2015), Glider observations and modeling of sediment transport in Hurricane Sandy, *J. Geophys. Res. Ocean.*, *120*, 1771–1791, doi:10.1002/2014JC010474.Received.

Miller, S. T. K., B. D. Keim, R. W. Talbot, and H. Mao (2003), SEA BREEZE: STRUCTURE, FORECASTING, AND IMPACTS, , (January), doi:10.1029/2003RG000124.

Munoz-Esparza, D., and B. Canadillas (2012), Forecasting the Diabatic Offshore Wind Profile at FINO1 with the WRF Mesoscale Model, *DEWI Mag.*, (40), 73–79.

Nakanishi, M., and H. Niino (2004), An Improved Mellor-Yamada Level-3 Model With Condensation Physics: Its Design And Verification, *Boundary-Layer Meteorol.*, *112*(1), 1–31.

Nakanishi, M., and H. Niino (2006), An improved Mellor–Yamada level-3 model: Its numerical stability and application to a regional prediction of advection fog, *Boundary-Layer Meteorol.*, *119*(2), 397–407, doi:10.1007/s10546-005-9030-8.

NOAA National Centers for Environmental Prediction (2016), U.S. Coastal Relief Model, Available from: http://www.ngdc.noaa.gov/mgg/coastal/crm.html

Papanastasiou, D. K., D. Melas, T. Bartzanas, and C. Kittas (2010), Temperature, comfort and pollution levels during heat waves and the role of sea breeze, *Int. J. Biometeorol.*, *54*(3), 307–317, doi:10.1007/s00484-009-0281-9.

Pielke, R. A. (1991), Regional and mesoscale meteorological modeling as applied to air quality studies, in *Air Pollution Modeling and Its Application VIII*, pp. 259–289.

Pollard, R. T., P. B. Rhines, and R. O. Thompson (1972), The deepening of the wind-mixed layer, *Geophys. Astrophys. Fluid Dyn.*, *4*(1), 381–404.

Price, J. F. (1981), Upper Ocean Response to a Hurricane, *J. Phys. Oceanogr.*, *11*(2), 153–175, doi:10.1175/1520-0485(1981)011<0153:UORTAH>2.0.CO;2.

Price, J. F., R. A. Weller, and R. Pinkel (1986), Diurnal Cycling: Observations and Models of the Upper Ocean Response to Diurnal Heating, Cooling, and Wind Mixing, *J. Geophys. Res. Ocean.*, *91*(C7), 8411–8427, doi:10.1029/JC091iC07p08411.

Price, J. F., T. B. Sanford, and G. Z. Forristall (1994), Forced Stage Response to a Moving Hurricane, *J. Phys. Oceanogr.*, *24*, 233–260, doi:http://dx.doi.org/10.1175/1520-0485(1994)024<0233:FSRTAM>2.0.CO;2.

Rappaport, E. N., J. L. Frankling, M. DeMaria, L. K. Shay, and E. J. Gibney (2010), Tropical Cyclone Intensity Change before U.S. Gulf Coast Landfall, *Weather Forecast.*, *25*(5), 1380–1396, doi:10.1175/2010WAF2222369.1.

Ratcliff, M. A., R. L. Petersen, R. Dunk, and J. DeToro (1996), Comparison of wind tunnel and ISDM model simulations of sea breeze fumigation, in *AIR & WASTE MANAGEMENT ASSOCIATION*, Atlanta, GA.

Reynolds, R. W., and D. B. Chelton (2010), Comparisons of daily Sea surface temperature analyses for 2007-08, *J. Clim.*, *23*(13), 3545–3562, doi:10.1175/2010JCLI3294.1.

Rhome, J. R., C. A. Sisko, and R. D. Knabb (2006), On the Calculation of Vertical Shear: An Operational Perspective, *Prepr. 27th Conf. Hurricanes Trop. Meteorol.*, *14*.

Roemmich, D., G. C. Johnson, S. Riser, R. Davis, J. Gilson, B. Owens, S. L. Garzoli, C. Schmid, and M. Ignasqewski (2009), The Argo Program: Observing the Global Ocean with Profiling Floats, , *22*(2), 34–43.

Rogers, R., S. Aberson, M. Black, P. Black, and J. Cione (2006), The intensity forecasting experiment: A NOAA multiyear field program for improving tropical cyclone intensity forecasts, , (June), 1523–1537, doi:10.1175/BAMS-87-11-1523.

Rothermel, R. C. (1983), *How to Predict the Spread and Intensity of Forest and Range Fires*.

Rotunno, R. (1983), On the Linear Theory of the Land and Sea Breeze, *J. Atmos. Sci.*, *40*(8), 1999–2009.

Ruiz, S., L. Renault, B. Garau, and J. Tintoré (2012), Underwater glider observations and modeling of an abrupt mixing event in the upper ocean, *Geophys. Res. Lett.*, *39*(1), n/a–n/a, doi:10.1029/2011GL050078.

Sampson, C. R., and A. J. Schrader (2000), The Automated Tropical Cyclone Forecasting System (version 3.2), *Bull. Am. Meteorol. Soc.*, *81*(6), 1231–1240, doi:10.1175/1520-0477(2000)081<1231:TATCFS>2.3.CO;2.

Sanabia, E. R., and S. R. Jayne (2014), Evolution of the Upper-Ocean Thermal Structure

beneath Hurricanes Iselle and Julio (2014), in *American Geophysical Union Fall Meeting*.

Sanabia, E. R., B. S. Barrett, P. G. Black, S. Chen, and J. A. Cummings (2013), Real-Time Upper-Ocean Temperature Observations from Aircraft during Operational Hurricane Reconnaissance Missions: AXBT Demonstration Project Year One Results, *Weather Forecast.*, *28*(6), 1404–1422, doi:10.1175/WAF-D-12-00107.1.

Sanabia, E. R., S. R. Jayne, W. Swick, S. Chen, and J. Cummings (2016), Variability in Upper-Ocean Thermal Structure beneath Tropical Cyclones as Observed by Air-Deployed Profiling Floats, in *32nd Conference on Hurricanes and Tropical Meteorology*.

Sanford, T. B., P. G. Black, J. R. Haustein, J. W. Feeney, G. Z. Forristall, and J. F. Price (1987), Ocean Response to a Hurricane. Part I: Observations, *J. Phys. Oceanogr.*, *17*(11), 2065–2083.

Schade, L. R., and K. a. Emanuel (1999), The Ocean's Effect on the Intensity of Tropical Cyclones: Results from a Simple Coupled Atmosphere–Ocean Model, *J. Atmos. Sci.*, *56*(4), 642–651, doi:10.1175/1520-0469(1999)056<0642:TOSEOT>2.0.CO;2.

Schofield, O. et al. (2007), Slocum Gliders: Robust and ready, *J. F. Robot.*, *24*(6), 473–485, doi:10.1002/rob.20200.

Schofield, O., R. J. Chant, B. Cahill, and R. Castelao (2008), The Decadal View of the Mid-Atlantic Bight from the COOLroom: Is Our Coastal System Changing?, *Oceanography*, *21*(4), 108–117.

Seroka, G. N., T. N. Miles, Y. Xu, J. T. Kohut, O. Schofield, and S. M. Glenn (2016), Hurricane Irene Sensitivity to Stratified Coastal Ocean Cooling, *Mon. Weather Rev.*, *144*(9), 3507–3530, doi:10.1175/MWR-D-15-0452.1.

Sessions, M. H., T. P. Barnett, and W. S. Wilson (1976), The airborne expendable bathythermograph, *Deep Sea Res. Oceanogr. Abstr.*, *23*(8), 779–782.

Shay, L. K., P. G. Black, A. J. Mariano, J. D. Hawkins, and R. L. Elsberry (1992), Upper Ocean Response to Hurricane Gilbert, *J. Geophys. Res. Ocean.*, *97*(20), 227–248.

Simpson, J. E. (1994), *Sea Breeze and Local Winds*, Cambridge University Press, Cambridge, UK.

Simpson, J. E., D. A. Mansfield, and J. R. Milford (1977), Inland penetration of sea-breeze fronts, *Q. J. R. Meteorol. Soc.*, *103*(435), 47–76.

Skamarock, W. C., J. B. Klemp, J. Dudhia, D. O. Gill, D. M. Barker, M. G. Duda, X.-Y. Huang, W. Wang, and J. G. Powers (2008), A Description of the Advanced Research WRF Version 3, *NCAR Tech. NOTE*, (June).

Steele, C. J., S. R. Dorling, R. Von Glasow, and J. Bacon (2013), Idealized WRF model sensitivity simulations of sea breeze types and their effects on offshore windfields, *Atmos. Chem. Phys.*, *13*(1), 443–461, doi:10.5194/acp-13-443-2013.

Steele, C. J., S. R. Dorling, R. von Glasow, and J. Bacon (2014), Modelling sea-breeze climatologies and interactions on coasts in the southern North Sea: implications for offshore wind energy, *Q. J. R. Meteorol. Soc.*, n/a–n/a, doi:10.1002/qj.2484.

Suda, K. (1943), *Ocean Science*, Kokin-Shoin, Tokyo.

Sutyrin, G. G., and E. A. Agrenich (1979), Interaction of the boundary layers of the ocean and atmosphere in a tropical cyclone, *Meteor. Gidrol.*, *2*, 45–56.

Sutyrin, G. G., and A. P. Khain (1984), The Influence of the Ocean-Atmosphere Interaction on the Intensity of Moving Tropical Cyclones, *Izv. Akad. Nauk SSSR Fiz. Atmos. I Okeana*, 787–794.

Tallapragada, V., S. Gopalakrishnan, Q. Liu, and T. Marchok (2011), Hurricane Weather Research and Forecasting (HWRF) model: 2011 scientific documentation, *Dev. Testbed Cent.*, (February), 1–96.

Tallapragada, V., C. Kieu, Y. Kwon, S. Trahan, Q. Liu, Z. Zhang, and I.-H. Kwon (2014), Evaluation of Storm Structure from the Operational HWRF during 2012 Implementation, *Mon. Weather Rev.*, *142*(11), 4308–4325, doi:10.1175/MWR-D-13-00010.1.

Torn, R. D., and C. Snyder (2012), Uncertainty of Tropical Cyclone Best-Track Information, *Weather Forecast.*, *27*(3), 715–729, doi:10.1175/WAF-D-11-00085.1.

Umlauf, L., and H. Burchard (2003), A generic length-scale equation for geophysical turbulence models, *J. Mar. Res.*, *61*(2), 235–265, doi:10.1357/002224003322005087.

Venkatesan, R., R. Mathiyarasu, and K. M. Somayaji (2002), A study of atmospheric dispersion of radionuclides at a coastal site using a modified Gaussian model and a mesoscale sea breeze model, , *36*, 2933–2942.

Walker, N. D., R. R. Leben, and S. Balasubramanian (2005), Hurricane-forced upwelling and chlorophyll a enhancement within cold-core cyclones in the Gulf of Mexico, *Geophys. Res. Lett.*, *32*(18), 1–5, doi:10.1029/2005GL023716.

Warner, J. C., C. R. Sherwood, H. G. Arango, and R. P. Signell (2005), Performance of four turbulence closure models implemented using a generic length scale method, *Ocean Model.*, *8*(1-2), 81–113, doi:10.1016/j.ocemod.2003.12.003.

Wilkin, J. L., and E. J. Hunter (2013), An assessment of the skill of real-time models of Mid-Atlantic Bight continental shelf circulation, *J. Geophys. Res. Ocean.*, *118*(6), 2919–2933, doi:10.1002/jgrc.20223.

Zambon, J. B., R. He, and J. C. Warner (2014a), Investigation of hurricane Ivan using the coupled ocean–atmosphere–wave–sediment transport (COAWST) model, *Ocean Dyn.*, *64*(11), 1535–1554, doi:10.1007/s10236-014-0777-7.

Zambon, J. B., R. He, and J. C. Warner (2014b), Tropical to extratropical: Marine environmental changes associated with Superstorm Sandy prior to its landfall, *Geophys. Res. Lett.*, *41*, 8935–8943, doi:10.1002/2014GL061357.Received.

Zhang, W. G., and G. G. Gawarkiewicz (2015), Dynamics of the direct intrusion of Gulf Stream ring water onto the Mid-Atlantic Bight shelf, *Geophys. Res. Lett.*, *42*(18), 7687–7695, doi:10.1002/2015GL065530.Received.